IMPLEMENTATION AND OPTIMISATION OF MICROWAVE MEDICAL IMAGING BASED ON THE MULTIPLE-FREQUENCY DBIM-TWIST ALGORITHM

Miao, Zhenzhuang

Awarding institution:
King's College London

IMPLEMENTATION AND OPTIMISATION OF MICROWAVE MEDICAL IMAGING BASED ON THE MULTIPLE-FREQUENCY DBIM-TWIST ALGORITHM

Zhenzhuang Miao

Supervisor: **Dr. Panagiotis Kosmas**

Department of Informatics

King's College London

This dissertation is submitted for the degree of

Doctor of Philosophy

September 2017

To my family, best friends, and Panos

Declaration

I hereby declare that except where specific reference is made to the work of others, the contents of this dissertation are original and have not been submitted in whole or in part for consideration for any other degree or qualification in this, or any other university. This dissertation is my own work and contains nothing which is the outcome of work done in collaboration with others, except as specified in the text and Acknowledgements. This dissertation contains fewer than 65,000 words including appendices, bibliography, footnotes, tables and equations and has fewer than 150 figures.

Zhenzhuang Miao

September 2017

Acknowledgements

This thesis would not have been possible without the guidance and the support of several individuals.

First of all, I owe my deepest gratitude to Dr. Panagiotis Kosmas for his continuous support, relentless and insightful guidance. Without your help, I will never be what I am. Thank you, sir. Your motivation and knowledge are irreplaceable assets for me.

I would like to thank Prof. Paul Meaney for allowing me to study with him at Dartmouth College. The great experience added an extra dimension to my research and helped me obtain the initial experience of the realistic experiment system. I would also like to thank Dr. Shuyu Ping, Dr. Fei Gao and Syed Ahsan for their accompanying and endless supports during my PhD life.

I am particularly grateful to all my current and erstwhile colleagues at CTR, including Yuhang, Xinruo, Gao, Menglan, Hong, Jinwei, Xi, Xun, Changtao, and Ziwen. Thank you guys for all the support and cooperation you have extended to me and for making my stay at CTR as the most memorable time of my life.

Last, but not the least, I wish to thank my parents and my wife, who have always stood by me through thick and thin. It is to them that I owe all the success in life.

Abstract

The goal of microwave breast imaging is to recover the profile of the dielectric properties of the breast by solving an inverse problem. In this thesis, a novel DBIM algorithm based on the TwIST method is proposed to reconstruct the complex permittivity of 2-D anatomically realistic numerical breast phantoms. A combined optimisation of the algorithm parameters is applied to improve the quality of reconstructions and the robustness of the algorithm.

Furthermore, we present new strategies which improve further the performance of the DBIM-TwIST algorithm by refining our previous work on multiple-frequency reconstructions using a single-pole Debye model. Multiple-frequency approaches can combine the stabilizing effects of lower frequencies with enhanced resolution of higher frequencies, thereby overcoming stability and resolution limitations of single-frequency algorithms which tend to be very dependent upon the chosen frequency. And then a novel hybrid frequency approach is proposed to optimise stability and reconstruction accuracy at lower computational cost relative to frequency-hopping techniques.

Besides, we propose an innovative two-step reconstruction approach for optimising the initial guess prior to reconstruction. Our approach adds low computational cost to the final breast reconstructions, and improves significantly the reconstruction quality for different breast phantoms. It can then be proposed that an L^1 norm regularisation of the TwIST method is based on the Pareto curve, which contributes to de-noising and stabilising the algorithm convergence.

At last, we focus on the application of the optimized DBIM-TwIST algorithm to data obtained from an MWI prototype, including direct measured data from MWI experiments, and numerical data from a CAD model emulating the MWI experiments using CST EM software. Based on our new eight-antenna microwave system with a small triangular patch printed monopole, our research demonstrates that the algorithm is able to image cylindrical targets immersed in a background (known) medium despite the model errors due to approximating the real experiment with our 2-D FDTD model. Moreover, a frequency selection method based on correlation analysis is proposed to improve the usage of the frequency information. Finally, we perform image reconstructions using a two-layer medium in order to enhance signal transmission through the imaging domain and at the same time reduce unwanted multi-path signals that do no interact with the interrogated imaging domain.

Table of contents

List of figures

List of tables

Chapter 1

INTRODUCTION

1.1 Fundamentals of Microwave Imaging

We start by a review on microwave imaging (MWI) since its inception up to the most recent developments. This will introduce the reader to microwave capabilities in biomedical applications, and what has been done to date in this area. The motivation of this research into MWI is based on two key facts: firstly, that microwave waves are less harmful than X-rays and secondly, they could be produced at a lower cost than any other imaging system.

Microwave medical imaging relies on the difference in the dielectric properties of the different human tissues. For instance, the dielectric properties (permittivity and conductivity) of the malignant tissues in breast cancer are higher than those of normal breast tissue. This difference is referred to as dielectric contrast, which can be detected by MWI methods. MWI employs energy levels that do not harm the tissues and the equipment used has lower associated costs than the currently widely used diagnostic tools, e.g. magnetic resonance imaging (MRI) or X-rays. Therefore, MWI has potential benefits in early-stage breast cancer detection for the screening of the population at risk.

MWI systems seek to address the limitations of today's standard imaging modalities for breast cancer detection. For instance, X-ray mammography may pose several health

risks due to its delivery of ionising radiation into the breast tissues. Another drawback of mammography is the pain associated with breast compression. It also has relatively low sensitivity especially in the case of radiologically dense breast tissue [1]. In the case of ultrasound, the images contain too many artefacts and ambiguities (such as shadowing, speckle, and non-quantified contrasts). These issues often result in insufficient effective resolutions, a lack of specificity in distinguishing malignant and normal masses, and a lack of distinguishing between normal background tissue and suspected masses [1]. The main disadvantage of MRI is its operating cost. The long examination times and the use of a contrast agent (gadolinium) make it unsuitable for screening purposes. Also, access to this imaging tool is rather limited and may result in unacceptable delays in the time for testing [2].

To investigate the ability of MWI for breast cancer detection, several studies of the dielectric properties of biological tissues at microwave frequencies were carried out. The results show that the dielectric contrast between malignant and normal breast tissues is sufficient for early stage breast cancer detection [2–5].

Various acquisition set-ups have been considered for the microwave measurements of the breast [5–14]. These set-ups can be categorised into three groups: passive, active, and hybrid. In the passive systems, which are similar to radiometry, a sensor measures the radiated thermal electromagnetic energy. The energy detected by a radiometer at microwave frequencies is the thermal emission from the tissue itself and from the environment that arrives at the radiometer after reflection. This intensity of emission is proportional to the temperature of the tissue. Cancer detection relies on the fact there is a temperature contrast between a malignant tumour and the surrounding normal tissue due to the difference in their metabolism [15].

In some systems, the contrast between malignant and normal tissue increases further. To archive a better contrast, for example, microwave radiation can be used to induce heat. Such systems are examples of hybrid systems. For instance in the microwave-induced acoustic imaging, microwaves are used to illuminate the breast. Due to the

higher conductivity of malignant breast tissue, more energy is deposited in tumours, resulting in selective heating of these lesions. A tumour expands and generates pressure waves, which are detected by ultrasound transducers [16].

The active methods are based on the generation of microwave signals that are coupled to the tissue using antennas. The microwave signals penetrate into the tissue and are scattered. This scattered field can also be extracted into three different scenarios: mono-static, bi-static or multi-static. In the mono-static scenario, which is common in radar, the transmitting (Tx) and the receiving (Rx) antennas are co-located, and the waves are extracted at the point at which they were generated. Moreover, to construct tissue images, scanning the Tx/Rx location over a sufficiently large surface (acquisition surface) is essential [17].

In a bi-static scenario, the Tx and Rx locations are different, and one antenna transmits and only one antenna receives. To obtain tissue images similar to the mono-static scenario, either the Tx or the Rx antenna, or both, may be scanned over their respective surfaces [18]. A multi-static system is a generalisation of the bi-static system, with one or more receivers extracting microwave signals from one or more geographically separated transmitters. Scanning the Tx/Rx antennas may also be used in multi-static systems [19].

Most systems exploit active MWI techniques. The focus of this study will also be on active systems. The goals of MWI design are increasing its capability to detect low-contrast and small-sized tumours as well as reducing its size and cost. The improvements can be realised both in the hardware and the software system components. Here, the focus is on the hardware of the MWI system and the evaluation of its performance. As a matter of fact, the hardware of the MWI system has a primary role in determining the performance, size and cost of the system.

There are several challenges in MWI that hardware design needs to address [20, 21]. One such challenge is coupling microwave power into the tissue. Due to the large difference between the electrical properties of living tissue and air, the reflection of any

microwave radiation generated in the air at the tissue interface is significant. In general, different layers of tissue not only reflect back the microwave power but also limit its penetration through attenuation.

To reduce reflections and increase the coupling power into the tissue coupling liquids are used [22]. Although using coupling liquids reduces the reflections, it can still cause power loss due to spillovers and dissipation in the coupling liquid. Moreover, coupling liquids make the maintenance of the acquisition system more difficult in clinical implementations. Another approach to improve the power coupling into the tissue is to design the antennas so that they couple the power through direct contact with the tissue [21]. In this case, the acquisition system should be flexible for adjustments or deformations of set-up to conform to the size and shape of the particular imaged tissue.

The low dynamic range of MWI systems is another challenging factor. The loss in medium, sensor efficiency and uncertainty in tissue measurements are major defining factors of the dynamic range in MWI systems. A high dynamic range is desirable to achieve better microwave signal penetration depth and better sensitivity of tumour detection.

1.2 Literature Review

Two approaches have been applied to MWI: microwave tomography and radar-based approaches; both use the scattering of microwave signals. The systems transmit the microwave signals into the breast and then measure scattered signals reflected from the tumour.

1.2.1 Microwave Tomography

Microwave tomography techniques have been studied by several research groups [5, 22–47]. Prof. Paulsen and Prof. Meaney from Dartmouth College in the United States are one of the representative research groups. They have studied microwave tomography

breast imaging since 1990s [48–51]. And they proposed an iterative reconstruction algorithm by obtaining dielectric properties in a 2D lossy medium in 1995.

The goal of microwave tomography is to recover the profile using the inverse problem of the dielectric properties of the breast. Microwave tomography uses an inverse scattering method to develop a diagnostic image of the breast. Inverse scattering uses scattering signals, including diffraction from objects. It creates a map of permittivity and conductivity through inversion of those signals [52]. However, the inverse problem takes an increased amount of time, because the calculation process is complicated. Furthermore, a non-linear inverse scattering problem must be solved, and iterative image reconstruction algorithms are usually required to obtain a solution. In general, these ill-posed inverse scattering approaches suffer from non-uniqueness and require regularisation in order to achieve convergence to a meaningful solution [29, 53].

The Dartmouth group, for the first time, have developed a clinical prototype for active MWI of the breast [5]. They developed a 32-channel data acquisition system operating at a frequency range of 500 MHz to 3 GHz [49] to obtain data from a clinical prototype exam. The clinical prototype illuminates the breast with 16 monopole antennas that operate in the 300 MHz to 1 GHz frequency range. The clinical exam was conducted with five women, and the total acquisition time was 10–15 minutes per breast. The system measured and obtained data at seven different array heights for seven different frequencies at each array position [52].

King's College London is one institute that has been experimenting on different antenna designs for microwave tomography [44, 46]. They have also proposed new imaging algorithms, such as an adaptive thresholding iterative shrinkage algorithm to the linear inversion at each iteration of the distorted Born iterative method (DBIM) [54]. Other groups are researching on reducing high computational demands due to a number of iterations and discretisation of the object image for accuracy. Xu et al. at the University of Manitoba proposed an iterative process that involves two algorithms: finite-difference time-domain (FDTD) and genetic algorithm (GA). They developed a parallel algorithm

for microwave tomography on CPU-based homogeneous multi-core distributed memory machines and the Cell BE processor [30, 31, 38]. The research group at the National University of Ireland, Galway in Ireland presented a novel parallelisation strategy to accelerate microwave tomography [47]. The IREA, National Research Council of Italy, also developed diagnostic and therapeutic strategies based on the use of electromagnetic fields at microwave frequencies for several years. They researched magnetic nanoparticles (MNP) enhanced MWI which is able to reduce the rate of false positives and negatives [55–58]. In addition, the research has been progressed in therapeutic aspects with microwave ablation at IREA and the University of Wisconsin—Madison [59–61].

1.2.2 Radar-Based Microwave Imaging

Microwave radar imaging reconstructs the image using the reflected wave from objects. It uses the reflection that arises due to the difference in the electrical dielectric properties of normal and malignant breast tissues, when microwaves transmit the internal breast with a tumour. This approach, which was first developed as a military ground-penetrating application, is applied to the human body. It was designed in the late 1990s by Hagness at Wisconsin University, and Benjamin at Bristol University [62–67]. Researchers at the National University of Ireland, Galway, Tianjin University in China and Hiroshima University are also working on this subject [10, 14, 68–79]. Recently, Goethe University of Frankfurt and the University of Bristol have developed experimental phantom-based imaging on 3D printing technology that was one step closer to the development of standard breast phantoms [80].

Microwave imaging via space–time (MIST) beamforming uses finite impulse response (FIR) filters to compensate for the frequency-dependent time delay, such as dispersion and fractional time delay. The microwave image is formed by summing the filtered signals. Microwave breast cancer imaging uses a generalised likelihood ratio test (GLRT), which is a hypothesis testing problem for each voxel, with the null hypothesis representing the tumour-free case. Reference [68] shows the image formation equations. However,

most of those methods have suffered from performance degradation used with dense breast. Thus, at the National University of Ireland, Galway, they used a preprocessing filter to compensate the path-dependent attenuation and phase effects. In addition, they investigated the focal quality metrics to estimate average dielectric properties to enhance tumour detection [81]. The University of Bristol also presented a time-domain wideband adaptive beamforming to reduce clutter [82]. The approach uses an adapted equalisation filter that adapts a calculated estimation of averaging dielectric properties of the breast.

1.3 Contribution and Relevant Publications

The Main contribution of this research is in the area of algorithm development and optimization for microwave tomography.

- The TwIST algorithm has been applied and optimized for MWI for the first time (Ch.3).
- The thesis proposes a new way of combining multiple frequency information to improve robustness, and tools for optimising the computational efficiency of the forward FDTD solver based on a resolution adjustment (Ch. 4)
- The thesis proposes a novel two-step DBIM algorithm, where the first step estimates the average breast properties in a fast and efficient way. This two-step algorithm can avoid false solutions (Ch. 5).
- A novel regularization technique based on the Pareto curve is proposed for the first time in MWI (Ch. 5).
- The proposed MWI algorithm is assessed for realistic experiments with a unique approach, using a three-dimensional (3-D) CAD model first to assess model error without additional random experimental errors such as interference, before moving to data from the true experimental system. (Ch. 6)

- The impact of frequency selection in reconstructions from experimental data is systematically studied for the first time using correlation metrics that are applied to the experimental data directly. (Ch.6)

The publications related to the main contributions of this thesis are stated as follows.

(1) P. Kosmas and Z. Miao, "Recent advances in microwave medical imaging based on the DBIM," *2014 IEEE MTT-S International Microwave Workshop Series on RF and Wireless Technologies for Biomedical and Healthcare Applications (IMWS-Bio2014)*, London, 2014, 3 pages. (Ch.3)

(2) Z. Miao and P. Kosmas, "Microwave breast imaging based on an optimized two-step iterative shrinkage/thresholding method," in *2015 9th European Conference on Antennas and Propagation (EuCAP)*, 2015, 4 pages. (Ch.3)

(3) Z. Miao and P. Kosmas, "Multiple-frequency DBIM-TwIST algorithm for microwave breast imaging", *IEEE Trans. Antennas Propag.*, vol. 65, no. 5, pp. 2507-2516, May 2017. (Ch. 4 and 5)

(4) Z. Miao, S. Ahsan, P. Kosmas, J.A. Tobon-Vasquez, F. Vipiana, M. R Casu, and M. Vacca, "Application of the DBIM-TwIST algorithm to experimental MWI data," *2017 European Conference on Antennas Propagation (EuCAP)*, Paris, France, 2017, pp. 1611-1614. (Ch. 6)

Submitting Papers

(1) Z. Miao et al., "Assessing efficacy of the DBIM-TwIST algorithm using data from an experimental MWI prototype and its 3-D CAD equivalent". (Ch.6)

(2) Z. Miao, S, Ahsan, et al., "A frequency selection method to reduce errors in microwave tomography". (Ch.6)

(3) S. Ahsan, Z. Miao, et al., "Improving MWI reconstructions from an experimental prototype using a two-layer coupling medium". (Ch.6)

1.4 Thesis Structure

The remainder of the thesis is structured as follows. Chapter 2 presents background material and theories that are necessary for the development of our imaging algorithms and its validation and testing. Chapter 3 presents our novel microwave breast imaging algorithm based on an optimised two-step iterative shrinkage/thresholding method. Following that Chapter 4 presents an implementation of the multiple-frequency approach for MWI in various resolutions. Moreover, several improvement strategies based on the multiple-frequency DBIM-TwIST algorithm are presented in Chapter 5. Finally, Chapter 6 presents initial results from the application of the algorithm to data from a MWI experimental prototype.

Chapter 2

PRELIMINARIES AND RELATED WORK

2.1 Propagation of Electromagnetic Waves

This chapter will review some basic knowledge of microwave theory, while also introducing the FDTD method, which is employed to simulate the propagation of electromagnetic waves as a forward solution in this thesis.

In the case of MWI, a so-called excitation signal (a known signal) is transmitted from one Tx antenna to a set of Rx antennas (sometimes including the Tx antenna). By traversing the object under examination, the wave collects information about the structural morphology and also about the current condition of the object. For example, the information of interest is the health condition of the brain tissues. However, the information obtained by a measurement with a microwave system contains much more information; for example, head and brain shape and internal structure. This chapter will briefly overview the mechanisms of microwave propagation and scattering to understand how the content of the information could be extracted later.

2.1.1 Maxwell Equations

Maxwell's Equations govern EM propagation through a set of laws described below:

$$\begin{aligned} J + \frac{\partial D}{\partial t} &= \nabla \times H && \text{(Faraday's Law)} \\ \frac{\partial B}{\partial t} &= -\nabla \times E && \text{(Ampère's circuital law)} \\ \nabla \cdot B &= 0 && \text{(Gauss's law for magnetism)} \\ \nabla \cdot D &= \rho && \text{(Gauss's law)} \end{aligned} \tag{2.1}$$

In (2.1), D is the electric displacement field, r, the charge density, H, the magnetic field, J, current density, E, the electric field and t denotes time [83]. If the material properties are known, every electromagnetic field problem with defined boundary conditions can be solved by finding a solution for this system of coupled partial differential equations. This is often a difficult task, and in most cases a closed solution does not exist. The only option to deal with such circumstances is to approximate the underlying problem and its solution. A common way to deal with differential equations is to approximate them numerically, by the method of finite differences.

A differential form in rectangular coordinates is shown below.

$$\begin{aligned} \mu\frac{\partial H_x}{\partial t} &= \frac{\partial E_y}{\partial z} - \frac{\partial E_z}{\partial y} - \sigma_m H_x - M_x \\ \mu\frac{\partial H_y}{\partial t} &= \frac{\partial E_z}{\partial x} - \frac{\partial E_z}{\partial y} - \sigma_m H_y - M_y \\ \mu\frac{\partial H_z}{\partial t} &= \frac{\partial E_x}{\partial y} - \frac{\partial E_z}{\partial y} - \sigma_m H_z - M_z \\ \epsilon\frac{\partial E_x}{\partial t} &= \frac{\partial H_z}{\partial y} - \frac{\partial H_y}{\partial z} - \sigma_e E_x - J_x \\ \epsilon\frac{\partial E_y}{\partial t} &= \frac{\partial H_x}{\partial z} - \frac{\partial H_z}{\partial x} - \sigma_e E_y - J_y \\ \epsilon\frac{\partial E_z}{\partial t} &= \frac{\partial H_y}{\partial x} - \frac{\partial H_x}{\partial y} - \sigma_e E_z - J_z \end{aligned} \tag{2.2}$$

2.1.2 Finite-Difference Time-Domain Method

One of the oldest numerical approximations for electromagnetic field problems is the FDTD method. As the name suggests this method approximates the derivatives by finite differences. This can be performed by defining a sufficiently small step Δx and then taking the result of the approximated function f around the point of interest x. The approximated derivative at x, for example, can be written as

$$\frac{\partial f}{\partial x} \approx \frac{f(x + \Delta x) - f(x)}{\Delta x}. \tag{2.3}$$

By performing this in this particular way, the defined approximation of the derivative is called the forward difference. Two other such definitions exist, the backward difference

$$\frac{\partial f}{\partial x} \approx \frac{f(x) - f(x - \Delta x)}{\Delta x} \tag{2.4}$$

and the central

$$\frac{\partial f}{\partial x} \approx \frac{f(x + \Delta x) - f(x - \Delta x)}{2\Delta x}. \tag{2.5}$$

All finite difference methods are based on at least one of these approximations. Combining these difference operators can derive higher order derivatives.

It was Kane S. Yee who first defined a scheme to discretise the fields and solve Maxwell's equation numerically. He introduced the lattice shown in Fig. 2.1 [84]. Because the components of the fields are calculated at different points, a separate calculation of the electric and the magnetic fields are possible. Currently, this lattice is the standard applied when models are discretised for FDTD calculations. Certain side conditions must be fulfilled, which are mainly set by the maximal wavelength. This is included in the set-up simulation. To achieve representative results with FDTD simulations a

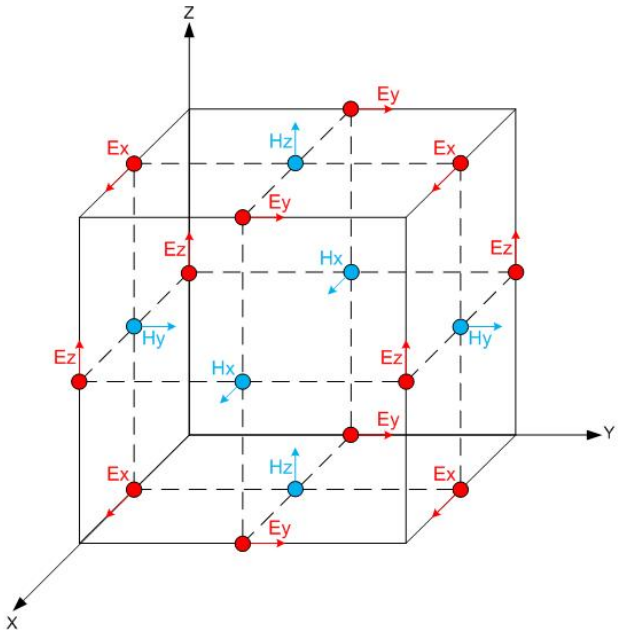

Figure 2.1: Lattice defined by Yee in 1966 which shows various positions of field components. The components of the electric field (red circle) are calculated in the middle of the edges and the components of the magnetic field (blue circle) are centred on the surfaces.(*source: fdtd.wikispaces.com*)

maximum time step Δt, that fulfils the following inequality

$$\Delta t \leq \frac{1}{u\sqrt{\frac{1}{(\Delta x)^2} + \frac{1}{(\Delta y)^2} + \frac{1}{(\Delta z)^2}}} \tag{2.6}$$

must be used. Here u denotes the velocity of propagation and Δx, Δy and Δz are the spatial dimensions of the smallest element of the grid of the simulation [85].

2.1.3 Convolutional Perfectly Matched Layer

One of the greatest challenges of the FDTD method has been the generation of an efficient and accurate solution of electromagnetic wave interaction problems in unbounded regions. For such problems, an absorbing boundary condition (ABC) must be introduced at the outer lattice boundary to simulate the extension of the lattice to infinity. A number of analytical techniques have been discussed to achieve this goal in [86–91].

An alternate approach to achieve an ABC is to terminate the outer boundary of the space lattice in an absorbing material medium. This is analogous to the physical treatment of the walls of an anechoic chamber. Ideally, the absorbing medium is only a few lattice cells thick, reflectionless to all impinging waves over their full frequency spectrum, highly absorbing, and effective in the near field of a source or a scatterer. An early attempt at implementing such an absorbing material boundary condition was reported by Holland [86], who used a conventional lossy dispersionless absorbing medium. The difficulty with this tactic is that such an absorbing layer is matched only to normally incident plane waves. As a result, the entire category of lossy material ABCs had only limited electromagnetic application.

In 1994, a breakthrough in this area was created by Berenger's introduction of a highly effective absorbing-material ABC designated the perfectly matched layer (PML) [92]. The innovation of Berenger's PML is that plane waves of arbitrary incidence, polarisation and frequency are matched at the boundary. Perhaps of equal importance is that the PML can be used as an absorbing boundary to terminate domains comprised of inhomogeneous, dispersive, anisotropic and even non-linear media, which was previously not possible with analytically derived ABCs.

In this thesis, a more efficient implementation is applied as previously published by Roden and Gedney in [93] based on a recursive convolution technique. This has since been referred to as the CPML formulation. The CPML is based on the stretched-coordinate form of Maxwell's equations as proposed in (2.2). One example is illustrated below

$$\epsilon \frac{\partial}{\partial t} E_x + \sigma E_x = s_y(t) * \frac{\partial}{\partial y} H_z - s_z(t) * \frac{\partial}{\partial z} H_y. \tag{2.7}$$

where the choice of the complex stretching variable will be as proposed by Kuzuoglu and Mittra. Specifically, it is assumed that

$$s_i = \kappa_i + \frac{\sigma_i}{\alpha_i + j\omega\epsilon_0}, \qquad i = x,\ y,\ or\ z \tag{2.8}$$

Finally, according to the conclusion in [93], the CPML formulation is generated as follows

$$\begin{aligned}\epsilon_r\epsilon_0\frac{E^{n+1}_{x_{i+1/2,j,k}}-E^{n}_{x_{i+1/2,j,k}}}{\Delta t}+\sigma\frac{E^{n+1}_{x_{i+1/2,j,k}}+E^{n}_{x_{i+1/2,j,k}}}{\Delta t}=\\ \frac{H^{n+1/2}_{z_{i+1/2,j+1/2,k}}-H^{n+1/2}_{z_{i+1/2,j-1/2,k}}}{\kappa_y\Delta y}-\frac{H^{n+1/2}_{y_{i+1/2,j,k+1/2}}-H^{n+1/2}_{y_{i+1/2,j,k-1/2}}}{\kappa_z\Delta z}+\\ \sum_{m=0}^{N-1}Z_{0_y}(m)\frac{H^{n-m+1/2}_{z_{i+1/2,j+1/2,k}}-H^{n-m+1/2}_{z_{i+1/2,j-1/2,k}}}{\Delta y}+\sum_{m=0}^{N-1}Z_{0_y}(m)\frac{H^{n-m+1/2}_{y_{i+1/2,j,k+1/2}}-H^{n-m+1/2}_{y_{i+1/2,j,k-1/2}}}{\Delta z}.\end{aligned}\tag{2.9}$$

Fortunately, $z_{0_i}(m)$ can be performed recursively using the recursive convolution method [94, 95]. The set of auxiliary expressions ψ_i is introduced, and Equation 2.9 is implemented as another form

$$\begin{aligned}\epsilon_r\epsilon_0\frac{E^{n+1}_{x_{i+1/2,j,k}}-E^{n}_{x_{i+1/2,j,k}}}{\Delta t}+\sigma\frac{E^{n+1}_{x_{i+1/2,j,k}}+E^{n}_{x_{i+1/2,j,k}}}{\Delta t}=\\ \frac{H^{n+1/2}_{z_{i+1/2,j+1/2,k}}-H^{n+1/2}_{z_{i+1/2,j-1/2,k}}}{\kappa_y\Delta y}-\frac{H^{n+1/2}_{y_{i+1/2,j,k+1/2}}-H^{n+1/2}_{y_{i+1/2,j,k-1/2}}}{\kappa_z\Delta z}+\\ +\psi^{n+1/2}_{e_{xy}{}_{i+1/2,j,k}}+\psi^{n+1/2}_{e_{xz}{}_{i+1/2,j,k}}\end{aligned}\tag{2.10}$$

where

$$\begin{aligned}\psi^{n+1/2}_{e_{xy}{}_{i+1/2,j,k}}&=b_y\psi^{n-1/2}_{e_{xy}{}_{i+1/2,j,k}}+a_y(H_{z_{i+1/2,j+1/2,k}}-H_{z_{i+1/2,j-1/2,k}})/\Delta y\\ \psi^{n+1/2}_{e_{xz}{}_{i+1/2,j,k}}&=b_z\psi^{n-1/2}_{e_{xz}{}_{i+1/2,j,k}}+a_z(H_{y_{i+1/2,j+1/2,k}}-H_{y_{i+1/2,j-1/2,k}})/\Delta z\\ b_i&=e^{-((\sigma_i/\kappa_i)+\alpha_i)(\Delta t/\epsilon_0)},\quad (i=x,\ y,\ or\ z)\end{aligned}\tag{2.11}$$

and a_i is shown by

$$a_i=\frac{\sigma_i}{\sigma_k\kappa_i^2\alpha_i}(e^{-((\sigma_i/\kappa_i)+\alpha_i)(\Delta t/\epsilon_0)}-1.0).\tag{2.12}$$

2.1.4 Two-Dimensional FDTD Modelling in Dispersive Media

In this thesis, the two-dimensional (2-D) FDTD is implemented in MATLAB to model EM propagation in the forward solver of the MWI algorithm (see Section 2.4). The former three sections outline the basic theories and derivations involved in the complete

modelling of FDTD. This section will cover all the formulations grouped with CPML and dispersive media in TM mode. The explicit update for H in x-projection is also shown below.

$$H_x^{n+1/2}(i,j+1/2) = D_a(i,j+1/2)\cdot H_x^{n-1/2} - D_b(i,j+1/2)\cdot \left[\frac{E_z^n(i,j+1)-E_z^n(i,j)}{\kappa_{y_{j+1/2}}\Delta y} + \Psi_{H_{xy}}^n(i,j+1/2)\right] \tag{2.13}$$

where

$$\begin{aligned} D_a(i,j+1/2) &= (1-\frac{\sigma^*_{(i,j+1/2)}\Delta t}{2\mu_{(i,j+1/2)}})/(1+\frac{\sigma^*_{(i,j+1/2)}\Delta t}{2\mu_{(i,j+1/2)}}) \\ D_b(i,j+1/2) &= (\frac{\Delta t}{\mu_{i,j+1/2}})/(1+\frac{\sigma^*_{i,j+1/2}\Delta t}{2\mu_{(i,j+1/2)}}) \\ \kappa_y(p) &= 1+(\kappa_{y,max}-1)\cdot(\frac{p}{d})^m \\ \Psi_{H_{xy}}^n(i,j+1/2) &= b_{y_{j+1/2}}\cdot\Psi_{H_{xy}}^{n-1}(i,j+1/2) + c_{y_{j+1/2}}\left[\frac{E_z^n(i,j+1)-E_z^n(i,j)}{\Delta y}\right] \end{aligned} \tag{2.14}$$

Note that σ^* denotes magnetic losses relative to σ as the electric conductivities. In this thesis, the magnetic loss is set to zero as $\sigma^* = 0$. κ_y uses a polynomial or geometric variation with a PEC-backed PML slab of thickness d, with the front planar interface located in the $p = 0$. It increases from 1 at $p = 0$, the inner surface of the CPML, to $\kappa_{y,max}$ at $p = d$, the PML outer boundary. In Equation 2.14, b_y and c_y are computed for the update of PML layer by

$$\begin{aligned} b_w &= e^{-(\frac{\sigma_w}{\epsilon_0\kappa_w}+\frac{\alpha_w}{\epsilon_0})\cdot\Delta t} \\ c_w &= \frac{\sigma_w}{\sigma_w\kappa_w+\kappa_w^2\alpha_w}(b_w-1) \end{aligned} \tag{2.15}$$

Similarly, the update for H in y-projection is also shown. The parameters are computed in the same form.

$$H_y^{n+1/2}(i+1/2,j) = D_a(i+1/2,j)\cdot H_x^{n-1/2} - D_b(i+1/2,j)\cdot \left[\frac{E_z^n(i+1,j)-E_z^n(i,j)}{\kappa_{x_{i+1/2}}\Delta x} + \Psi_{H_{yx}}^n(i+1/2,j)\right] \tag{2.16}$$

In this thesis, the 2-D FDTD simulation is excited by point sources with a wideband Gaussian pulse in a TM configuration (i.e. the electric field is perpendicular to the breast phantom) in the frequency range between 0.5 and 3.5 GHz. Therefore, there is only one projection of electric field, E_z, which is given by

$$E_z^{n+1}(i,j) = C_a(i,j)\cdot E_z^n(i,j) + C_b\cdot \left[\frac{H_y^{n+\frac{1}{2}}(i+\frac{1}{2},j) - H_y^{n+\frac{1}{2}}(i-\frac{1}{2},j)}{\kappa_x(i)\Delta x} - \frac{H_x^{n+\frac{1}{2}}(i,j+\frac{1}{2}) - H_x^{n+\frac{1}{2}}(i,j-\frac{1}{2})}{\kappa_y(j)\Delta y} + \Psi_{E_{zx}}^{n+\frac{1}{2}}(i,j) - \Psi_{E_{zy}}^{n+\frac{1}{2}}(i,j) - \frac{1}{2}(1+K_d)J_d^n(i,j)\right] \tag{2.17}$$

where

$$\begin{aligned} C_a(i,j) &= \frac{2\epsilon_0\epsilon_\infty(i,j) - \sigma_s(i,j)\Delta t + \beta_d(i,j)}{2\epsilon_0\epsilon_\infty(i,j) + \sigma_s(i,j)\Delta t + \beta_d(i,j)} \\ C_b(i,j) &= \frac{2\Delta t}{2\epsilon_0\epsilon_\infty(i,j) + \sigma_s(i,j)\Delta t + \beta_d(i,j)} \\ \kappa_x(p) &= 1 + (\kappa_{x,max}-1)\cdot(\frac{p}{d})^m \\ \kappa_y(p) &= 1 + (\kappa_{y,max}-1)\cdot(\frac{p}{d})^m \\ \Psi_{E_{zx}}^{n+\frac{1}{2}}(i,j) &= b_{xi}\cdot\Psi_{E_{zx}}^{n-\frac{1}{2}}(i,j) + C_{xi}\left[\frac{H_y^{n+\frac{1}{2}}(i+\frac{1}{2},j) - H_y^{n+\frac{1}{2}}(i-\frac{1}{2},j)}{\Delta x}\right] \\ \Psi_{E_{zy}}^{n+\frac{1}{2}}(i,j) &= b_{yj}\cdot\Psi_{E_{zy}}^{n-\frac{1}{2}}(i,j) + C_{yj}\left[\frac{H_x^{n+\frac{1}{2}}(i,j+\frac{1}{2}) - H_x^{n+\frac{1}{2}}(i,j-\frac{1}{2})}{\Delta y}\right] \end{aligned} \tag{2.18}$$

$$
\begin{aligned}
K_d &= \frac{2\tau - \Delta t}{2\tau + \Delta t} \\
J_d^n(i,j) &= K_d \cdot J_d^{n-1}(i,j) + \beta_b\left(\frac{E_z^n(i,j) - E_z^{n-1}(i,j)}{\Delta t}\right) \\
\beta_b &= \frac{2\epsilon_0 \Delta\epsilon \Delta t}{2\tau + \Delta t}.
\end{aligned}
\tag{2.19}
$$

2.2 Debye Model

The main features of the dielectric spectrum of tissues are well-known and have been reviewed and reported by [96]. The dielectric spectrum of tissues is characterised by three main relaxation regions at low, medium and high frequencies. In its simplest form, each of these relaxation regions is the manifestation of a polarisation mechanism characterised by a single time constant τ. The Debye model and single-pole Cole–Cole model are commonly used to describe human tissues. This is because a lossy dispersive wave equation is conducted completely by the frequency-dependent conductivity. The Debye relation is used to model the dispersive behaviour of the complex relative permittivity of breast tissue [64]. The single-pole Cole–Cole model is defined as

$$
\begin{aligned}
\epsilon_r(\omega) &= \epsilon_r^{'}(\omega) - j\epsilon_r^{''}(\omega) \\
&= \epsilon_\infty + \frac{\epsilon_s - \epsilon_\infty}{1 + (j\omega\tau)^{1-\alpha}} + \frac{\sigma_s}{j\omega\epsilon_0}
\end{aligned}
\tag{2.20}
$$

where ω is the angular frequency, $\epsilon^{'}(\omega)$ is the frequency-dependent dielectric constant, and $\epsilon^{''}(\omega)$ is the frequency-dependent dielectric loss which can be converted into the effective conductivity, $\sigma(\omega) = \omega\epsilon_0\epsilon^{''}(\omega)$. Note that α is a fitting parameter. In many cases such as biological tissue within certain frequency ranges, the Cole-Cole model in (2.20) can be simplified to a single-pole Debye model by setting $\alpha = 1$ in (2.20) [34]

$$
\begin{aligned}
\frac{\epsilon(\omega)}{\epsilon_0} &= \epsilon_\infty + \frac{\epsilon_s - \epsilon_\infty}{1 + j\omega\tau} + \frac{\sigma_s}{j\omega\epsilon_0} \\
&\equiv \epsilon_\infty + \frac{\Delta\epsilon}{1 + j\omega\tau} + \frac{\sigma_s}{j\omega\epsilon_0}
\end{aligned}
\tag{2.21}
$$

where ϵ_s is the zero-frequency relative permittivity and ϵ_∞ is the relative permittivity at infinite frequency. τ is the pole relaxation time and σ_s denotes the static conductivity. Finally, ω denotes angular frequency. In this thesis, the frequency range of interest for the MWI is from 0.5 to 3.5 GHz.

For this study, the approximations of the Debye model of different breast tissues were obtained from the University of Wisconsin Cross-Disciplinary Electromagnetics Laboratory (UWCEM), which provides a number of anatomically-realistic MRI-derived numerical breast phantoms for breast cancer detection and treatment applications. The breast tissues in these phantoms have the realistic ultra wideband dielectric properties reported in [97].

2.3 Numerical Breast Phantoms

The numerical breast phantoms are derived from 3-D MRI datasets from patients with different breast tissue density classifications, based on the American College of Radiology's BI-RADS system [98]. A number of anatomically realistic MRI-derived numerical breast phantoms are applied for breast cancer detection and treatment applications. The phantoms are classified into four groups: 'mostly fatty', 'scattered fibroglandular', 'heterogeneously dense' and 'very dense', as illustrated by the 3-D model from Fig. 2.3 to Fig. 2.6, respectively.

The numerical breast phantoms are created following the procedures reported in [99–101]. The intensity of the voxels in each MRI dataset is converted to dispersive dielectric properties via a piecewise linear mapping. A single-pole Debye model (2.21) is used to describe the frequency-dependent behaviour of the dielectric properties of all the biological tissues in the computational model. In this study, a spatially invariant relaxation time constant of $\tau = 17.125ps$ for FDTD algorithmic simplicity and efficiency. The frequency dependence of the complex permittivity of the constituent tissues is illustrated in Fig. 2.2, and their Debye parameters are listed in Table 2.1. The interior of

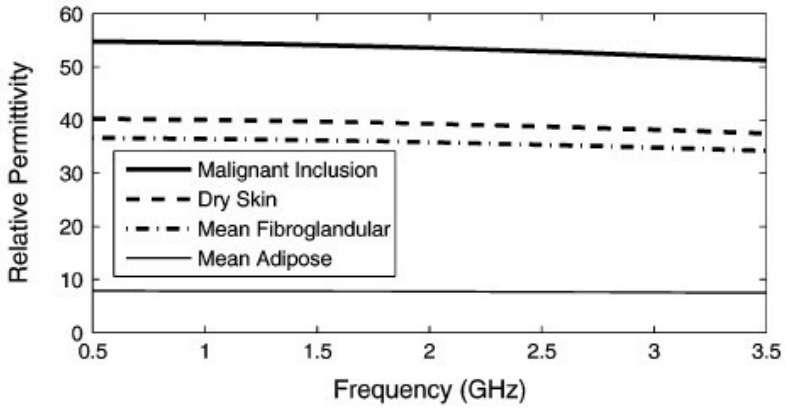

(a)

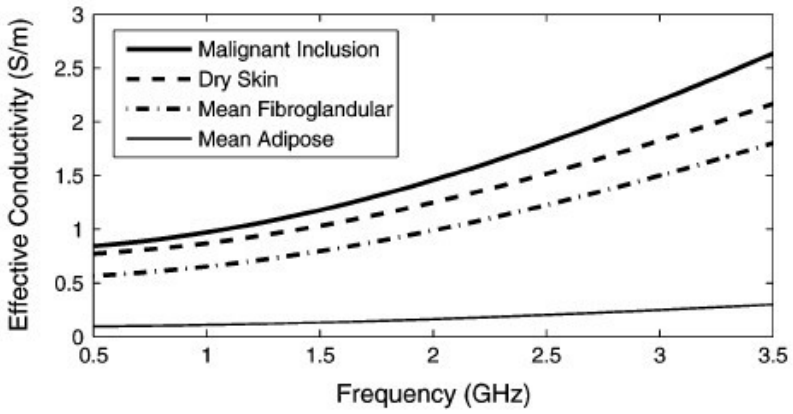

(b)

Figure 2.2: Frequency dependence of the single-pole Debye tissue models used in the numerical breast phantoms. (a) ϵ_r and (b) σ_{eff}. The curves for adipose and fibroglandular tissues represent the mean of the full mapping range from the raw MRI data.

Table 2.1: The Debye parameters of the media modelled in the computational testbeds (valid for the frequency range of 0.5 – 3.5 GHz).

Material	ϵ_∞	$\Delta\epsilon$	$\sigma_s(S/m)$	$\tau(ps)$
Adipose tissue (min)	2.28	1.3	0.0023	17.125
Adipose tissue (mean)	4.68	3.21	0.0881	17.125
Fibroglandular tissue (mean)	17.3	19.4	0.535	17.125
Dry skin	18.4	21.9	0.737	17.125
Malignant inclusion	23.2	33.6	0.801	17.125
Coupling medium	2.6	0.0	0.0	17.125

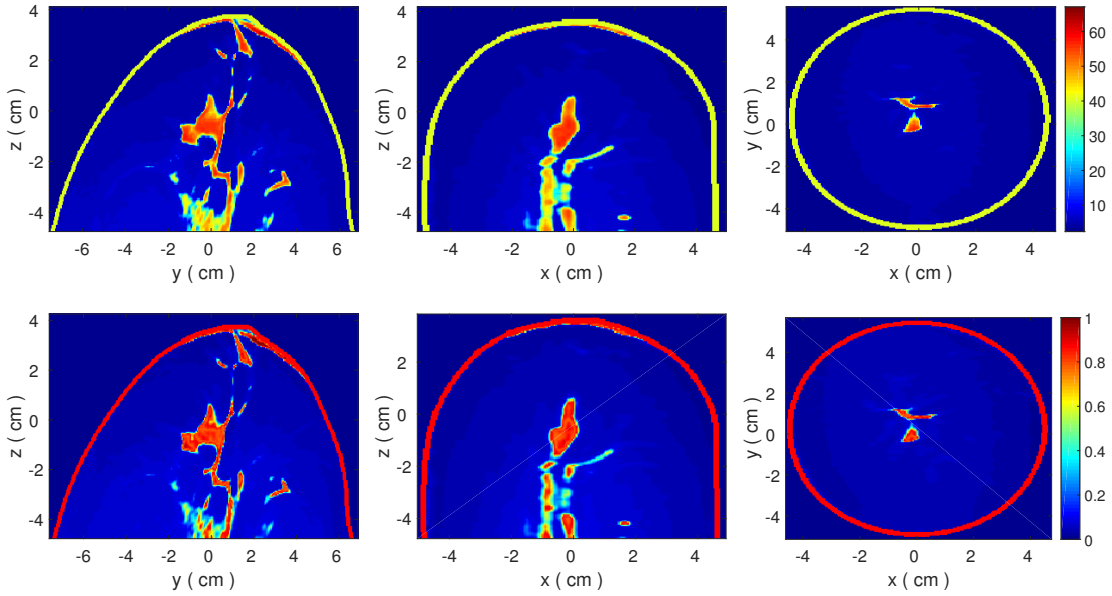

Figure 2.3: Relative permittivity and effective conductivity of the mostly fatty 3-D numerical breast phantom distributions at 1.0 GHz. (a) ϵ_r in $y-z$ plane. (b) ϵ_r in $x-z$ plane. (c) ϵ_r in $x-y$ plane. (d) σ_{eff} in $y-z$ plane. (e) σ_{eff} in $x-z$ plane. (f) σ_{eff} in $x-y$ plane.

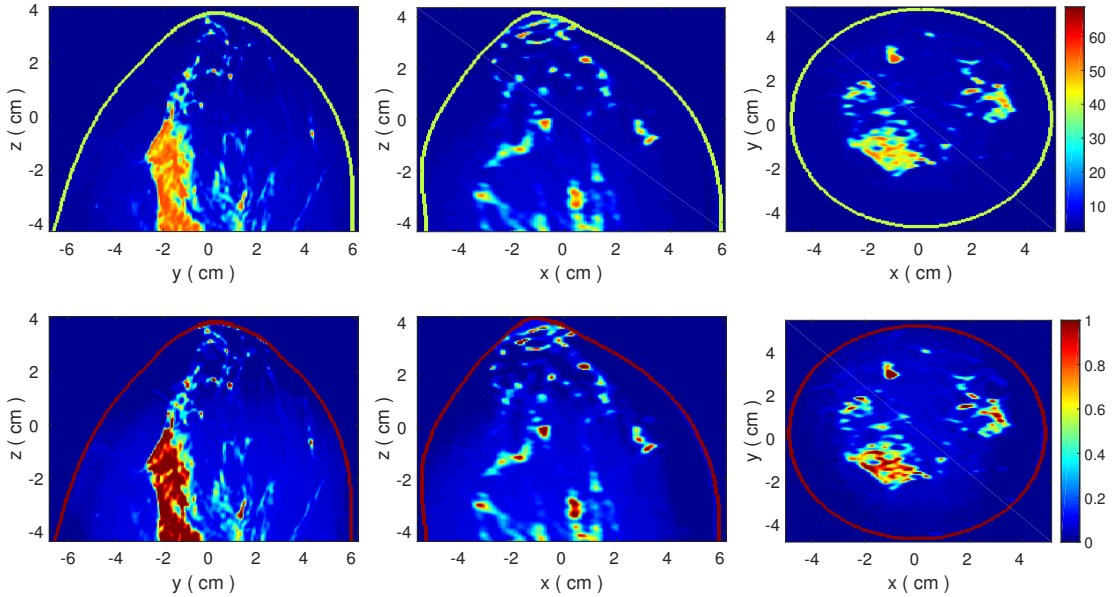

Figure 2.4: Relative permittivity and effective conductivity of the scattered fibroglandular 3-D numerical breast phantom distributions at 1.0 GHz. (a) ϵ_r in $y-z$ plane. (b) ϵ_r in $x-z$ plane. (c) ϵ_r in $x-y$ plane. (d) σ_{eff} in $y-z$ plane. (e) σ_{eff} in $x-z$ plane. (f) σ_{eff} in $x-y$ plane.

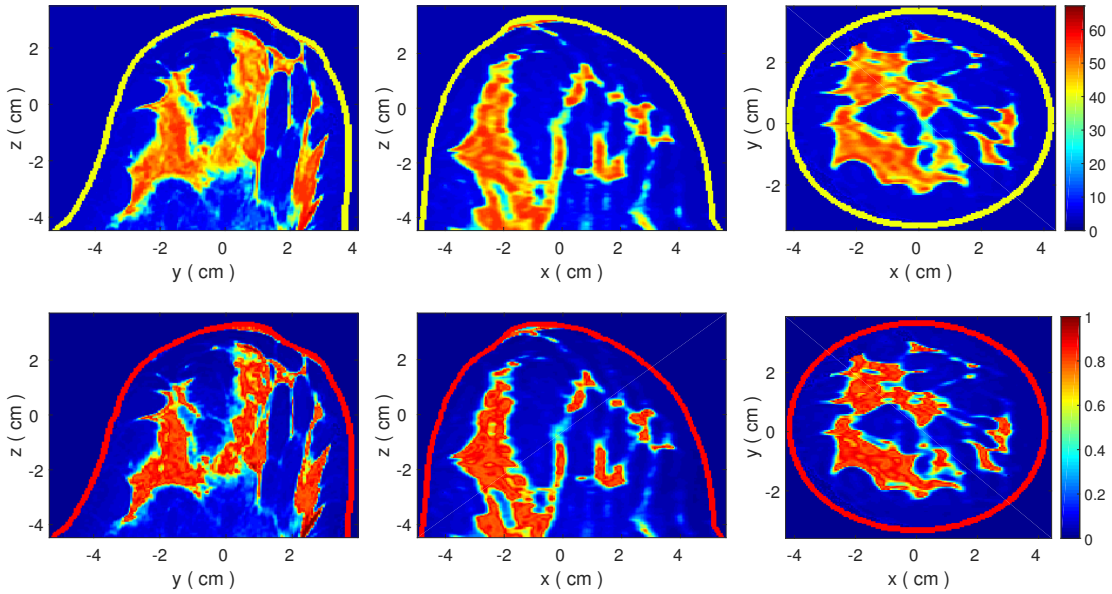

Figure 2.5: Relative permittivity and effective conductivity of the heterogeneously dense 3-D numerical breast phantom distributions at 1.0 GHz. (a) ϵ_r in $y-z$ plane. (b) ϵ_r in $x-z$ plane. (c) ϵ_r in $x-y$ plane. (d) σ_{eff} in $y-z$ plane. (e) σ_{eff} in $x-z$ plane. (f) σ_{eff} in $x-y$ plane.

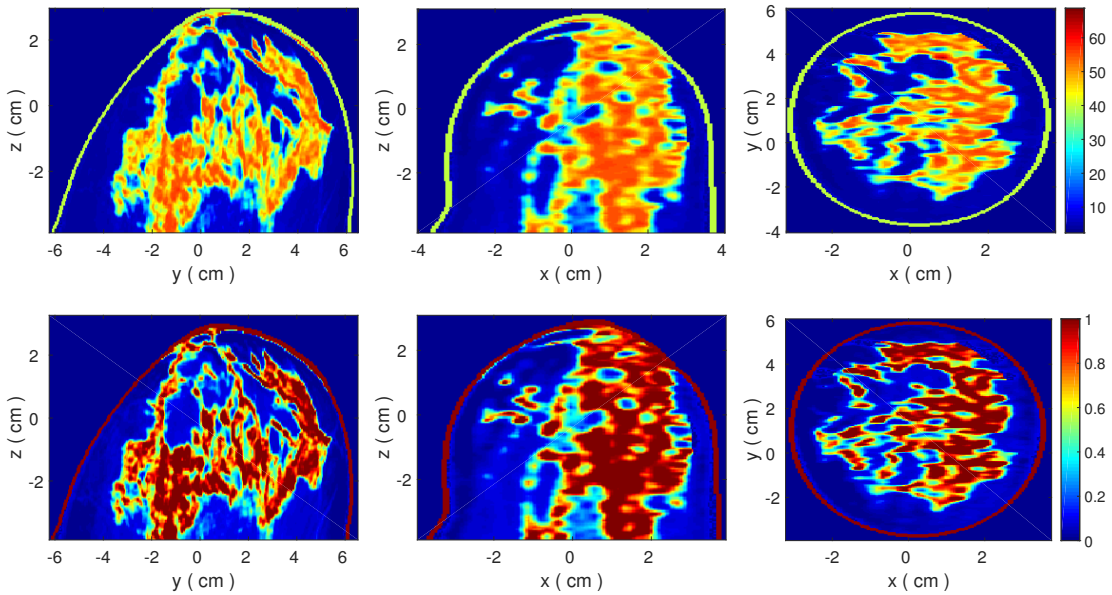

Figure 2.6: Relative permittivity and effective conductivity of the very dense 3-D numerical breast phantom distributions at 1.0 GHz. (a) ϵ_r in $y-z$ plane. (b) ϵ_r in $x-z$ plane. (c) ϵ_r in $x-y$ plane. (d) σ_{eff} in $y-z$ plane. (e) σ_{eff} in $x-z$ plane. (f) σ_{eff} in $x-y$ plane.

each breast phantom is segmented into three distinct regions: adipose, fibroglandular and transition. Here, the dielectric properties adopted are those reported in a recent large-scale dielectric spectroscopy study [97] for the adipose and fibroglandular regions in the models utilised. Voxels in the transition region are mapped to the range spanning the maximum of the adipose range to the minimum of the fibroglandular range. The Debye parameters for adipose tissue are derived by first averaging all the Cole–Cole curves from the large-scale tissue study [97] that correspond to breast tissue samples with 85%—100% adipose tissue, and then fitting a Debye model with $\tau = 17.125ps$ to the averaged curve over the frequency range of 0.5 GHz–3.5 GHz. The Debye parameters for fibroglandular tissue result from applying the same procedure.

The 2 mm thick skin layer is modelled using the dielectric properties for dry skin [102], which were approximated with the Debye parameters given in Table 2.1. The dielectric properties assigned to the spherical inclusions are adapted from a recent study [97] and are representative of malignant breast tissue properties in our frequency range of interest.

2.4 Inverse Scattering Problems

When a bounded medium is highly inhomogeneous, there are several methods used to resolve its scattering. One way is to approximate the inhomogeneous medium with N scatterers and seek its scattering solution. An alternative approach is to use volume integral equations where the unknowns in the problem are expressed in terms of the flowing current volume in the inhomogeneity. The current volume consists of the conduction current and the displacement current induced by the total electric field shown in Fig. 2.7 from [103]. An integral equation can then be formulated from which the total field is solved. This process involves the formulation of the integral equation for the electromagnetic wave case. Historically, the volume integral equation method was developed as early as 1913 by Esmarch [104].

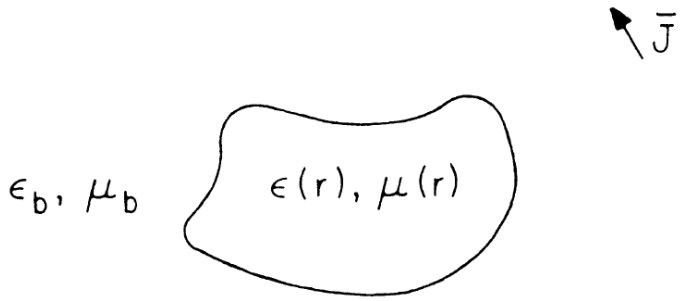

Figure 2.7: A current source radiating in the vicinity of a general inhomogeneity

2.4.1 Mathematical Formulation of EM Scattering

We first demonstrate how the corresponding integral equation can be derived for a finite-size, inhomogeneous scatterer for the electromagnetic wave case shown in Fig. 2.7. From Maxwell's equations, it follows that the electric field everywhere satisfies the following equation,

$$\nabla \times \mu^{-1} \nabla \times E(\boldsymbol{r}) - \omega^2 \epsilon E(\boldsymbol{r}) = i\omega J(\boldsymbol{r}), \tag{2.22}$$

where μ and ϵ are functions of position inside the inhomogeneous region V. Next, subtracting $\nabla \times \mu_b^{-1} \nabla \times E(\boldsymbol{r}) - \omega^2 \epsilon_b E(\boldsymbol{r})$ from both sides of the equation, the following is achieved

$$\nabla\times(mu^{-1}-\mu_b^{-1})\nabla\times E(\boldsymbol{r})-\omega^2(\epsilon-\epsilon_b)E(\boldsymbol{r}) = i\omega J(\boldsymbol{r})-\nabla\times\mu_b^{-1}\nabla\times E(\boldsymbol{r})+\omega^2\epsilon_b E(\boldsymbol{r}) \tag{2.23}$$

To formulate the integral equation, we must calculate the dyadic Green's function in the absence of the scatterer. The dyadic Green's function satisfies the equation

$$\nabla \times \mu_b^{-1} \nabla \times \bar{G}(\boldsymbol{r}, \boldsymbol{r}') - \omega^2 \epsilon \bar{G}(\boldsymbol{r}, \boldsymbol{r}') = \mu_b^{-1} \bar{I} \delta(\boldsymbol{r} - \boldsymbol{r}'). \tag{2.24}$$

The solution is

$$\begin{aligned} E(\boldsymbol{r}) =& i\omega \int_V d\boldsymbol{r}' \bar{G}(\boldsymbol{r}, \boldsymbol{r}') \cdot \mu_b \boldsymbol{J}(\boldsymbol{r}') + \omega^2 \int_V d\boldsymbol{r}' \bar{G}(\boldsymbol{r}, \boldsymbol{r}') \cdot (\epsilon - \epsilon_b) \boldsymbol{E}(\boldsymbol{r}') \\ & - \int_V d\boldsymbol{r}' \bar{G}(\boldsymbol{r}, \boldsymbol{r}') \cdot \mu_b \nabla' \times \left(\frac{1}{\mu} - \frac{1}{\mu_b} \right) \nabla' \times \boldsymbol{E}(\boldsymbol{r}') \end{aligned} \tag{2.25}$$

In the above, the first term is just the incident field. Hence, (2.25) becomes

$$\begin{aligned} \boldsymbol{E}(\boldsymbol{r}) = \boldsymbol{E}_{inc}(\boldsymbol{r}) + \omega^2 \int_V d\boldsymbol{r}' \bar{\boldsymbol{G}}(\boldsymbol{r},\boldsymbol{r}') \cdot (\epsilon - \epsilon_b)\boldsymbol{E}(\boldsymbol{r}') \\ - \int_V d\boldsymbol{r}' \bar{\boldsymbol{G}}(\boldsymbol{r},\boldsymbol{r}') \cdot \mu_b \bigtriangledown' \times \left(\frac{1}{\mu} - \frac{1}{\mu_b}\right) \bigtriangledown' \times \boldsymbol{E}(\boldsymbol{r}') \end{aligned} \tag{2.26}$$

The integrals in (2.26) are contributions to the field E from the volume current induced in the scatterer by the total electric field E and magnetic field H (note that $\bigtriangledown \times \boldsymbol{E} = i\omega\mu\boldsymbol{H}$). Hence, the first term is generated by the electric polarisation current or displacement current, while the second term is generated by the magnetic polarisation charges. When the scatterer is conductive such that $\epsilon = \epsilon' + i\sigma/\omega$, the first integral in (2.26) is due to the conduction current induced by the field as well. The two integrals can be combined by substituting the complex permittivity into (2.26) and identifying a term proportional to $\sigma\boldsymbol{E}$ corresponding to conduction currents. Moreover, our analysis focuses on materials that are non-magnetic, thus $\mu = \mu_b = 1$. Equation 2.26 simplifies to

$$\boldsymbol{E}(\boldsymbol{r}) = \boldsymbol{E}_{inc}(\boldsymbol{r}) + \int_V d\boldsymbol{r}' \bar{\boldsymbol{G}}(\boldsymbol{r},\boldsymbol{r}') \cdot O(\boldsymbol{r}')\boldsymbol{E}(\boldsymbol{r}'), \tag{2.27}$$

where $O(\boldsymbol{r}') = \omega^2(\epsilon - \epsilon_b)$. In an inverse scattering problem, only field data outside the scatterer are available, for instance, through a measurement scheme shown in Fig. 2.8. Then, the total field is related to the object via the volume integral equation (2.27). The integral above corresponds to the scattered field and is the only term that contains information on the scatterer, which is described by $O(\boldsymbol{r}) = \kappa^2(\boldsymbol{r}) - \kappa_b^2$, where $\kappa^2(\boldsymbol{r}) = \omega^2\mu(\boldsymbol{r})\epsilon(\boldsymbol{r})$ represents an inhomogeneous medium over a finite domain V. It is apparent that the scattered field is a non-linear functional of $O(\boldsymbol{r})$,because $E(\boldsymbol{r})$ itself is also a functional of $O(\boldsymbol{r})$.

The solution of the volume integral equation (2.27) usually has to be solved numerically. This is, in general, computationally intensive because in finding the matrix element N_{mn}, a double integration may have to be performed. For many problems, however,

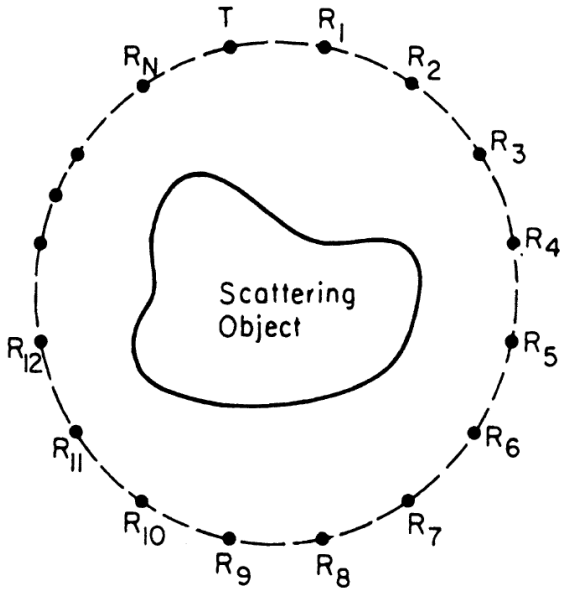

Figure 2.8: An example of an inverse scattering experiment

especially when the scattering from the inhomogeneity is weak, it suffices to derive approximate solutions to the scattering problem. To this end, this thesis employs the well-known Born approximation [104].

In the cases when $\kappa^2(\boldsymbol{r}) - \kappa_b^2$ is small, or where the contrast of the scatterer is weak so that the second term on the right of Equation 2.27 is small compared to the first term, it can be approximated by

$$\boldsymbol{E}(\boldsymbol{r}) \approx \boldsymbol{E}_{inc}(\boldsymbol{r}) \tag{2.28}$$

Then, the total field in Equation 2.27 can be approximately calculated as

$$\boldsymbol{E}(\boldsymbol{r}) = \boldsymbol{E}_{inc}(\boldsymbol{r}) + \int_V d\boldsymbol{r}' \bar{\boldsymbol{G}}(\boldsymbol{r}, \boldsymbol{r}') \cdot O(\boldsymbol{r}') \boldsymbol{E}_{inc}(\boldsymbol{r}') \tag{2.29}$$

The above is known as the first-order Born approximation. It is also the first order approximation in the Neumann series expansion of integral equation in (2.27).

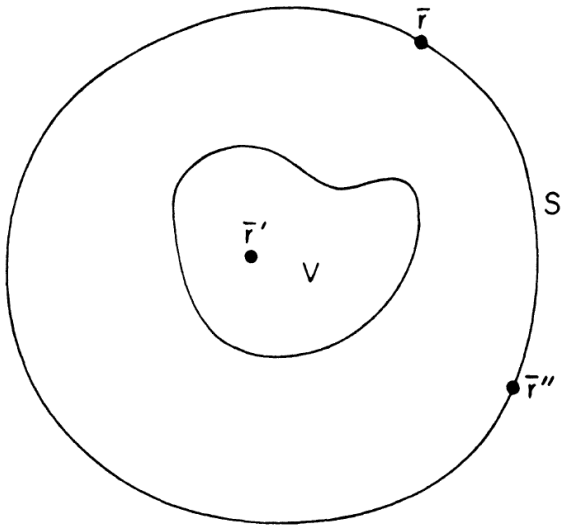

Figure 2.9: An inverse scattering experiment where the measurement data are obtained at $\boldsymbol{r}$ on S and the transmitter is at $\boldsymbol{r}''$

2.4.2 Distorted Born Iterative Method

The Born approximation assumes a linear integral equation, while the integral equation is non-linear in the object function being sought. To extend the Born approach to non-linear problems, iterative methods must be used to solve the non-linear equation. The most popular approach to this problem is the use of the DBIM [105].

To demonstrate the implementation of the DBIM, we start by the Born integral equation

$$\boldsymbol{E}(\boldsymbol{r}) = \boldsymbol{E}_{inc}(\boldsymbol{r}) + \int_V d\boldsymbol{r}' \bar{\boldsymbol{G}}(\boldsymbol{r}, \boldsymbol{r}', \epsilon_b) \cdot \left[\kappa^2(\boldsymbol{r}') - \kappa_b^2\right] \boldsymbol{E}_{inc}(\boldsymbol{r}'). \tag{2.30}$$

In this formulation, the measurement data are available only outside the scatterer in the inverse scattering problem. Therefore, the only item available is

$$\boldsymbol{E}_{sca}(\boldsymbol{r}) = \boldsymbol{E}(\boldsymbol{r}) - \boldsymbol{E}_{inc}(\boldsymbol{r}) \quad \boldsymbol{r} \in S, \tag{2.31}$$

where S is some surface outside V (see Fig. 2.9 from [103]). It is only the scattered field E_{sca} that bears information on the scatterer. Hence, it can be written as (2.30) as

$$\boldsymbol{E}_{sca}(\boldsymbol{r}) = \int_V d\boldsymbol{r}' \bar{\boldsymbol{G}}(\boldsymbol{r}, \boldsymbol{r}', \epsilon_b) \cdot \left[\kappa^2(\boldsymbol{r}') - \kappa_b^2\right] \boldsymbol{E}_{inc}(\boldsymbol{r}') \tag{2.32}$$

Now, the preceding equation is an integral equation linear in $\kappa^2(\boldsymbol{r}) - \kappa_b^2$. Moreover, the error in the above equation can be easily shown to be of the order $(\kappa^2(\boldsymbol{r}) - \kappa_b^2)^2$. In addition, for the special case where $\boldsymbol{E}_{inc}(\boldsymbol{r}')$ is generated by a point source a located at $\boldsymbol{r}'' \in S$, it can be written as

$$\boldsymbol{E}_{inc}(\boldsymbol{r}') = \bar{\boldsymbol{G}}(\boldsymbol{r}', \boldsymbol{r}'', \epsilon_b) \cdot a \tag{2.33}$$

Then this generates

$$\boldsymbol{E}_{sca}(\boldsymbol{r}) = \int_V d\boldsymbol{r}' \bar{\boldsymbol{G}}(\boldsymbol{r}, \boldsymbol{r}', \epsilon_b) \cdot \bar{\boldsymbol{G}}(\boldsymbol{r}', \boldsymbol{r}'', \epsilon_b) \cdot a \left[\kappa^2(\boldsymbol{r}') - \kappa_b^2\right] \quad \boldsymbol{r}, \boldsymbol{r}'' \in S \tag{2.34}$$

Because $\kappa^2(\boldsymbol{r})$ is a 3-D function with support on V, a single measurement of $\boldsymbol{E}_{sca}(\boldsymbol{r}, \boldsymbol{r}')$ for $\boldsymbol{r}$ on the surface S for a fixed $\boldsymbol{r}''$ is not sufficient to generate enough data to solve $\kappa^2(\boldsymbol{r})$. In other words, it is not expected that information will be accurately retrieved on a 3-D function from a 2-D function. Therefore, data for a range of $\boldsymbol{r}$ and $\boldsymbol{r}''$ are needed to reconstruct $\kappa^2(\boldsymbol{r})$ accurately. The problem may still be ill-posed. Therefore, the iterative method is applied to find $\kappa^2(\boldsymbol{r})$ approximately. However, the new $\kappa^2(\boldsymbol{r})$ can be used as the estimate κ_b^2. Then, a new $\bar{\boldsymbol{G}}(\boldsymbol{r}, \boldsymbol{r}', \epsilon_b)$ that corresponds to this new κ_b^2 in (2.34) has to be found. This new Green's function can then be found. This iterative procedure is similar to Newton's method for solving a non-linear integral equation, except that the solution is regularised at every iteration.

Specifically, the inhomogeneous Green's function $\bar{\boldsymbol{G}}(\boldsymbol{r}, \boldsymbol{r}', \epsilon_b)$ has a simple relationship with the internal electric field. From the differential equations governing the Green's

function and electric field, the following is easily obtained

$$\bar{G}(\boldsymbol{r}, \boldsymbol{r}', \epsilon_b) \approx \frac{i}{\omega\mu} \boldsymbol{E}_a(\boldsymbol{r}, \boldsymbol{r}', \epsilon_b) \tag{2.35}$$

where $\boldsymbol{E}_a(\boldsymbol{r}, \boldsymbol{r}', \epsilon_b)$ is the total electric field at the receivers generated by a 2-D point source in the reconstruction domain filled by the background medium. Using the reciprocity theorem, the above equation directly gives [34]

$$\bar{G}(\boldsymbol{r}, \boldsymbol{r}', \epsilon_b) \approx \frac{i}{\omega\mu} \boldsymbol{E}_b(\boldsymbol{r}', \boldsymbol{r}, \epsilon_b) \tag{2.36}$$

Finally, (2.34) can be discretised, e.g., via the Riemann sum under the assumption that all quantities are constant over the discrete volume elements of the mesh. Discretisation of (2.34) for all Tx-Rx pairs results in the following set of linear equations:

$$\boldsymbol{b}(\omega) = \boldsymbol{A}(\omega)\boldsymbol{o}. \tag{2.37}$$

In (2.37), $\boldsymbol{A}(\omega)$ is an M-by-K matrix, where M is the number of Tx-Rx pairs in the antenna array and K denotes the number of elements in the discretisation, namely unknown dielectric properties contrasting inside the breast. While $\boldsymbol{b}(\omega)$ is an M-by-1 vector whose elements are equal to the residual scattered field E_s.

Solving (2.37) results in a discrete approximation $\hat{o}$ of the true distribution of contrast $\boldsymbol{o}(\boldsymbol{r})$. The approximation may be improved by adding $\hat{o}$ to the background and using FDTD simulation to calculate the new background electric field and inhomogeneous Green's function for the new background profile $\epsilon_b + \hat{\boldsymbol{o}}$. The iterative application of this sequence of computations forms the basis of the DBIM.

The DBIM algorithm begins with an initial assumption ϵ_{b_0} of the background profile. At the i_{th} iteration the background electric field and the Green's function are computed

for the background profile ϵ_{b_i}, and the associated equation is given by

$$\boldsymbol{A}_i(\omega)\boldsymbol{o}_{i+1} = \boldsymbol{b}_i(\omega) \tag{2.38}$$

where $\boldsymbol{A}_i(\omega)$ is the discretisation of (2.34) for $\boldsymbol{G}_b$ and $\boldsymbol{E}_b$, and the vector $\boldsymbol{b}_i(\omega)$ contains the residual scattered fields due to the background profile ϵ_{bi}. Then the background profile is updated as

$$\epsilon_{bi+1} = \epsilon_{bi} + \hat{\boldsymbol{o}}_{i+1} \tag{2.39}$$

2.5 Iterative Method to Solve Linear Problem

2.5.1 Linear Problem Description

We consider solving for the n-vector x in the system of linear equations

$$Ax = b \tag{2.40}$$

when the $n \times n$ real symmetric matrix A is large and sparse, or represents an operator for forming products Av. When the real vector b is in the range of A, it is said that the system is consistent or compatible; otherwise it is inconsistent or incompatible. When A is non-singular, the system is always consistent and the solution of (2.40) is unique.

When A is singular and (2.40) has at least one solution, and then the singular system is consistent or compatible, in which case it has infinitely many solutions. To obtain a unique solution, the minimum-length solution among all solutions x is selected in $\mathbb{R}^n$ such that $Ax = b$. On the other hand, if the singular system has no solution, it is thus referred to as inconsistent or incompatible, in which case the singular symmetric least-squares problem is solved instead and the minimum-length solution is selected:

$$x = \arg\min \|Ax - b\|_2. \tag{2.41}$$

More precisely, the minimum-length least-squares problem is defined as

$$\min \|x\|_2 \quad \text{s.t.} \quad x \in \arg\min \|Ax - b\|_2, \tag{2.42}$$

or with the more commonly seen but actually a slight abuse of notation

$$\min \|x\|_2 \quad \text{s.t.} \quad x = \arg\min \|Ax - b\|_2, \tag{2.43}$$

When A is linear, a linear inverse problem (LIP) is generated. Many approaches to LIPs define a solution $\hat{x}$ as a minimiser of a convex object function $f\colon X = \mathbb{R}^m$, given by

$$f(x) = \frac{1}{2}\|Ax - b\|^2 + \lambda\Phi(x) \tag{2.44}$$

where $\lambda \in [0, +\infty]$ is the parameter of the penalty term. In a regularisation framework, minimising f is seen as a way of overcoming the ill-conditional, or singular, nature of A, which precludes inverting it. In this context, Φ is called the regulariser and λ the regularisation parameter [106].

2.5.2 Direct vs Iterative Methods

Direct methods for solving systems of linear equations try to find the exact solution and carry out a fixed amount of computations, such as using the Gaussian elimination method. The errors introduced during computation can accumulate and render the method unusable for very large systems of equations. In addition, the number of arithmetic operations to be performed to solve a large system using direct methods may become infeasible. In the case where many of the coefficients a_{ij} are zero, this approach may also be redundant.

Iterative methods try to identify the solution by generating a sequence of vectors that are approximate solutions to the system of equations. These methods seek to approach the actual solution as rapidly and as accurately as possible. This means the algorithm can

be stopped once the sequence of vectors approaches a solution that is close enough to the actual solution. In addition, iterative methods can sometimes take better advantage of the structure found in the matrix. Many matrices in practice, especially when considering physical models, are sparse, meaning that most of the coefficients a_{ij} are equal to zero. In that case, iterative methods arrive at a solution in a shorter period than direct methods and perform computations only when necessary.

There are three main classes of the iterative methods for linear systems: stationary iterative method, non-stationary iterative method and Krylov subspace methods. Iterative methods that can be expressed in the simple form

$$x^{k+1} = Bx^k + c \tag{2.45}$$

(where neither B nor c depends upon the iteration count k) are called stationary iterative methods, such as Jacobi method, the Gauss-Seidel method, the Successive Over-relaxation (SOR) method and the Symmetric Successive Over-relaxation (SSOR) method.

Non-stationary methods differ from stationary methods in that the computations involve information that changes at each iteration. Typically, constants are computed by taking inner products of residuals or other vectors arising from the iterative method. In this class, there is a special kind of non-stationary method called Krylov subspace method. With respect to the "influence on the development and practice of science and engineering in the 20^{th} century", Krylov space methods are considered as one of the ten most important classes of numerical methods [107]. Large sparse linear systems of equations or large sparse matrix eigenvalue problems appear in most applications of scientific computing. In the past, Krylov space solvers were referred to also by other names such as semi-iterative methods and polynomial acceleration methods. Some of them can also be used as (fixed) preconditioners, in which case they are known as polynomial pre-conditioners. The best known Krylov subspace methods are the Lanczos, Conjugate gradient, GMRES (generalized minimum residual), and MINRES (minimal

residual) methods. Some methods have been applied in solving the inverse problem for MWI, such as CGLS (Conjugate Gradient method for Least Squares).

2.6 Iterative Shrinkage/Thresholding (IST)

IST algorithm was derived by several groups in different frameworks [107–112]. In particular, Figueiredo and Nowak [112] proposed the function $\Psi(\cdot)$ as the log-likelihood function for a restoration problem with Gaussian noise and obtained the algorithm based on an electromagnetic (EM) approach. Combettes and Wajs (see also [109] and [113]) investigate the minimisation of functions given as sums of two convex functions. Characterisation of the solution as the fixed point of a proximity operator leads to an iterative algorithm that coincides with the IST algorithm for the particular objective function [114]. Another approach is discussed by Bredies, Lorenz and Maass in [108], where they interpret the inclusion of a non-differentiable regularisation term as a generalisation of a constraint and regard the IST algorithm as a generalised conditional gradient algorithm.

The IST algorithm is proposed for finding minimisers of (2.43), which is focused on the finite-dimensional case, $X = \mathbb{R}^m, Y = \mathbb{R}^n$, and it denotes the standard Euclidean vector norm as $\|\cdot\|_2$. The IST algorithm has the form

$$x_{t+1} = (1 - \beta)x_t + \beta\Psi_\lambda(x_t + K^T(y - Kx_t)) \tag{2.46}$$

where $\beta > 0$. The original IST algorithm has the form (2.46), with $\beta = 1$ [111, 112, 115]. Schemes with $\beta \neq 1$ can be seen as under ($\beta < 1$) and over ($\beta > 1$) relaxed versions of the original IST algorithm.

Each iteration of the IST algorithm only involves sums, matrix-vector products by K and K^T, and the application of the de-noising operation Ψ_λ. In wavelet-based methods, Ψ_λ is a coefficient- wise non-linearity, thus very computationally efficient. When K represents the convolution with some kernel k, the corresponding product can

be computed efficiently using the fast Fourier transform (FFT) [116]. Convergence of IST, with $\beta = 1$, was first shown in [111]. Later, convergence of a more general version of the algorithm was shown in [110].

2.7 Summary

In this chapter, we have introduced the theory of the FDTD method starting from the Maxwell equations. The explicit update equations based on the 2-D FDTD with CPML are presented. The Debye model is employed to describe the dielectric spectrum of human tissues, and corresponding numerical breast phantoms derived from 3-D MRI datasets from patients are presented as the original data of the simulation experiments. Besides, the distorted Born iterative method is introduced to solve the inverse scattering problem in MWI, by transforming the non-linear problem to the linear problem that then can be solved by a variety of iterative methods. Finally, a traditional IST method is introduced as the background of the TWIST method in the next chapter.

Chapter 3

MICROWAVE BREAST IMAGING BASED ON AN OPTIMISED TWO-STEP ITERATIVE SHRINKAGE/THRESHOLDING METHOD

In this chapter, we propose the application of a two-step iterative shrinkage/thresholding method (TwIST) to improve the resolution in MWI applications. The TwIST algorithm is combined with the DBIM to reconstruct the complex permittivity of 2-D anatomically realistic numerical breast phantoms. This section will also involve discussions on how to optimise the algorithm parameters to improve the quality of reconstructions and the robustness of the algorithm. The results generated demonstrate the ability of this method to produce images with enhanced resolution in 2-D microwave breast imaging.

3.1 Introduction

Microwave tomographic methods for medical imaging estimate the spatial distribution of dielectric properties in a tissue region by solving an EM inverse scattering problem [117, 118]. Various EM inverse scattering methods have been proposed in recent years for this purpose, such as CG techniques [119, 120] and Gauss–Newton (GN) optimisation algorithms [22, 34, 121]. In this chapter, microwave tomography is implemented by applying the DBIM, which approximates the non-linear inverse scattering problem by an underdetermined set of linear equations.

Previous work has applied adaptive thresholding methods to solve this set of linear equations thereby improving reconstructions in DBIM-based microwave breast imaging [122]. This work improves further the solution to the resulting ill-posed linear system at every DBIM iteration based on the use of the TwIST algorithm [116], which uses the two previous iterates to compute the current update of the iterative linear solver. This allows the TwIST method to exhibit much faster convergence and improved robustness relative to the one-step iterative methods.

This chapter mainly demonstrates how to implement microwave breast imaging based on TwIST by optimising the algorithm parameters for this particular application.

3.2 Methodology

3.2.1 Microwave Breast Imaging based on DBIM

As discussed in the previous chapter, DBIM is an inverse scattering algorithm, which is commonly used to estimate the spatial distribution of dielectric properties within a region V [118]. It is based on a non-linear integral equation, which can be described in

its 2-D scalar form as [123],

$$\begin{aligned} E_s(\boldsymbol{r}_n, \boldsymbol{r}_m) &= E(\boldsymbol{r}_n, \boldsymbol{r}_m) - E_b(\boldsymbol{r}_n, \boldsymbol{r}_m) \\ &= \omega^2 \mu \int_V G_b(\boldsymbol{r}_n, \boldsymbol{r}) E(\boldsymbol{r}, \boldsymbol{r}_m)(\epsilon(\boldsymbol{r}) - \epsilon_b(\boldsymbol{r}) d\boldsymbol{r}), \end{aligned} \tag{3.1}$$

where E, E_s, E_b denote respectively total, scattered, and background fields, and $\boldsymbol{r}_n$ and $\boldsymbol{r}_m$ denote the Tx and Rx antenna locations. The total field is measured at each antenna, but is unknown inside V. Inside of the integral, G_b is the Green's function for the background medium. As argued in the previous chapter, the Green's function is estimated by $G_b(\boldsymbol{r}_n, \boldsymbol{r}) = \frac{i}{\omega\mu} E_b(\boldsymbol{r}, \boldsymbol{r}_m)$. The difference between the complex permittivity of the object $\epsilon(\boldsymbol{r})$ and background $\epsilon_b(\boldsymbol{r})$ are defined as the contrast function $O(\boldsymbol{r})$, which is updated at each iteration. Under the Born approximation, this non-linear integral equation is linearised by replacing the unknown total electric field $E(\boldsymbol{r}, \boldsymbol{r}_m)$ with the known background field $E_b(\boldsymbol{r}, \boldsymbol{r}_m)$ [34]. These approximations yield the following integral equation as

$$E_s(\boldsymbol{r}_n, \boldsymbol{r}_m) \approx i\omega \int_V E_b^2(\boldsymbol{r}, \boldsymbol{r}_m) O(\boldsymbol{r}) d\boldsymbol{r}. \tag{3.2}$$

This equation can be discretized for all Tx-Rx pairs, leading to a linear system given by

$$\boldsymbol{A}(\omega)\boldsymbol{o} = \boldsymbol{b}(\omega) \tag{3.3}$$

where

$$\begin{aligned} \boldsymbol{A}(\omega) &= i\omega \boldsymbol{E}_b^2 \\ \boldsymbol{o} &= \epsilon(\boldsymbol{r}) - \epsilon_b(\boldsymbol{r}) \end{aligned} \tag{3.4}$$

In (3.3), $\boldsymbol{A}(\omega)$ is an M-by-K matrix, where M is the number of transmit–receive pairs in the antenna array and K denotes the number of elements in the discretisation in the reconstruction range V. The K-by-1 vector $\boldsymbol{o}$ contains the unknown dielectric properties contrast for the K voxels in V, while $b(\omega)$ is an M-by-1 vector with elements that are

equal to the residual scattered fields $\boldsymbol{E}^{z}_{scat}(\boldsymbol{r}_n|\boldsymbol{r}_m)$. For example, in the 16-antenna system, M is equal to $16 * 15/2 = 120$.

According to the introduction in Section 2.4.2, the updated background profile can be obtained as

$$\boldsymbol{\epsilon}_{bi+1} = \boldsymbol{\epsilon}_{bi} + \boldsymbol{o}_{i+1} \tag{3.5}$$

where $\boldsymbol{o}_{i+1}$ is the solution of the previous iteration by solving (2.38).

3.2.2 Two-Step IST (TwIST)

Consider an inverse problem where the goal is to estimate an unknown original image vector x from an observation vector y, described by the linear equation $\boldsymbol{Ax} = \boldsymbol{y}$. Many approaches to this LIP define a solution $\hat{\boldsymbol{x}}$ as a minimiser of a convex objective function $f : \chi \to \mathbb{R} = [-\infty, +\infty]$, given by

$$f(\boldsymbol{x}) = \frac{1}{2}\|\boldsymbol{y} - A\boldsymbol{x}\|^2 + \lambda\Phi(\boldsymbol{x}) \tag{3.6}$$

where $\Phi(\boldsymbol{x})$ is a regularisation function for the convex optimisation problem and $\lambda \in [0, +\infty]$ is a weighting parameter.

In recent years, iterative algorithms were independently proposed by many authors in different frameworks [116, 124–127]. For example Ref. [116] presents a method of splitting the matrix to structure a two-step iterative equation.

Consider the linear system $Ax = b$, with positive definite $\boldsymbol{A}$; define a so-called splitting of $\boldsymbol{A}$ as $\boldsymbol{A} = \boldsymbol{C} - \boldsymbol{B}$, such that $\boldsymbol{C}$ is positive definite and easy to invert. A stationary two-step iterative method (TwSIM) for solving $\boldsymbol{b}$ is defined as

$$\begin{aligned} \boldsymbol{x}_1 &= \boldsymbol{x}_0 + \beta_0 \boldsymbol{C}^{-1}(\boldsymbol{b} - \boldsymbol{A}\boldsymbol{x}_0) \\ \boldsymbol{x}_{t+1} &= (1-\alpha)\boldsymbol{x}_{t-1} + \alpha\boldsymbol{x}_t + \beta\boldsymbol{C}^{-1}(\boldsymbol{b} - \boldsymbol{A}\boldsymbol{x}_t) \end{aligned} \tag{3.7}$$

for $t \leq 1$, where $\boldsymbol{x}_0$ is the initial vector, and α, β, and β_0 are the parameters of the algorithm.

For a large sparse linear problem, A is always not positive definite. Thus, we can take $\boldsymbol{C} = \boldsymbol{I} + \lambda \boldsymbol{D}_t$ and $\boldsymbol{R} = \boldsymbol{I} - \boldsymbol{K}^T\boldsymbol{K}$ in the splitting $\boldsymbol{A} = \boldsymbol{C} - \boldsymbol{R}$ of the matrix $\boldsymbol{A} = \lambda \boldsymbol{D}_t + \boldsymbol{K}^T\boldsymbol{K}$, the two-step iteration (3.7) for the linear system $\boldsymbol{A}\boldsymbol{x} = \boldsymbol{K}^T\boldsymbol{y}$ becomes

$$\boldsymbol{x}_{t+1} = (1-\alpha)\boldsymbol{x}_{t-1} + (\alpha - \beta)\boldsymbol{x}_t + \beta \boldsymbol{C}^{-1}(\boldsymbol{x}_t + \boldsymbol{K}^T(\boldsymbol{y} - \boldsymbol{K}\boldsymbol{x}_t)) \tag{3.8}$$

Observe the relationship between (2.46) and (3.8): the former can be obtained from the latter by setting $\alpha = 1$ and replacing the multiplication by matrix $\boldsymbol{C}^{-1}$ by the de-noising operator $\boldsymbol{\Psi}_\lambda$. This similarity suggests a TwIST as shown below:

$$\boldsymbol{x}_{t+1} = (1-\alpha)\boldsymbol{x}_{t-1} + (\alpha - \beta)\boldsymbol{x}_t + \beta \Gamma_\lambda(\boldsymbol{x}_t) \tag{3.9}$$

$$\Gamma_\lambda(\boldsymbol{x}) = \Psi_\lambda(\boldsymbol{x} + A^T(\boldsymbol{y} - A\boldsymbol{x})) \tag{3.10}$$

where α and β are the parameters of the TwIST algorithm, and Ψ_λ is the regularisation operation. The designation 'two-step freeze' stems from the fact that the next estimate $\boldsymbol{x}_{t+1}$ depends on both the current solution $\boldsymbol{x}_t$ and the previous solution $\boldsymbol{x}_{t-1}$, rather than only on $\boldsymbol{x}_t$.

It is noted that the one-step IST method is a special case of the TwIST with $\alpha = 1$ and that the Landweber method can be obtained with $\alpha = 1$ and $\beta = 1$ [128]. In our research, the regularisation parameter λ is set to zero in order to discuss the influence of the TwIST parameters independently. Then the update equation is simplified below,

$$\boldsymbol{x}_{t+1} = (1-\alpha)\boldsymbol{x}_{t-1} + \alpha \boldsymbol{x}_t + \beta(A^T(\boldsymbol{y} - A\boldsymbol{x})) \tag{3.11}$$

According to Theorem 3 in [116], (3.11) converges to the solution of $A\boldsymbol{x} = \boldsymbol{y}$, if and only if $0 < \alpha < 2$ and $0 < \beta < 2\alpha/\lambda_m$, where λ_m denotes the largest eigenvalues of the matrix A^TA. The optimal parameters α and β are obtained from the asymptotic

convergence factor

$$\begin{aligned} \alpha &= \rho^2 + 1 \\ \beta &= 2\alpha/(\lambda_1 + \lambda_m) \\ \rho &= (1 - \sqrt{k}/(1 + \sqrt{k})) \end{aligned} \tag{3.12}$$

where λ_1 is the smallest eigenvalue of the matrix $A^T A$ and $k = \lambda_1/\lambda_m$ is its inverse condition number [116].

In MWI, the matrix $A_{m\times n}$ is a severely ill-posed matrix with $m << n$, where m is the number of measurements and n represents the number of unknown dielectric contrast coefficients of the breast model. The matrix $A^T A$ has some eigenvalues very close to zero and others greater than 1, which leads to an unstable iterative process. Therefore, to apply for the TwIST, the matrix is normalised by a suitably chosen smallest eigenvalue ξ, and the optimal parameters become,

$$\begin{aligned} \hat{k} &= \xi/1 \\ \hat{\rho} &= (1 - \sqrt{\hat{k}})/(1 + \sqrt{\hat{k}}) \\ \hat{\alpha} &= \hat{\rho}^2 + 1 \\ \hat{\beta} &= 2\hat{\alpha}/(\xi + 1) \end{aligned} \tag{3.13}$$

Another important aspect of the TwIST algorithm is the so-called tolerance that determines the number of the TwIST iterations at each DBIM iteration. In this chapter, the stopping criterion is based on the relative variation of the objective function (3.6) which is described as

$$V_t = \|f_t - f_{t-1}\|/f_{t-1}, \tag{3.14}$$

where V_t is the current relative variation, and f_t and f_{t-1} are respectively the current and previous value of the objective function. When V_t becomes smaller than a value denoted as the tolerance, the TwIST iteration algorithm stops and returns the result to the DBIM iteration.

3.2.3 Frequency Hopping Approach

MWI involving large inhomogeneous bodies using the inverse scattering technique is highly non-linear. This is because the scattered fields are non-linearly related to the inhomogeneity. The non-linearity is a consequence of multiple scattering [103]. Therefore, as the body becomes large compared to the wavelength or when the contrasts of the inhomogeneity become large, the non-linear effect, or the multiple scattering effect, becomes more pronounced. However, this effect is less pronounced at lower frequencies [105, 129]. Therefore, an inverse problem involving higher contrasts can be solved at lower frequencies. When the frequency becomes higher, the inverse problem increases in non-linearity. An optimisation approach is the robust way of solving the inverse scattering problem. However, due to the non-linearity, the use of single-frequency data at a high frequency often results in the inverse algorithm being trapped in local minima due to the highly non-linear nature of the problem [123].

W.C. Chew and J.H. Lin have proposed the frequency hopping approach to process multiple-frequency microwave measurement data. By using the image reconstructed from low frequency data as the initial guess to the higher frequency problem, the authors found that the non-linear effect can be mitigated. By slowly hopping from lower frequencies to higher frequencies, reconstruction of objects that are as large as 10 wavelengths in diameter with high fidelity can be performed. The image reconstructed is much better than using the high-frequency data directly. Such a MWI algorithm needs no *a priori* information about the inhomogeneous body [123].

3.2.4 Hard Constraints

In mathematical optimisation, constraint optimisation is the process of optimising an objective function with respect to some variables in the presence of constraints on those variables. The objective function is either a cost function or energy function which is to be minimised, or a reward function or utility function which is to be maximised.

Table 3.1: Hard boundary setting of Debye parameters applied for the updated background $\epsilon_{i+1}(r)$ in each DBIM iteration.

Debye parameters	Lower bound	Upper bound
ϵ_∞	2.28	23.2
$\Delta\epsilon$	1.3	33.6
$\sigma_s(S/m)$	0.0023	0.801

Constraints can be either hard constraints which set conditions for the variables that are required to be satisfied, or soft constraints which have some variable values that are penalised in the objective function if, and based on the extent that, the conditions on the variables are not satisfied.

In our system, we apply the hard constraint technique to restrict the updated dielectric properties $\epsilon_{i+1}(r)$ in a reasonable range, which is obtained from (2.39). The choice of boundary conditions is based on the fitted Debye parameters of the media modelled by the UWCEM as shown in Table 2.1 and Table 3.1. For example, the value of $\epsilon_{i+1}(r)$ in certain voxels will be replaced as the value of the upper bound when they are beyond the upper bound. Note that the hard constraint only is used in the reconstruction range, as the immersion property is *a priori* information in the imaging system.

3.3 Performance Analysis of the DBIM-TwIST Algorithm

This section considers a 2-D microwave breast imaging simulation scenario which has been used in previous work to evaluate imaging performance with the frequency hopping approach [120]. All simulation cases are based on the FDTD method with a CPML boundary condition. The parameters ϵ_∞, ϵ_s, and σ_s of the Debye model are estimated for the complex relative permittivity,

$$\epsilon_r(\omega) = \epsilon_\infty + \frac{\epsilon_s - \epsilon_\infty}{1 + j\omega\tau} - j\frac{\sigma_s}{\omega\epsilon_0}, \tag{3.15}$$

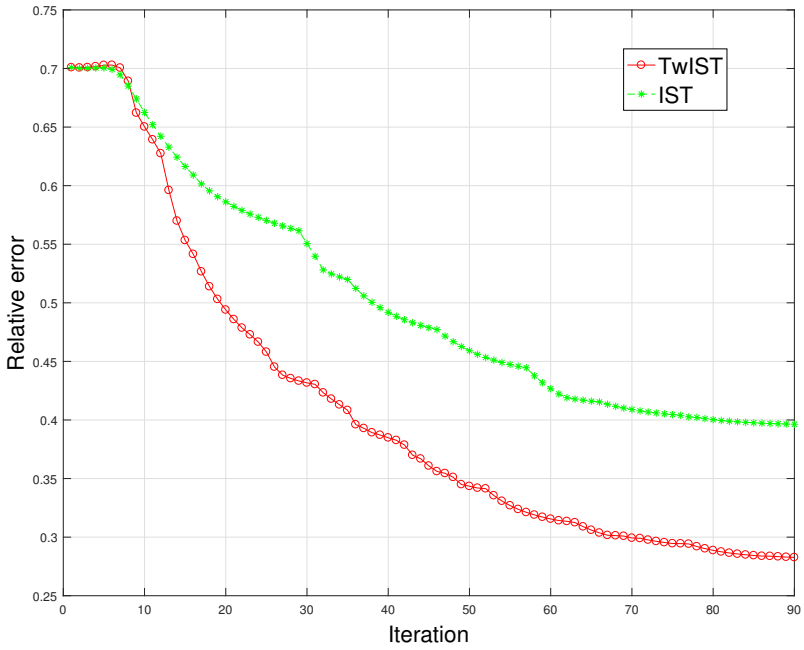

Figure 3.1: Difference from the reconstruction by the IST and the TwIST method, in the range from 1 GHz to 3.5 GHz (15 iterations at each frequency).

where τ is assumed constant for all tissues (with a fixed value of 17.125 ps). The original true image of the 2-D breast is sampled with a cubic cell of a 2 mm side and obtained from UWCEM numerical breast phantom 062204 (see Fig. 2.5 in the previous chapter) [130]. Sixteen antennas surround the breast and correspond to point sources with a wideband pulse for 2-D simulations [120, 122]. Six sampling frequencies are selected at 1.0, 1.5, 2.0, 2.5, 3.0, and 3.5 GHz. Moreover, the background medium is assumed lossless with $\epsilon_r = 2.6$, and the outer outline of the breast model is assumed to be known precisely for reconstruction. To compare the image reconstruction quality, the 'relative error' is defined (used as the y-axis in subsequent figures) as,

$$\frac{\|\epsilon_{\infty original} - \epsilon_{\infty reconstructed}\|^2}{\|\epsilon_{\infty orginal}\|^2} \tag{3.16}$$

Finally, some representative reconstruction images for the optimized parameters are shown at the end of the next section.

3.3.1 Comparison of the IST and TwIST Algorithms

The IST algorithm is a representative of the one-step iterative methods, which has been introduced in Section 2.6. In Fig. 3.1, the reconstruction results illustrating the convergence speed and accuracy of the TwIST vs the IST algorithm are presented. It is evident that the TwIST performs better than the IST. It is also important to note that the difference between the initial guess and true image can influence the convergence of the TwIST and the IST method. If the initial guess is far from the average dielectric properties of the true image, the TwIST is more likely to become unstable compared with the IST algorithm. Finally, the corresponding reconstructed images are shown in Section 3.3.4.

3.3.2 Impact of Estimated ξ

The parameter ξ of the TwIST algorithm is an estimate of the minimal eigenvalue of $A^T A$. Generally, $\xi = 10^{-4}$ denotes severely ill-conditioned problems, and $\xi = 10^{-2}$ denotes mildly ill-conditioned problems. In this chapter, the impact of different values of ξ on the reconstruction quality has been examined. Fig. 3.2 suggests that there is only little effect in the range 10^{-2} to 10^{-6}. If ξ is set smaller than 10^{-6}, the algorithm becomes unstable. Therefore, it can be concluded that the TwIST algorithm is very robust for this range of value ξ, and ξ to 10^{-4} is set for all imaging simulations.

3.3.3 Optimization of the TwIST Parameters

The tolerance value determines the stopping criterion for the TwIST iteration (see (3.14)). This will affect the estimated solution at each DBIM iteration, and therefore plays a key role for the overall convergence of the DBIM. Fig. 3.3 demonstrates the results for different fixed tolerance values by using the frequency hopping method. It is evident that a smaller tolerance value drops the error faster after the 20_{th} iteration, but a very small value (10^{-4}) causes the DBIM to diverge early due to amplification of the initial

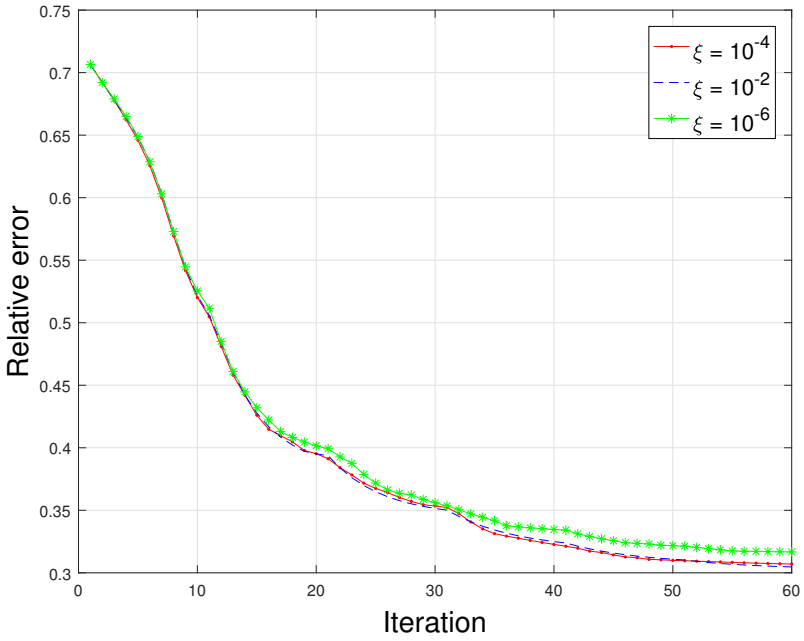

Figure 3.2: Impact of the estimated ξ with $Tol = 10^{-2}$ and known skin in 90 iterations by TwIST method and frequency hopping method.

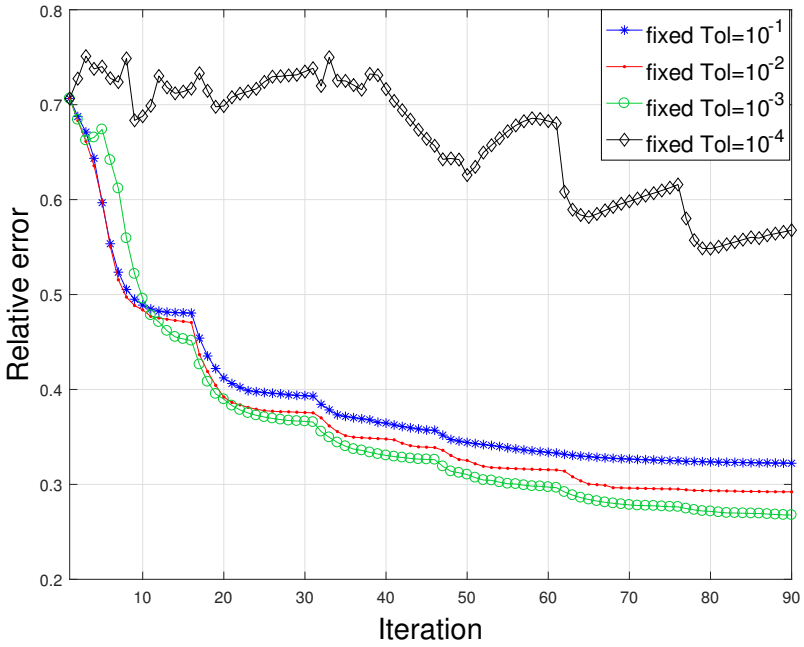

Figure 3.3: Comparison of the results in different tolerance values with known skin in 90 iterations by TwIST method and frequency hopping method.

error. This graph shows that the values in the order on 10^{-2} and 10^{-3} are optimal, but also suggests that an adaptive process for determining its value is advantageous.

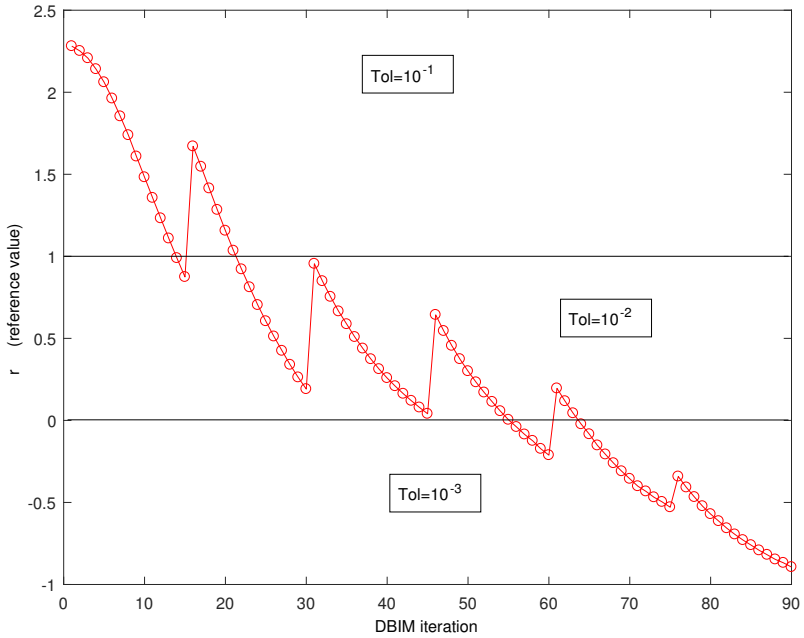

Figure 3.4: Adaptive method for setting the tolerance value depending on the reference value, r, in three ranges including $r < 0$, $0 \leq r < 1$, and $r \geq 1$.

To this end, we have designed an adaptive tolerance method for the TwIST-DBIM implementation. Firstly, it is assumed that at the n-th DBIM iteration ($n < 90$), there are m TwIST iterations where we can obtain m outputs of the objective function ($f_{(n-1,1)} \ldots f_{(n-1,m)}$) corresponding to the previous DBIM iteration. Then we define a reference value r_n, by $r_n = log_{10}(max\{f_{(n-1,1)}, f_{(n-1,2)} \ldots f_{(n-1,m)}\})$, where max denote the maximum in the m objective functions. Based on the reference value r, we set the tolerance value as,

$$Tol_n = \begin{cases} 10^{-1} & r_n > 1 \\ 10^{-2} & 0 < r_n \leq 1 \\ 10^{-3} & r_n < 0 \end{cases} \tag{3.17}$$

The process is illustrated in Fig. 3.4. At the first iteration, Tol_1 is set to 10^{-1}.

As shown in Fig. 3.5, the adaptive method can reduce the iteration error at the first frequency (from the 1st to 10th iteration) and can increase the accuracy of reconstruction in high frequencies (from the 70th to 90th iteration). Importantly, these improvements

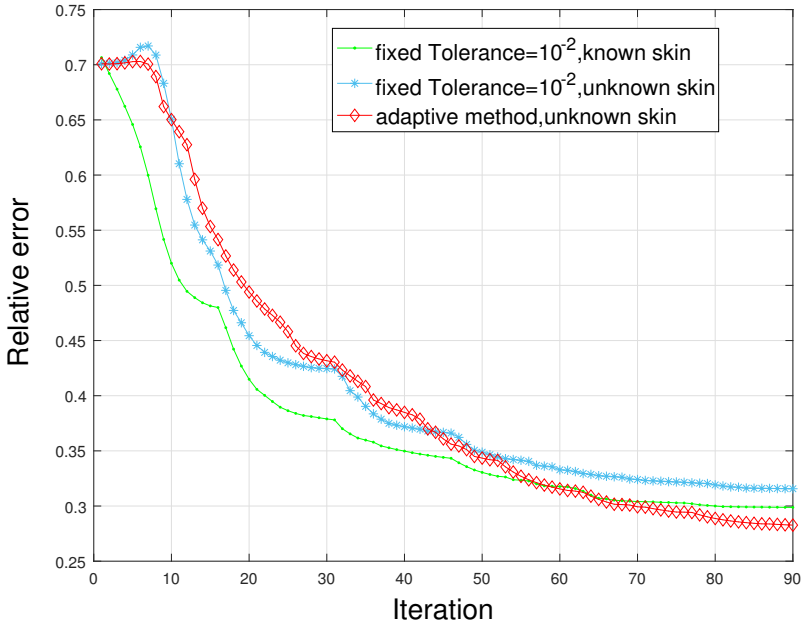

Figure 3.5: Comparison between the adaptive tolerance method and the fixed tolerance method for the case of unknown skin layer thickness and properties.

can be obtained without any prior knowledge of the skin layer thickness and dielectric properties. On the contrary, the TwIST becomes unstable when the tolerance is fixed to 10^{-3} with unknown prior knowledge of the skin. This is because the adaptive tolerance method improves smoothness of the curve in the first 10 iterations by setting a large tolerance value. This means that the estimated error is reduced at these early iterations where the DBIM initial guess is far from the solution. Compared with the three curves shown in Fig. 3.5, it can be concluded that the adaptive method improves robustness and reconstructs more accurate and fine details in high frequencies.

3.3.4 Reconstructed Images

Out optimization analysis is concluded by showing reconstructed images for the Debye parameters ϵ_∞, $\Delta\epsilon$, and σ_s in Fig. 3.6, which are obtained by the IST, the TwIST with fixed tolerance 10^{-2}, and the TwIST method with the adaptive tolerance method. By comparison with the original image, it is evident that Fig. 3.6 (g–i) present the best estimate especially in terms of the breast details. It is also evident that the TwIST method

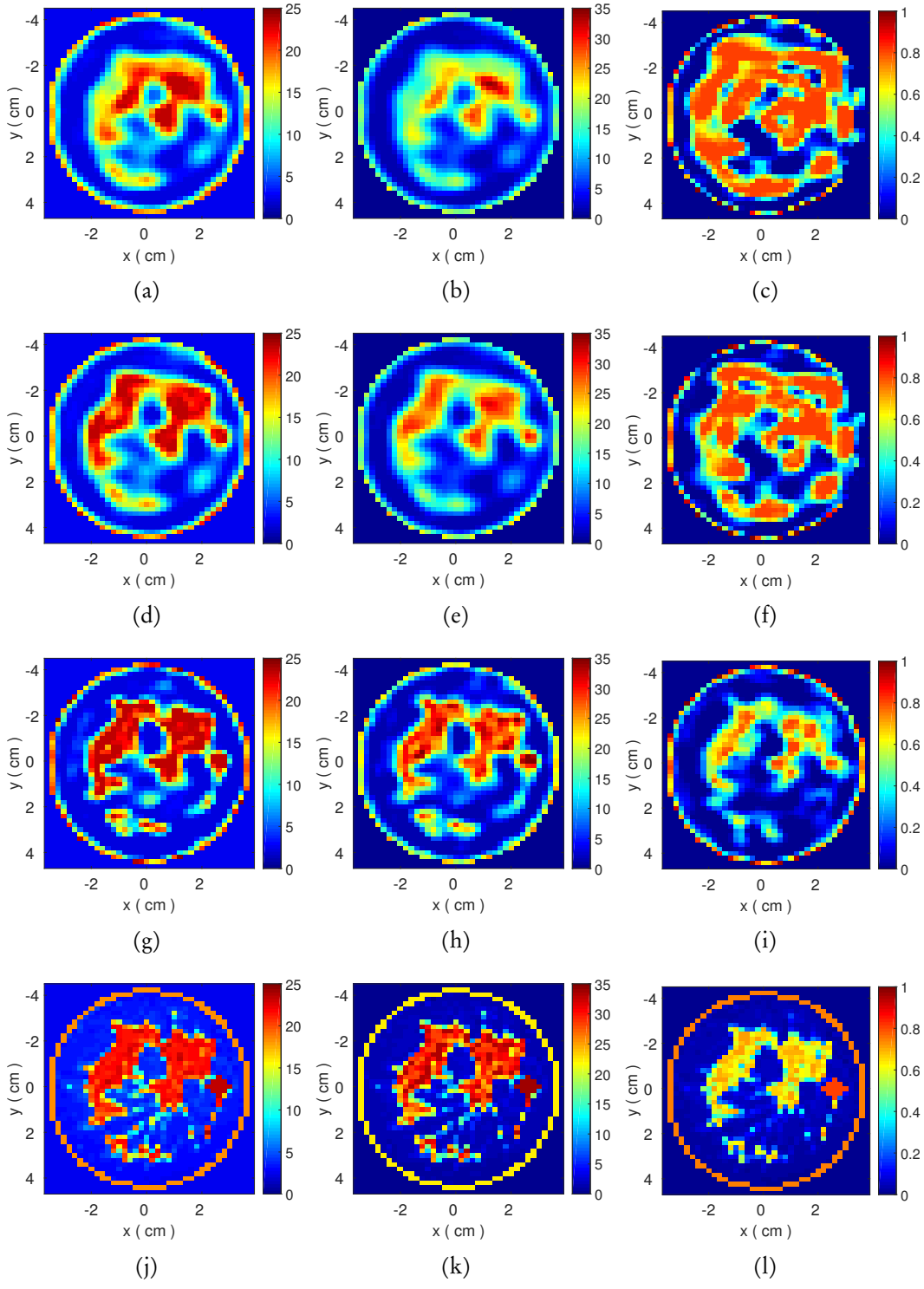

Figure 3.6: Reconstructions of the ϵ_∞ (the left column), $\Delta\epsilon$ (the middle column), and σ_s (the right column) profiles by IST method, original TwIST method, and adaptive TwIST method using the frequency-hopping approach. (a–c) Reconstruction by the IST method; (d–f) Reconstruction by the TwIST method with fixed tolerance as 10^{-2}; (g–i) Reconstruction by the TwIST method with the adaptive tolerance; (j-l) Reference ϵ_∞, $\Delta\epsilon$, and σ_s profiles of original breast phantom.

outer-performs the IST in reconstructing the breast phantom. In particular, compared with (d–f), the adaptive TwIST method in (g–i) produces the most accurate details. Note that (i) shows a clear outline of breast tissues inside, which prove the high stability of this study's adaptive method.

3.4 Conclusion

An improved DBIM algorithm for microwave breast imaging has been implemented based on the TwIST method, which is a novel way for solving the linear problem at each DBIM iteration. The initial simulations of this study demonstrated the advantages and potential of the TwIST compared with one-step iterative such as the IST. The chapter focuses on the optimal choice of the TwIST parameters to improve the resolution in microwave breast imaging applications. The final reconstructed breast images have shown that the two-step iterative method can produce high-quality images in 2-D breast reconstructions.

Chapter 4

IMPLEMENTATION OF MULTIPLE-FREQUENCY APPROACH FOR MICROWAVE BREAST IMAGING

4.1 Introduction

This chapter presents new strategies which improve further the performance of the DBIM-TwIST algorithm for microwave breast imaging. Firstly, we improve the performance of the DBIM-TwIST further by refining our previous work on multiple-frequency reconstructions using a single-pole Debye model [131, 132]. Reconstructing the single-pole Debye parameters allows multiple frequency data to be used for the inversion at each DBIM iteration [118, 131, 133]. Multiple-frequency approaches can combine the stabilizing effects of lower frequencies with enhanced resolution of higher frequencies, thereby overcoming stability and resolution limitations of single-frequency algorithms which tend to be very dependent upon the chosen frequency [103].

Moreover, our analysis provides insight on how to utilize multiple-frequency information to enhance the accuracy of reconstruction and robustness of the DBIM-TwIST algorithm. Our adopted hybrid frequency approach provides better stability and reconstruction accuracy at lower computational cost relative to frequency-hopping techniques [120]. Furthermore, to tackle the increase of computational cost for FDTD implementation in high resolution, we proposed an optimisation of FDTD simulation speed by modifying the excitation from the point source and the FDTD time step.

Finally, the BDIM-TwIST out-performs two well-known iterative methods employed for reconstruction. Our research presents the strong robustness and stability of the multiple-frequency BDIM-TwIST algorithm.

4.2 Methodology

4.2.1 Multiple-Frequency Formulation of DBIM-TwIST Algorithm

The DBIM is an iterative inverse scattering algorithm which is commonly used to estimate the spatial distribution of dielectric properties within a region V [134]. Under the Born approximation, a linear integral equation at each iteration can be discretized for all Tx-Rx pairs, leading to a linear system that can be solved by various methods including the TwIST method, as presented in the previous chapter [132]. The chapter presented a methodology to increase the robustness of the DBIM–TwIST algorithm, as well as ways to optimise its parameters for a particular application such as microwave breast imaging. This robustness is an important advantage of the TwIST method relative to other iterative solvers such as CGLS and LSQR, as suggested by the comparison results in Section 4.5.3.

$$\begin{bmatrix} \Re\{A(\omega_1)\} & \frac{\Re\{A(\omega_1)\}+\omega_1\tau\Im\{A(\omega_1)\}}{1+(\omega_1\tau)^2} & \omega^*\omega_1^{-1}\Im\{A(\omega_1)\} \\ \Im\{A(\omega_1)\} & \frac{\Im\{A(\omega_1)\}-\omega_1\tau\Re\{A(\omega_1)\}}{1+(\omega_1\tau)^2} & -\omega^*\omega_1^{-1}\Re\{A(\omega_1)\} \\ \Re\{A(\omega_2)\} & \frac{\Re\{A(\omega_2)\}+\omega_2\tau\Im\{A(\omega_2)\}}{1+(\omega_2\tau)^2} & \omega^*\omega_2^{-1}\Im\{A(\omega_2)\} \\ \Im\{A(\omega_2)\} & \frac{\Im\{A(\omega_2)\}-\omega_2\tau\Re\{A(\omega_2)\}}{1+(\omega_2\tau)^2} & -\omega^*\omega_2^{-1}\Re\{A(\omega_2)\} \\ \vdots & \vdots & \vdots \\ \Re\{A(\omega_f)\} & \frac{\Re\{A(\omega_f)\}+\omega_f\tau\Im\{A(\omega_f)\}}{1+(\omega_f\tau)^2} & \omega^*\omega_f^{-1}\Im\{A(\omega_f)\} \\ \Im\{A(\omega_f)\} & \frac{\Im\{A(\omega_f)\}-\omega_f\tau\Re\{A(\omega_f)\}}{1+(\omega_f\tau)^2} & -\omega^*\omega_f^{-1}\Re\{A(\omega_f)\} \end{bmatrix} \begin{bmatrix} \boldsymbol{o}_\infty \\ \boldsymbol{o}_\Delta \\ \frac{\boldsymbol{o}_\sigma}{\epsilon_0\omega^*} \end{bmatrix} = \begin{bmatrix} \Re\{A(\omega_1)\} \\ \Im\{A(\omega_1)\} \\ \Re\{A(\omega_2)\} \\ \Im\{A(\omega_2)\} \\ \vdots \\ \Re\{A(\omega_f)\} \\ \Im\{A(\omega_f)\} \end{bmatrix} \tag{4.1}$$

The multiple-frequency approach essentially involves solving (2.37) at multiple frequencies simultaneously. The systems of equations at different frequencies are coupled via the Debye model in (4.2), such that the contrast function represents the contrast of the unknown parameters of the Debye model. Because the model parameters are real values, the first step is to separate the real (R) and imaginary (I) components of each set of equations. Then the real and imaginary parts of the complex permittivity can be expressed in terms of the Debye parameters. Note that there is a fourth parameter of relaxation time τ in the one-order Debye model (4.2). However, it is impossible to separate the τ into a matrix structure. Thus, it has to be assumed that τ is known as constant and invariant with position. This is also a reasonable assumption since τ does not vary extensively across the different biological tissues of the breast [118].

The structure of matrix A is shown in (4.1), where $\boldsymbol{A}_f$ is the extended term of the $\boldsymbol{A}$ in (3.3) for multiple frequencies. The vector of unknowns on the left-hand side of (4.1) is composed of three vectors of equal length: $\boldsymbol{o}_\infty$, $\boldsymbol{o}_\Delta$ and $\boldsymbol{o}_\sigma$. These sub-vectors contain the contrast values for the respective Debye parameters ϵ_∞, $\Delta\epsilon$ and σ_s, for each of K voxels. Note that the ω^* is a scaling factor to provide solution stability. This parameter can

adjust the weight of σ_s when the linear equation is solved. The effect of the ω^* will be discussed in the next section. The complete MATLAB codes are shown in Appendix A.2.

4.2.2 Testbeds for 2-D Microwave Breast Imaging

A 2-D microwave breast imaging simulation scenario that has been used in previous work is considered for evaluation of imaging performance with different inversion approaches [131, 135]. Simulation data is produced by the FDTD method with a CPML boundary condition. The tests include all four types of numerical breast phantoms taken from the UWCEM repository [136]. In particular, 2-D axial slices representative of the phantoms classified as 'mostly fatty' (ID:071904), 'scattered fibroglandular' (ID:010204), 'heterogeneously dense' (ID:062204) and 'very dense' (ID:012304) have been considered. The single-pole Debye model is employed to describe the frequency-dependence for all breast tissues in the computation model,

$$\epsilon_r(\omega) = \epsilon_\infty + \frac{\epsilon_s - \epsilon_\infty}{1 + j\omega\tau} - j\frac{\sigma_s}{\omega\epsilon_0} \tag{4.2}$$

where τ is assumed constant for all tissues (with a value of 17.125 ps). As in previous work [118, 131, 132], a lossless background medium is assumed with $\epsilon_r = 2.6$ in the simulations. However, the impact of losses is examined for some realistic background coupling media in Section 5.4. Our setup considers sixteen antennas surrounding the 2-D breast phantom, representing point sources excited with a wideband Gaussian pulse in a TM configuration (i.e. the electric field is perpendicular to the breast phantom). Six sampling frequencies are selected at 1.0, 1.5, 2.0, 2.5, 3.0 and 3.5 GHz.

It is noted that the choice of the number of antennas is based on the analysis in [137]. In the 2-D scalar case, the essential number of the antennas is defined as,

$$M = 2\beta\alpha \tag{4.3}$$

where α is the radius of the reconstruction domain and β is the wave number. Considering our first operating frequency of 1 GHz, M is approximately equal to 15.

The shape of the breast model is the only prior information assumed known for the reconstruction, while the relative dielectric permittivity of the skin and its thickness are unknown.

To compare image reconstruction quality, a relative reconstruction error has been defined in (3.16) where ϵ_∞ is chosen as the representative of reconstructed Debye parameter, but similar metrics can be calculated for any of the parameters of the Debye (or an Ohmic) model.

As the true ϵ_∞ cannot be known in a realistic application, and then a 'Residual' error must also be defined as,

$$Residual = \|M_t^E - M_t^S\| \tag{4.4}$$

where M_t^E and M_t^S denote complex vectors of the 'experimental' and 'model' data at the t_{th} iteration respectively, recorded at the antenna locations. The 'Residual' difference can be computed at each DBIM iteration, and can be used as a stopping criterion for the DBIM iterative algorithm.

4.2.3 Conjugate Gradient Algorithms as Alternative Methods to TwIST

The CG method is a widely used iterative algorithm for the numerical solution of large sparse systems of linear equations, whose matrix is symmetric and positive-definite. An overview of applications of CG, and generalisations to indefinite or non-symmetric matrices, can be found, for example, in [138].

The CG method, originally proposed by Hestenes and Stiefel [139], is a well-known iterative method for solving sparse systems of equations $Ax = b$ where the matrix A is positive defined [138, 140–142]. The main problem with methods like the CGLS, which involves the normal equations, is that the condition number of the matrix $A^T A$ usually

is the square of the condition number of A. Therefore, for ill-conditioned problems the algorithm convergence can be slow. However, if the condition number of A is not particularly high, then CGLS can be reasonably expected to converge more quickly.

LSQR is a variant of the conjugate gradient method which can be used for solving non-symmetric linear equations $Ax = b$ and least squares problems $min_x \|b - Ax\|_2$. If A has a full column rank (linearly independent columns), $A^T A$is positive-definite and the conjugate gradient algorithm can be applied to the normal equations $A^T Ax = A^T b$. The resulting algorithm can be implemented in several ways. In this thesis, the algorithm LSQR has been used, which is mathematically equivalent to CG on the normal equations but has favourable properties in floating-point arithmetic [143].

Conjugate Gradient Least-Squares Algorithm

The CGLS algorithm solves the following unconstrained optimization problem:

$$\min_b \|(A^T A + \lambda_{CGLS} I)x - A^T b\|_2 \tag{4.5}$$

where λ_{CGLS} is a regularisation term. As λ_{CGLS} increases, $\|x\|_2$ decreases and the residual error $\|r\|_2 = \|b - Ax\|_2$ increases. If matrix A is $m \times n$, the CGLS requires only $2M + 3N$ complex multiplications in every iteration. When solving (4.5), the number of iterations may be restricted or a threshold ϵ may be specified such that CGLS halts when $\|r\|_2 < \epsilon$. CGLS may also incorporate preconditioning matrices, weighted norms and initial conditions. For the MWI problem, it is hard to obtain *a priori* information about the residual ϵ or related weighted norm, so that an optimal iteration step k cannot be found based on a certain stopping rule. As the CGLS converges monotonically in the first several iterations, one simple solution is that an L-curve technique can be applied to locate an optimal iteration number.

When λ_{CGLS} is 0, CGLS is identical to Hestenes and Stiefel's iterative CG method for least-squares problems [139]. In this chapter, the unconstrained linear problem without

regularisation term is discussed. The next chapter will focus on the regularisation method for de-noising and stabilising the convergence of iterative process.

Least-Squares QR Algorithm

The LSQR algorithm is designed as an implementation of the Tikhonov regularisation and solves large linear least-squares problems in a numerically attractive manner [143, 144]. Its name originates from its use of the QR decomposition [145, 146]. The algorithm has one regularisation parameter, λ_{LSQR}, and solves the following:

$$\min_{b}(\|b - Ax\|_2^2 + \lambda_{LSQR}^2\|b\|_2^2). \tag{4.6}$$

As λ_{LSQR} increases, more weight is placed on the energy of b than on the residual error, causing $\|b\|_2$ to decrease and $\|d - Ab\|_2$ to increase. LSQR also avoids the use of a singular value decomposition (SVD) and it requires $3M + 5N$ complex multiplications every iteration. LSQR, like CGLS, generates b_i such that $\|r_i\|_2$ decreases monotonically, but LSQR performs better in practice [143, 147] because of its unique restructuring of the input system (via the Lanczos process [148] and Golub-Kahan bidiagonalization [149]) prior to solving it. Many studies conducted by Paige and Saunders [149] and Bjorck and Elfving [147] indicate that LSQR can find the best solutions with lower residual error than CGLS when A is ill-conditioned, and of similar fidelity when A is well-conditioned.

In addition to the above, the stopping rules of the LSQR are designed to reflect the data's accuracy. Relative to CGLS's stopping rule based on the iteration number, LSQR ensures that the algorithm always shuts down faster and the estimate of its corresponding b is equally acceptable. This advantage becomes more pronounced as A has a lower condition number [143].

Note that while LSQR indeed requires $N + 2M$ more complex multiplications than CGLS in every iteration, this is mitigated by the fact that LSQR often requires fewer iterations to attain a similar-fidelity solution.

L-Curve Technique

The L-curve is a log-log plot of the norm of a regularised solution versus the norm of the corresponding residual norm. It is a convenient tool for displaying the trade-off between the regularised solution and its fit to the given data, as the regularisation parameter varies. The L-curve thus gives insight into the regularising properties of the underlying regularisation method, and it is an aid in choosing an appropriate regularisation parameter for the given data [150].

Given the discrete linear least-squares problem $\|Ax - b\|_2$, the classical regularisation method developed independently by Phillips and Tikhonov. In its most general form, the minimisation problem is described as,

$$x_\lambda = \arg\min\{\|Ax - b\|_2^2 + \lambda^2 \|L(x - x_0)\|_2^2\}, \tag{4.7}$$

where λ is a real regularisation parameter that must be chosen by the user. Here, the 'size' of the regularised solution is measured by the norm $\|L(x - x_0)\|_2^2$, while the fit is measured by the Euclidean norm $\|Ax - b\|_2$ of the residual. The vector x_0 is *a priori* estimate of x which can be set to zero when no *a priori* information is available. The problem is in standard form if $L = I$, the identity matrix [150].

Having realised the important roles played by the norms of the solution and the residual, it is quite natural to plot these two quantities versus each other, i.e. as a curve

$$(\|Ax_\lambda - b\|_2, \|L(x_\lambda - x_0)\|_2) \tag{4.8}$$

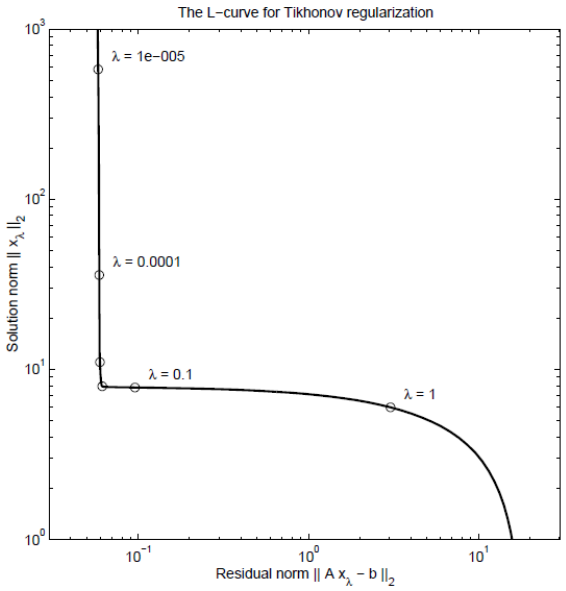

Figure 4.1: An example of L-curve plot

parametrised by the regularisation parameter. This is an example of an L-curve plot in Fig. 4.1. Note that if too much regularisation, or damping, is imposed on the solution, then it will not fit the given data b properly and the residual $\|Ax_\lambda - b\|_2$ will be too large. On the other hand, if too little regularisation is imposed then the fit will be good but the solution will be dominated by the contributions from the data errors, and hence $\|L(x_\lambda - x_0)\|_2$ will be too large. Hence, the L-curve is really a trade-off curve between two quantities that should both be controlled. Such trade-off curves are common in the solving of linear problems, especially the large sparse linear problems.

4.3 FDTD Implementation in Multiple Resolutions

The work carried out in this study investigates imaging performance for different voxel sizes, in order to assess the DBIM–TwIST algorithm's resolution limitations. The resolution of the original breast models is 0.5 mm, it therefore follows that reconstruction of the images in four different grid resolutions, i.e. 2 mm, 1.5 mm, 1 mm and 0.5 mm, is proposed. It can be noted that the maximum resolution must be smaller than the thickness of the skin. Otherwise, the lower resolution may cause down-sampling error

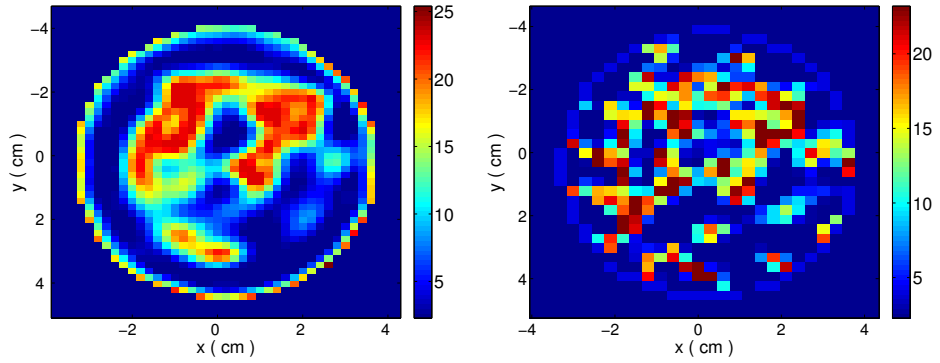

Figure 4.2: Comparison of image reconstructions in different resolutions based on the same fine breast model in 0.5 mm. (a) Reconstruction in 2 mm from 0.5 mm; (b) Reconstruction in 3 mm from 0.5 mm.

in the forward FDTD process and cause artificial error of estimating the skin layer. Consequently, 2 mm is the maximum for the multi-resolution implementation based on the original breast phantoms. Fig. 4.2 indicates the comparison with the reconstructed images in 2 mm and 3 mm. The resolution lower than the thickness of the skin layer cannot be applied for the reconstruction algorithm.

The FDTD method provides flexibility of electromagnetic simulation in different grids and corresponding sampling frequencies. Naturally, the choice of the grid resolution affects the numerical data mismatch error of the FDTD forward solver. In particular, the FDTD simulation data sampling frequency depends on the inverse of the FDTD time-step Δt which is fixed relative to the spatial increment $\Delta x = \Delta y$ according to Courrant's criterion to avoid numerical instability, e.g.,

$$\Delta t = \Delta x/(2 \cdot c) \tag{4.9}$$

where c denotes the speed of light in a vacuum. A soft source excitation is applied, which commonly uses a current source as a drive to produce a required field, such as

$$\boldsymbol{E}_{n+1} = \boldsymbol{E}_n + source(n) \tag{4.10}$$

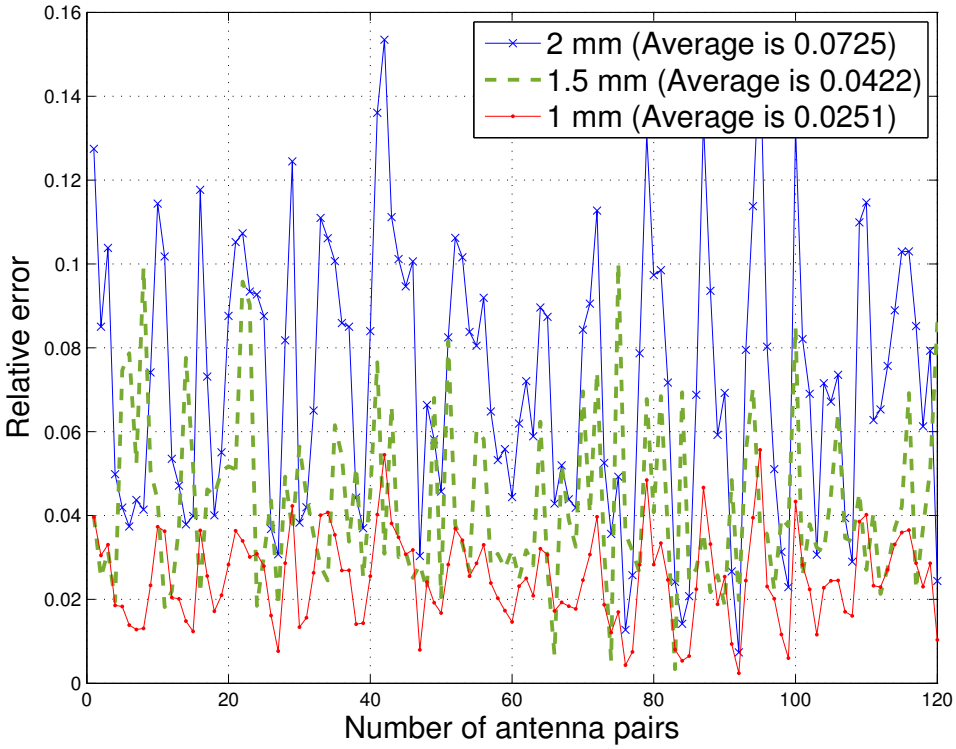

Figure 4.3: Errors of FDTD-calculated signals at the receiver points for multiple grid resolutions against the 0.5 mm resolution of the original phantom.

where $source(n)$ is a discrete series of the voltage source. This soft source causes successive accumulations of energy for different time-step Δt.

To tackle the problem, the relationship between Δx and Δt must be amended and the amplitude of simulated source must be modified to compensate for this error as it is moved from the 0.5 mm grid to its multiple increments 1.0 mm, 1.5 mm, and 2.0 mm. Thus, the parameter mul is defined as the ratio of the multiple resolution to the 'original' resolution grid of 0.5 mm, as shown below,

$$\begin{aligned} mul &= r_c/0.5mm \\ \Delta t &= \Delta x/(2 \cdot c)/mul \\ source_m &= source_o/mul^2 \end{aligned} \tag{4.11}$$

where r_c denotes the targeted resolution, and $source_o$ and $source_m$ are the original excitation signal and the modified source respectively.

Fig. 4.3 plots the relative errors of received signals from 120 antenna pairs (for the 16 antenna system) in 2.0 mm, 1.5 mm and 1.0 mm grid resolutions against the received signal in 0.5 mm. The average of relative errors is 0.0725, 0.0422 and 0.0251 respectively. It is evident that the targeted resolution closer to the fine original model in 0.5 mm results in the least relative error. In all cases, our compensation method results in a data mismatch under 8% relative to the original numerical phantom. This data mismatch due to the forward solver's numerical discretisation is negligible relative to the model mismatch between the true numerical phantom and our initial guess of a homogeneous breast interior with unknown skin properties.

4.4 Optimisation of FDTD Simulation Speed in Various Resolutions

In our breast imaging algorithm, the FDTD computation takes over 90% of the whole computing time. In Section 4.3, an overview of how to obtain equivalent simulation performance in different resolutions has been discussed. However, the high resolution causes an exponential increase of computational cost, in terms of grid size and iteration number. Thus, in this section, two optimisations strategies are proposed to reduce the unnecessary computation cost by adaptively reducing FDTD time step and modifying the excitation function applied in the soft source.

The Gaussian modulated sinusoidal pulse is applied as the excitation of point source, shown as

$$E(t) = e^{-(\frac{t-t_0}{t_w})^2} sin(\omega t) \tag{4.12}$$

where t is the present time, t_0 is the time at which the pulse reaches its maximum value as the delay parameter of the excitation. ω is the angular central frequency of the wide-band

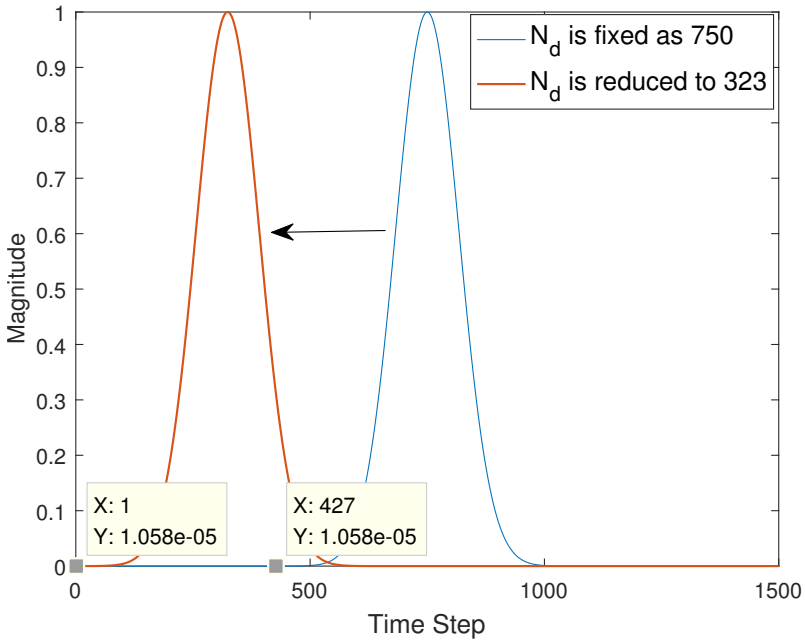

Figure 4.4: Theory of optimizing delay parameter

Gaussian pulse. T_w denotes the Gaussian pulse width, which is defined as

$$T_w = 4/(\pi \cdot (f_{upper} - f_{lower})) \tag{4.13}$$

where f_{upper} and f_{lower} denote the maximum and minimum of the frequency band. The discrete form of this Gaussian pulse is

$$E(n\Delta t) = e^{-(\frac{(n-n_d)\Delta t}{T_w})^2} sin(\omega \cdot n\Delta t) \tag{4.14}$$

where n is the number of time intervals between the turn-on time $t = 0$ and the present time t, and n_d is the number of time intervals between the leading edge and the peak of the Gaussian. The goal now is to determine the length of n and the delay parameter of n_d.

4.4.1 Modified Delay Parameter of Gaussian Modelled Sine Pulse

Generally, the choice of the delay parameter is a constant. However, for a multiple resolution system, this set has to consider a numerical limitation of high grid FDTD, which leads to waste of the computational resource in the low-resolution case. Thus, an adaptive method to obtain the n_d based on envelope of the Gaussian pulse is proposed and that is the first part of (4.14), shown as

$$E^*(n\Delta t) = e^{-(\frac{(n-n_d)\Delta t}{T_w})^2} \tag{4.15}$$

Then another parameter γ can be defined as the left limit of the $E^*(n\Delta t)$. For example, when γ is set to 10^{-5}, a unique point n_d^* can be found on the left of the pulse peak of the function (4.15). Fig. 4.4 indicates a left shift from a fixed value of n_d to a reduced value, which contributes to reducing the waiting time before the radiation from the antenna. The optimal mathematical solution is shown as,

$$n_d^* = \lfloor T_w/\Delta t\sqrt{-\log\gamma}\rfloor \tag{4.16}$$

where $\lfloor\rfloor$ denotes the floor function, and γ always to be set between 10^{-2} and $-\infty$.

4.4.2 An Optimisation of FDTD time step

Based on the optimal delay parameter above, an optimal FDTD time step is proposed by estimating the necessary number of the time step for any model size. Here, we define the optimal time step as,

$$n_{opt} = 2 \cdot n_d^* + \max\{dimX, dimY\} \cdot \sqrt{2} \cdot 5 \tag{4.17}$$

where $2 \cdot n_d^*$ contains the whole length of the envelope of the Gaussian pulse. Then a setting of 5 times of diagonal distance of the FDTD grid can satisfy the scattered radiation

Table 4.1: An example of the optimal FDTD parameters in various resolutions

Resolution	0.5 mm	1.0 mm	1.5 mm	2.0 mm
n_d^*	1296	648	432	324
n^*	4629	2315	1543	1158
Running time (s)	14.3	1.75	0.72	0.28

to pass the target and received antennas completely. Table 4.1 shows an example of an optimal FDTD time step and delay parameter based on the 2-D model in 288×265 of 0.5 mm. The running time calculated in a sixteen-antenna system, indicates the average of each antenna FDTD simulation. This test performs on a laptop with Intel Core i7-6700HQ CPU working at 2.60 GHz and in MATLAB 2016b. The complete MATLAB codes for the FDTD forward solver are shown in Appendix A.1.

4.5 Performance of Multiple-frequency Algorithm in Various Resolutions

This section discusses implementation strategies to improve the multiple-frequency DBIM–TwIST algorithm in terms of robustness and resolution. Discussions over how to best use multiple-frequency data to enhance the algorithm's performance are covered. Employing a multiple-frequency structure, seven different hybrid frequency approaches are researched and the impact of the scaling factor is analysed in multiple-frequency reconstruction. Finally, the performances of the three algorithms are compared in various resolutions.

Table 4.2: Seven recipes of hybrid frequency approaches

Name	Hopping method (*iteration No.*)
Freq hopping approach	1→1.5→2→2.5→3→3.5 GHz
Hybrid freq approach 1	1 (20)→ 1.5 + 2 + 2.5 + 3 + 3.5 GHz
Hybrid freq approach 2	1 + 1.5 (20)→ 2 + 2.5 + 3 + 3.5 GHz
Hybrid freq approach 3	1 + 1.5 + 2 (20)→ 2.5 + 3 + 3.5 GHz
Hybrid freq approach 4	1 + 1.5 + 2 + 2.5 (20)→ 3 + 3.5 GHz
Hybrid freq approach 5	1 + 1.5 + 2 + 2.5 + 3 (20)→ 3.5 GHz
Multi-freq approach	1 + 1.5 + 2 + 2.5 + 3 + 3.5 GHz (90)

4.5.1 Multiple-Frequency Optimisation Combined with Frequency Hopping Approach

Our recent DBIM-based work has demonstrated that the combination of multiple-frequency information can enhance performance in terms of both robustness and resolution [131, 132]. A multiple-frequency approach requires a proper dispersion model that should be chosen carefully to reflect true breast tissue dependencies within a frequency range of interest. This work adopts the previously well-established assumption that the single-pole Debye model in (4.2) can cover the range from 1.0 GHz to 3.5 GHz [118, 133, 136], thereby allowing the combining of multiple-frequency data to estimate the unknown Debye parameters in this entire range.

An alternative method for the use of multi-frequency data is based on the frequency hopping approach, where single-frequency reconstructions are performed successively from low to high frequencies [134]. With this approach, the use of low frequencies in the initial inversion stages reduces the nonlinearity of the problem and increases robustness. However, we have argued in previous work that the method may not take full advantage of high frequency data due to a possibly low rank of the monochromatic linear equation [135].

To balance between these two approaches, a variety of hybrid frequency approaches have been tested with the DBIM–TwIST algorithm, which are listed in Table 4.2. We

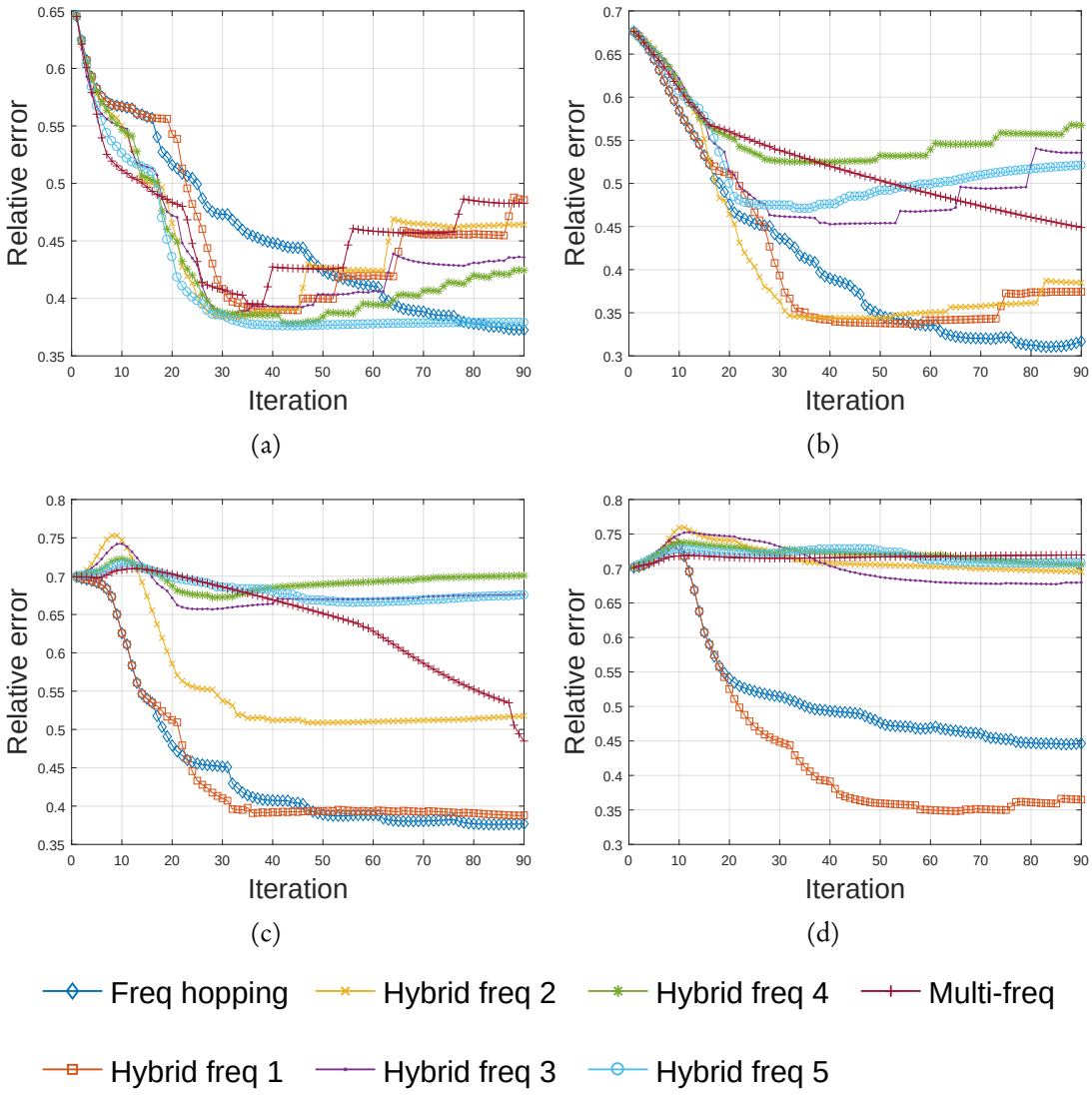

Figure 4.5: Relative reconstruction errors for seven multiple-frequency approaches in the DBIM-TwIST applied to four breast phantoms with unknown skin properties; (a) in Class 1 for 'mostly fatty'; (b) in Class 2 'scattered fibroglandular'; (c) in Class 3 for 'heterogeneously dense'; (d) in Class 4 for 'very dense'.

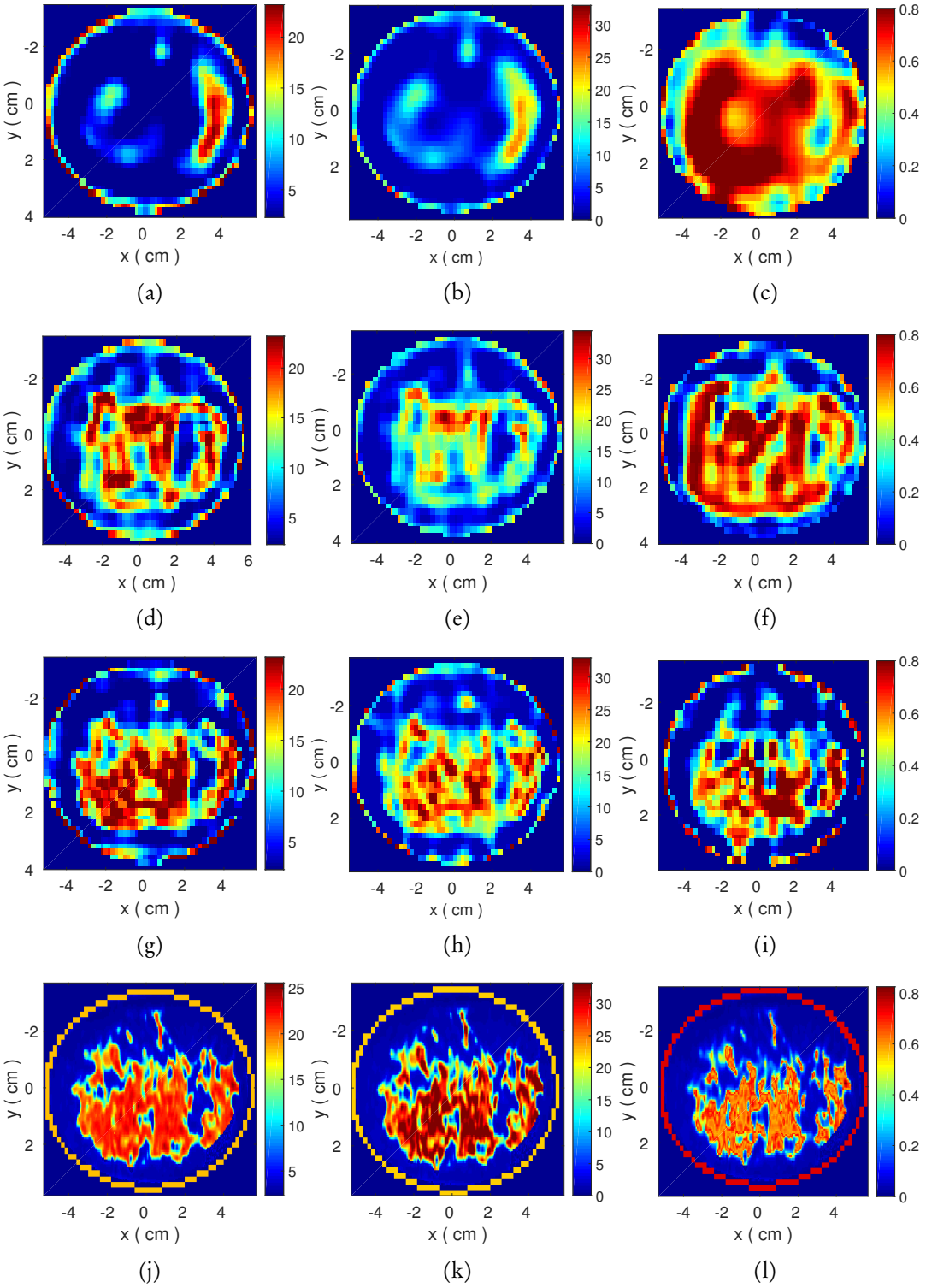

Figure 4.6: Reconstructed images of ϵ_∞ (left column), $\Delta\epsilon$ (middle column), and σ_s (right column) by the multiple-frequency approach in (a—c), freq-hopping approach in (d—f) and hybrid frequency approach 1 in (g—i),based on the 'very dense' breast phantom '012304' in (j—l).

apply a two-step hopping approach, in each of which the multiple frequency approach is employed to reconstruct in 20 and 70 DBIM iterations respectively. Note that for the hybrid freq approach 1, single frequency at 1GHz is used to reconstruct in the first step and hops to the multiple frequency approach with other five frequencies. The hybrid approaches rely on first using one or more of the lowest frequencies from this study's set to provide a crude initial estimate of the breast distribution, which is then used as the starting point for a second DBIM inversion using multiple-frequency data from the remaining frequencies. Note here that the low frequency reconstruction is initialised with the output of the algorithm's first step, which provides the optimised initial guess in terms of the breast average dielectric properties (see Section 5.2.1).

Relative reconstruction errors for all seven approaches and the four breast phantoms are shown in Fig. 4.5. Here, 15 iterations were used per frequency for the frequency hopping approach while the hybrid approaches processes the low frequencies in the first 20 iterations, followed by 70 iterations using data from the rest of the frequencies. It is evident that the frequency hopping approach and the first hybrid frequency approach are the most stable, while other hybrid frequency approaches are not guaranteed to converge to a minimum. Moreover, the hybrid frequency method is much faster than frequency hopping, requiring between 40 and 60 iterations to converge in all cases. Reconstructed images based on the 'very dense' breast phantom are shown in Fig. 4.6. Sub-figure (a—c), (d—f) and (g—i) are obtained by the multiple-freq approach, the freq-hopping approach and the hybrid frequency approach 1 in 90 iterations respectively, while the skin layer is not assumed as *a priori* information. It is simple to identify the hybrid frequency approach 1 as providing the highest accuracy of image reconstruction and more detailed fibroglandular tissues.

4.5.2 Impact of Scaling Factor in Multiple-Frequency Structure

In Section 4.2.1, the scaling factor ω^* has been mentioned to provide solution stability, by balancing the magnitude of three Debye parameters in the matrix A for all reconstructed

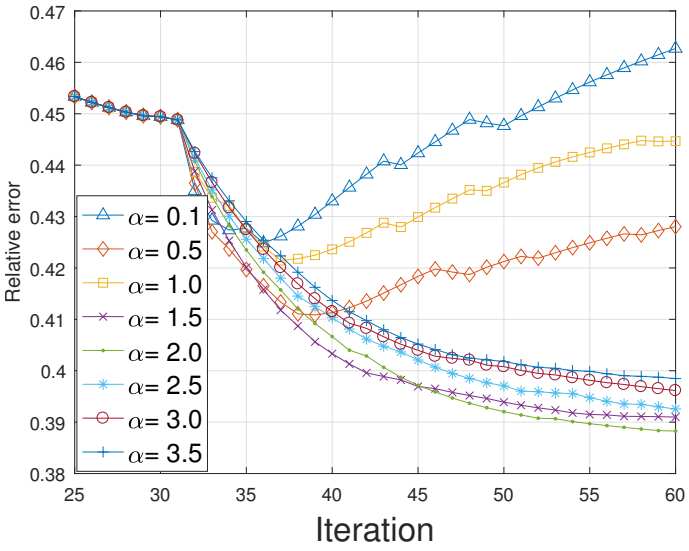

Figure 4.7: Comparison of the reconstruction error of ϵ_∞ by different α

voxels. Note that the factor is only applied to σ_s shown in (4.1). In this section, the impact of the scaling factor will be analysed in the multiple-frequency algorithm, thus applying hybrid approach 1 that was introduced above. In the first step, all cases are reconstructed at 1 GHz in 30 iterations to obtain a stable single-frequency reconstruction result as the new initial guess for the next multiple-frequency process. Then they will be processed following 30 iterations using the remaining frequencies together with different scaling factor settings. The scaling factor is defined as

$$\omega^* = \alpha\omega_s \tag{4.18}$$

where ω_s is set to $2\pi \cdot 10^9$. And the α is discovered from 0.1 to 3.5, corresponding to 8 frequencies from 0.1 GHz to 3.5 GHz. The reconstruction results are shown in Fig. 4.7 and Table 4.3. The Fig. 4.7 demonstrates that the scaling factor has a negative influence on the DBIM reconstruction, when α is below 1.5. A reasonable explanation is that there is no frequency below 1.5 GHz to be used in the multiple-frequency reconstruction process. On the other hand, when α is set to the rest of the value, it provides quite similar results in the end. The final relative reconstruction errors are listed in Table 4.3. It is noted that the best solution is obtained when α is equal to 1.5.

Table 4.3: Relative reconstruction error for different scaling factors

α	0.1	0.5	1	1.5	2.0	2.5	3.0	3.5
Relative error	0.463	0.428	0.447	0.391	0.3988	0.393	0.396	0.399

4.5.3 Analysis of Three Algorithms based on Multiple-Frequency Optimization in Various Resolutions

First, this study demonstrates that using the TwIST method to solve the LIP can increase the robustness of the DBIM algorithm relative to the commonly used CGLS solvers [118, 133]. To this end, the DBIM with the TwIST and the CGLS, and the LSQR in various resolutions have been tested, using the frequency hopping approach (in order to examine the impact of each frequency separately). The parameters adaptive TwIST provides a flexibility of convergence to tackle the various ill-posedness in different resolutions. Besides, as relying on the setting of iteration number, the CGLS is applied with the L-curve technique to locate an optimal step number. In comparison, the LSQR converges faster than the CGLS without a parameter. Comparison of relative reconstruction errors are shown in Fig. 4.8 and Fig. 4.9, where it is evident that the adaptive TwIST performs the best in low ill-posed condition (corresponding to 2 mm), with an almost identical convergence rate against the LSQR. However, for higher resolutions of 1 mm where ill-posedness increases, the TwIST algorithm becomes a little unstable, compared with the LSQR. One reason for this is that the adaptive approach in this case cannot ensure the algorithm's stability. A possible remedy to the increased several ill-posedness in higher resolution, is to increase the number of the DBIM iterations in low frequency (such as at 1 GHz in the case) which can improve the convergence stability and enhance the quality of the reconstructed image. It is proven in Fig. 4.10 that the convergences of three algorithms are smoother and faster, when the DBIM iteration number increases from 15 to 30 at 1 GHz.

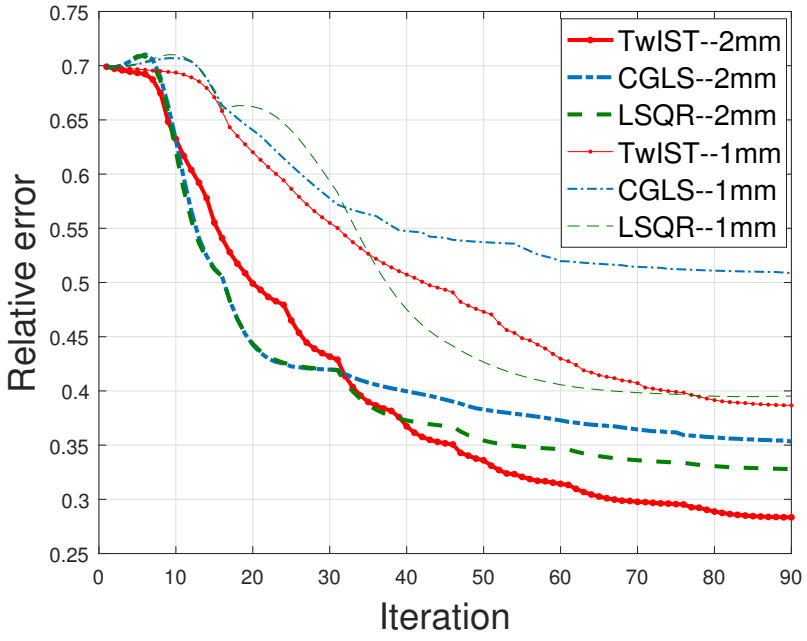

Figure 4.8: Comparison of relative reconstruction errors by the TwIST, CGLS, and LSQR algorithms in resolutions of 2 mm and 1mm.

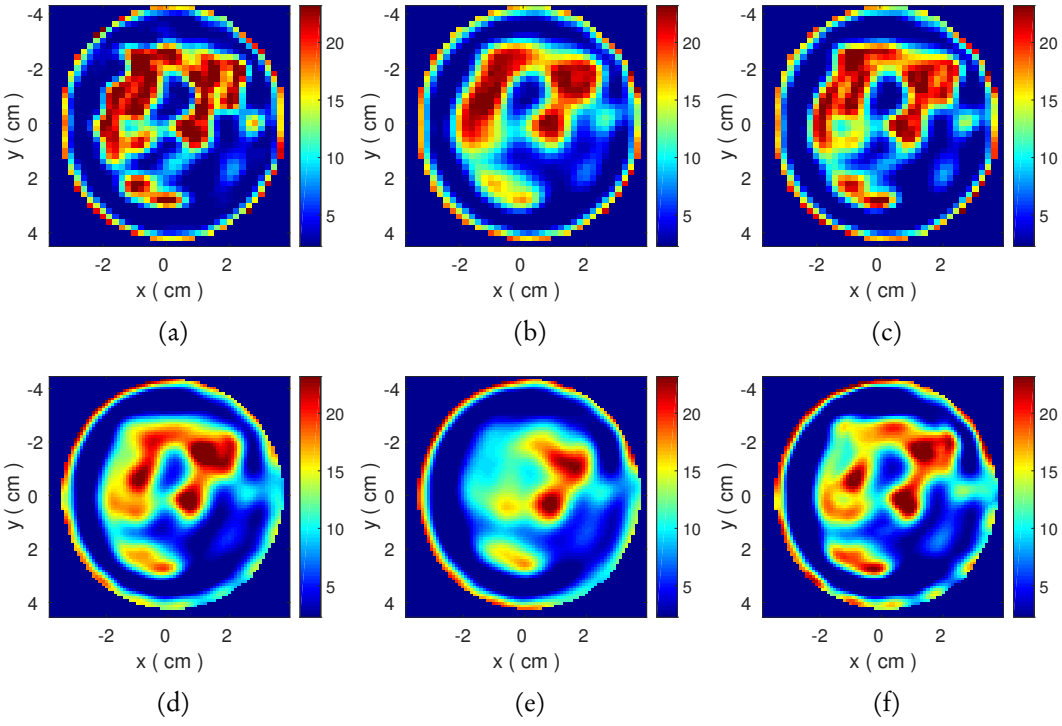

Figure 4.9: Reconstructed images of ϵ_∞ by the TwIST, CGLS, and LSQR algorithms in resolution of 2 mm and 1 mm. (a) the adaptive TwIST in 2 mm; (b) the CGLS combined L-curve technique in 2 mm; (c) the LSQR in 2mm; (d) the adaptive TwIST in 1 mm; (e) the CGLS combined L-curve technique in 1 mm; (f) the LSQR in 1mm.

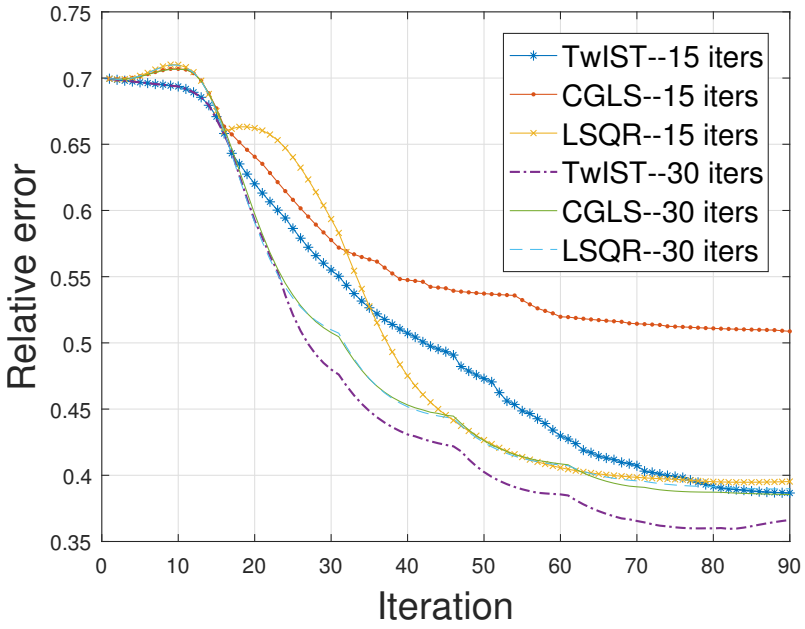

Figure 4.10: Effect of increasing number of the DBIM iterations at 1 GHz based on the TwIST, CGLS, and LSQR reconstructing in 1 mm.

4.6 Conclusion

This study presented a novel multiple frequency DBIM algorithm for microwave breast imaging based on the TwIST method. It was argued that this implementation is more flexible and robust than the CG methods as a solver of the ill-posed linear problem, by employing the L-curve technique for CGLS. By using a hybrid multiple-frequency approach, an optimal trade-off between imaging accuracy and reconstruction stability has been achieved for this method. Besides, an optimisation strategy has been proposed to speed the FDTD simulation time. Finally, the reconstructed performances of three iterative algorithms have been shown in various resolutions.

Chapter 5

IMPROVEMENT STRATEGIES BASED ON MULTIPLE-FREQUENCY DBIM-TWIST ALGORITHM

5.1 Introduction

This section discusses implementation strategies to improve the DBIM–TwIST algorithm in terms of robustness and resolution. First, we present a two-step reconstruction approach, where the first step considers a homogeneous breast interior and uses the DBIM to obtain an initial guess which corresponds to average properties of the true breast tissue composition. This step is critical for the DBIM to converge to an optimal solution (global minimum), as GN algorithms can be very sensitive to the initial guess in applications such as medical imaging, where very little *a priori* information may be available [151, 152]. In particular, an initial guess provides the starting point for these convex optimization algorithms, and inaccurate information can lead to false solutions that fit the data but are completely different from the ground truth [153]. Our

approach adds low computational cost to the final breast reconstructions, and improves significantly the reconstruction quality for different breast phantoms.

Moreover, we present a new method for regularizing the unconstrained optimization problem based on L^1 norm minimization and the TwIST method. This is motivated by recent work in medical applications, where regularization methods based on the L^1 norm or total variation (TV) principle have become popular instead of L^2 norm regularization approaches [154]. These methods impose less smoothing on the reconstruction image. Our research implements the Pareto curve for finding the L^1 norm regularization parameter of the TwIST algorithm, which defines the optimal trade-off between the L^2 norm of the residual and the L^1 norm of the solution [155]. The non-stationary convergence of the TwIST method does not ensure differentiability and continuity of the Pareto curve, as in stationary iterative methods such as conjugate gradient method. We therefore employ curve fitting method of cubic polynomials to smooth the Pareto curve. And then we apply an exponential distribution sampling of the regularization parameter to reduce computation cost.

Combined with the multiple-frequency DBIM-TwIST algorithm and relevant optimisation methods in the previous chapter, these new strategies, which are presented in a unified framework within the DBIM, provide some unique capabilities of our algorithm relative to recently proposed alternative methods. For example, Nikolova et al. in [156, 157], presented an interesting and effective holography method for reconstructing targets in the near-field range, which relies on an alternative formulation of the problem. Similarly, theoretical and experimental work by LoVetri et al. has also focused on 2-D wideband MWI using various approaches including the DBIM [158], but the employed optimization and regularization strategies are very different from this work. Moreover, the importance of the initial guess in the convergence of the algorithm has been demonstrated in numerous papers (see for example [151]), but the approach presented here to tackle this problem has not been considered previously, to the best of our knowledge.

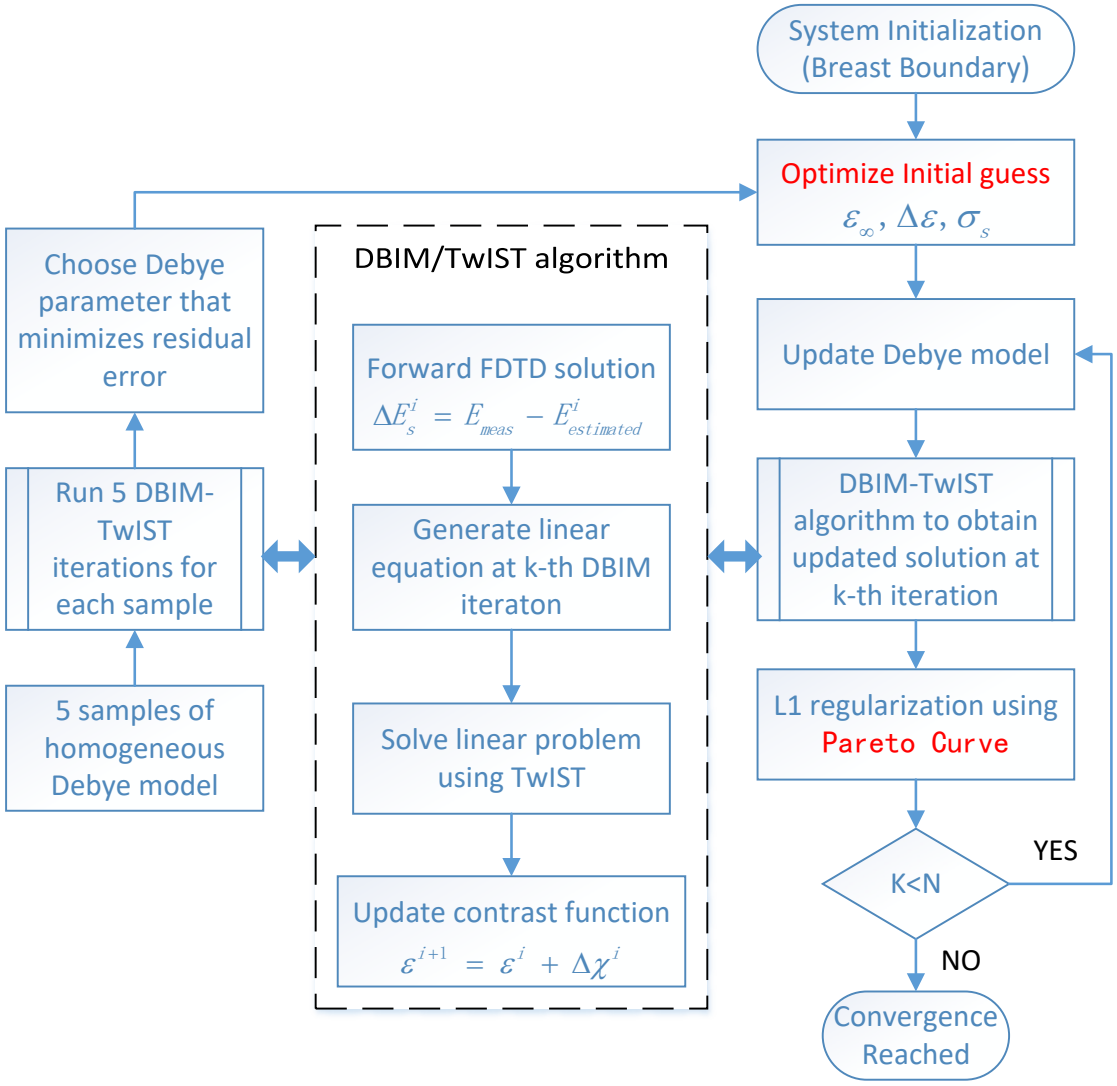

Figure 5.1: Flow chart of the multiple-frequency DBIM–TwIST algorithm

For all our results, our reconstruction approach employed the DBIM–TwIST algorithm in conjunction with the optimisation strategies as illustrated in Fig. 5.1. The DBIM–TwIST algorithm is invoked both in the first step of finding the optimal initial guess (average breast properties) and in the main reconstruction of the inhomogeneous breast structure. A single frequency approach at 1 GHz is used in the first step, and its outcome initialises the optimal multiple-frequency approach employed in the second step of the process.

5.2 Methodology

5.2.1 Optimised Initial Guess of Breast Average Dielectric Properties

Iterative local optimisation methods, such as the DBIM method, are sensitive to the adopted 'initial guess' of the reconstruction domain [151], which can result in the convex optimisation algorithm converging to a false solution. In addition to increasing stability, a good initial guess can speed up convergence and thus reduce computational time. Obtaining an accurate initial guess can be challenging in applications such as breast imaging, where very little information (e.g. the breast surface) may be known as *a priori*. To this end, a very simple process to estimate the average breast dielectric properties is proposed, which relies on the following: 1) assume the breast is homogeneous and filled with normal tissue, and run the DBIM–TwIST algorithm for a fixed number of iterations; and 2) apply this process to a number of samples (which we term 'Cases') within a well-known range of values for normal breast tissue to determine the optimal initial guess of the average breast dielectric properties, based on minimising the data residual.

As an example of implementing this approach, 5 samples of the 3 Debye parameters are chosen. These are evenly spaced within the range used to model normal breast tissue

Table 5.1: Five cases of estimated initial guesses based on the single-pole Debye model

Sampling	ϵ_∞	$\Delta\epsilon$	$\sigma_s(S/m)$	$\tau(ps)$
Case 1	4.68	3.21	0.088	17.125
Case 2	7.835	7.26	0.2	17.125
Case 3	10.99	11.3	0.311	17.125
Case 4	14.145	15.35	0.423	17.125
Case 5	17.3	19.4	0.535	17.125

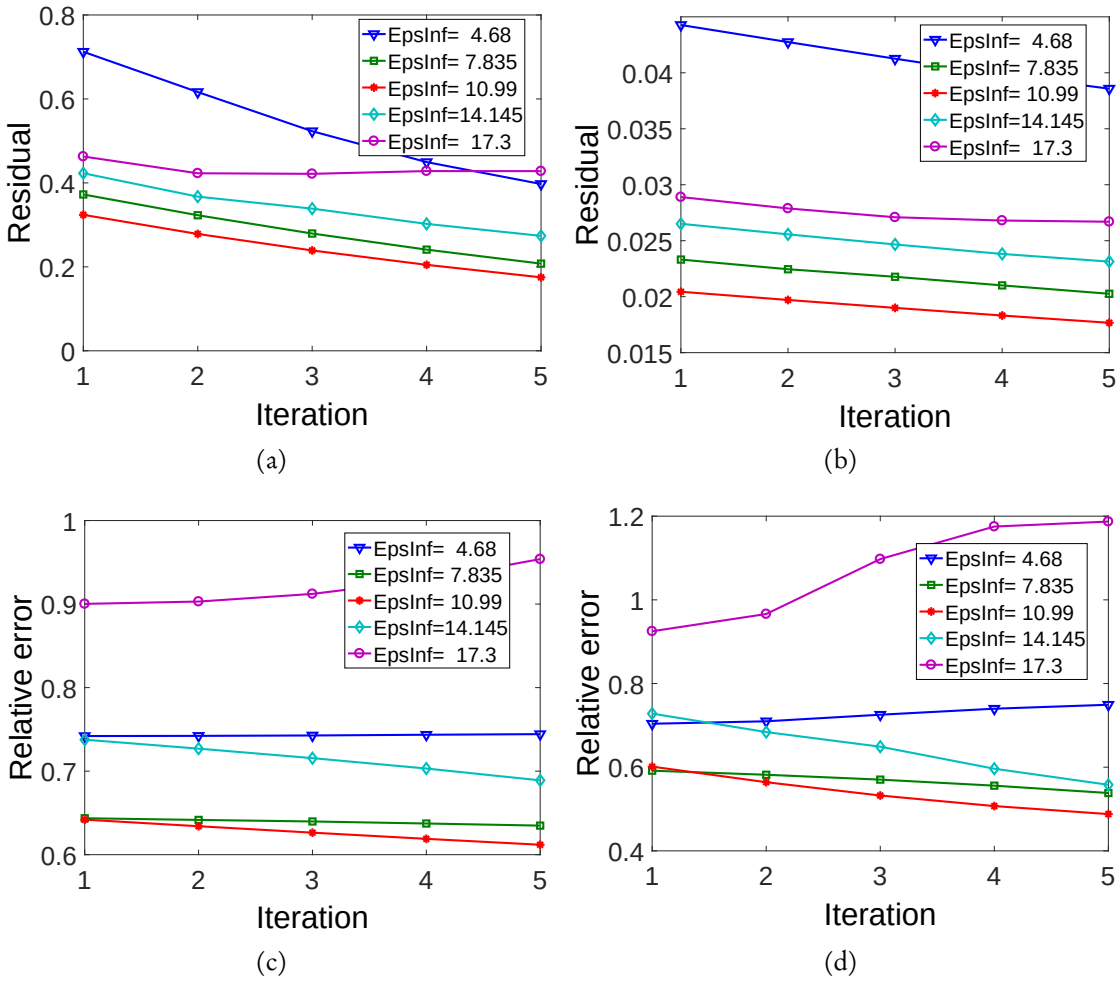

Figure 5.2: Illustration of the proposed method to select an optimal initial guess for microwave breast imaging. Here we consider five samples from the normal breast tissue range shown in Table 5.1 are considered. Each sample is used as the starting point of DBIM–TwIST, which is run for 5 iterations for a fixed homogeneous breast with unknown skin properties. The residual and relative reconstruction errors vs iteration number are plotted in (a) and (c) for 2 mm resolution, and in (b) and (d) for 0.5 mm.

shown in Table 5.1 ('Cases' 1–5), where the parameters of Cases 1 and 5 represent the mean of adipose breast tissue and fibroglandular breast tissue respectively [133]. Then 5 iterations of the DBIM–TwIST are run for each of the 5 cases to select the initial guess with the smallest data residual. This process yields the three Debye parameters of the homogeneous breast interior that reflect the closest estimate to its average dielectric properties and are used as the optimal initial guess in the second step of the DBIM algorithm, to estimate the inhomogeneous breast structure.

Fig. 5.2 illustrates the evolution of this process for a heterogeneously dense phantom based on a single-frequency reconstruction at 1 GHz. The data residuals and relative reconstruction errors against the original model are plotted at each DBIM iteration for reconstruction resolution of 2 mm in (a) and (c), and 0.5 mm in (b) and (d). The residual and relative errors exhibit similar trends for all cases. Moreover, the similarity of the results in 2 mm and 0.5 mm confirms that it is sufficient to use a 2 mm resolution grid for optimising the initial guess in this first step of the algorithm even if the final (heterogeneous) images are reconstructed in higher resolutions. The complete MATLAB codes have been shown in Appendix A.3.

5.2.2 L^1 Norm Regularisation with the DBIM-TwIST Method

Thresholding algorithms such as the TwIST promote sparse solutions of the LIP. The TwIST can therefore be regularised using tools employed by other sparse-promoting algorithms, such as the basis pursuit (BP) problem. BP aims to identify a sparse solution of the underdetermined system of equations $Ax = b$, where A is an m-by-n matrix and b is m-by-1 vector. Again, if $m << n$, this problem is ill-posed. The approach introduced by Chen, Donoho and Saunders [159], is to solve the convex optimisation problem,

$$\min_x \|x\|_1 \quad \text{subject to} \quad Ax = b. \tag{5.1}$$

However, it is undesirable to fit exactly the linear system because of noisy or imperfect data. Therefore, other possible formulations of the L^1 norm regularised least-squares problem have been proposed based on the penalised least-squares problem,

$$\min_x \quad \|Ax - b\|_2^2 + \lambda\|x\|_1, \tag{5.2}$$

which is proposed by Chen, Donoho and Saunders [159], and an explicit L^1 norm constraint problem known as the Lasso problem,

$$\min_x \quad \|Ax - b\|_2 \quad \text{subject to} \quad \|x\|_1 \leq \tau. \tag{5.3}$$

The formulation of (5.2) is well-suited to the TwIST method because of its close connection to convex quadratic programming, for which an explicit expression of the de-noising function can be obtained in closed form. Let x_λ denote the optimal solution of (5.2). The residual function,

$$\phi(\lambda) = \|Ax_\lambda - b\|_2 \tag{5.4}$$

gives the minimal residual of (5.2) for each $\lambda \geq 0$.

To obtain the optimal value of λ for $\Phi(\lambda)$, the Pareto curve is employed, which can yield the optimal trade-off between minimising the L^2 norm of the residual r and the L^1 norm of the solution x, as shown in Fig. 5.3 for a typical LIP. As the TwIST method is a non-stationary method, the function of (5.4) is not strictly non-increasing and not smooth. Therefore curve fitting is applied using cubic polynomials to approximate the function and its derivative. The curve then becomes continuously differentiable and convex, and the residual ϕ will decrease as λ increases.

Subsequently, a log-log scale is used to plot the norm of residual ϕ on the abscissa against the L^1 norm of solution x for the parameter λ. Then, a point λ_{opt} corresponding to the maximum of the curve slope can be localised. As shown in Fig. 5.3(b), the

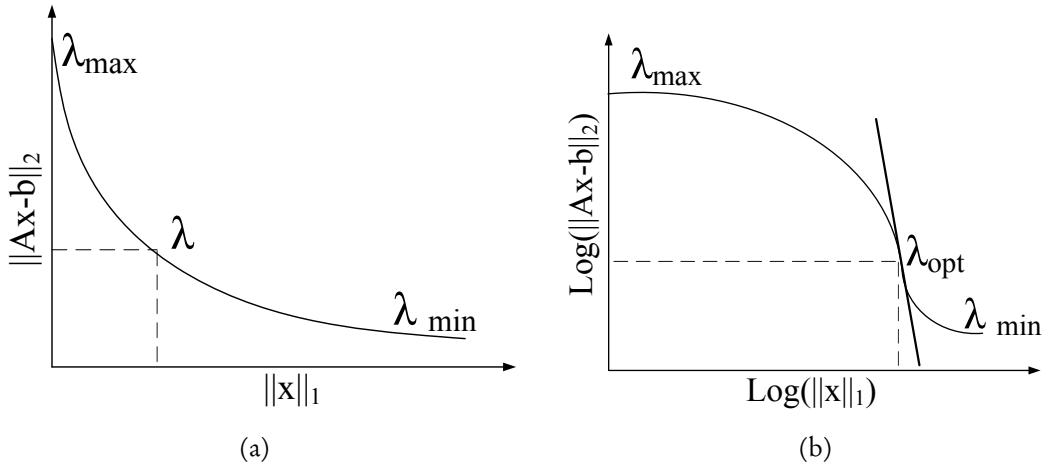

Figure 5.3: A typical Pareto curve (a) and Pareto curve in log-log scale (b), which is used to choose the optimal value of the L^1-regularisation parameter λ.

smallest increase in $\|x\|$ leads to the greatest decrease in $\phi(\lambda)$ around this point. This process is similar to using the L-curve method for L^2 norm regularisation problems [160]. However, the L-curve in log-log scale is a convex downward, but the Pareto curve in log-log scale is a convex upward (even if the original Pareto curve is convex downward).

To reduce the computation cost, the value of λ is chosen based on an exponentially decreasing function from $\|A^T b\|_\infty$ to zero, which is defined as,

$$\lambda(n) = \|A^T b\|_\infty \cdot \delta^n \qquad n \in \mathbf{Z}^+ \tag{5.5}$$

where δ denotes a decreasing factor with $0.1 < \delta < 1$, $(\cdot)^T$ denotes a transpose operator, and $\|\cdot\|_\infty$ denotes the infinity norm. In (5.5), δ is used to control the number of samples for the parameter λ. When δ tends to 1, a more accurate Pareto curve is obtained at the expense of a very high computational cost. Conversely, the number of samples becomes insufficient as δ approaches 0.1. In our numerical experiment, a reliable range of δ is found between 0.3 and 0.5, and any choice in this range comes with a low computational cost.

Finally, it is important to emphasise that, contrary to commonly used L^1 norm approaches, the method utilised in this study combines the Pareto curve with an adaptive

Table 5.2: Relative error of reconstructions of ϵ_∞

Model	Default initial guess / Optimised initial guess			
	2 mm	1.5 mm	1 mm	0.5 mm
Class 1	0.264/0.272	0.289/0.301	0.332/0.335	0.429/0.417
Class 2	0.233/0.241	0.266/0.265	0.320/0.297	0.554/0.373
Class 3	0.306/0.312	0.342/0.319	0.380/0.298	0.682/0.361
Class 4	0.473/0.235	0.504/0.261	0.694/0.268	0.707/0.332

This is based on the default initial guess and the optimal initial guess for 4 breast phantoms introduced in Section 2.3, including mostly fatty, scattered fibroglandular, heterogeneously dense and very dense breasts from Class 1 to 4.

strategy to optimise the L^1 regularisation based on the residuals of the TwIST iterations at each DBIM iteration, which has been detailed in [132]. The complete MATLAB code are shown in Appendix A.4.

5.3 Reconstructed Results

5.3.1 Effect of Optimising Initial Guess by Estimating the Breast Average Dielectric Properties

To illustrate the advantage of optimising the initial guess for the breast average dielectric properties in the DBIM, axial slices have been reconstructed from four UWCEM breast phantoms (see Section 2.3) in resolutions of 2 mm, 1.5 mm, 1 mm and 0.5 mm. The reconstructed images of ϵ_∞ and σ_s using a fixed initial guess versus an optimised initial guess in 2 mm and 0.5 mm are shown from Fig. 5.4 to Fig. 5.7, respectively. Relative errors computed for the same parameter are given in Table 5.2. Note that the fixed initial guess values are chosen in the middle of the range for the Debye parameters of normal breast tissue.

These images and error values suggest that optimising the initial guess leads to sufficiently accurate distribution estimates for all resolution ranges, while omitting this step can compromise imaging performance. This is particularly true in all resolution

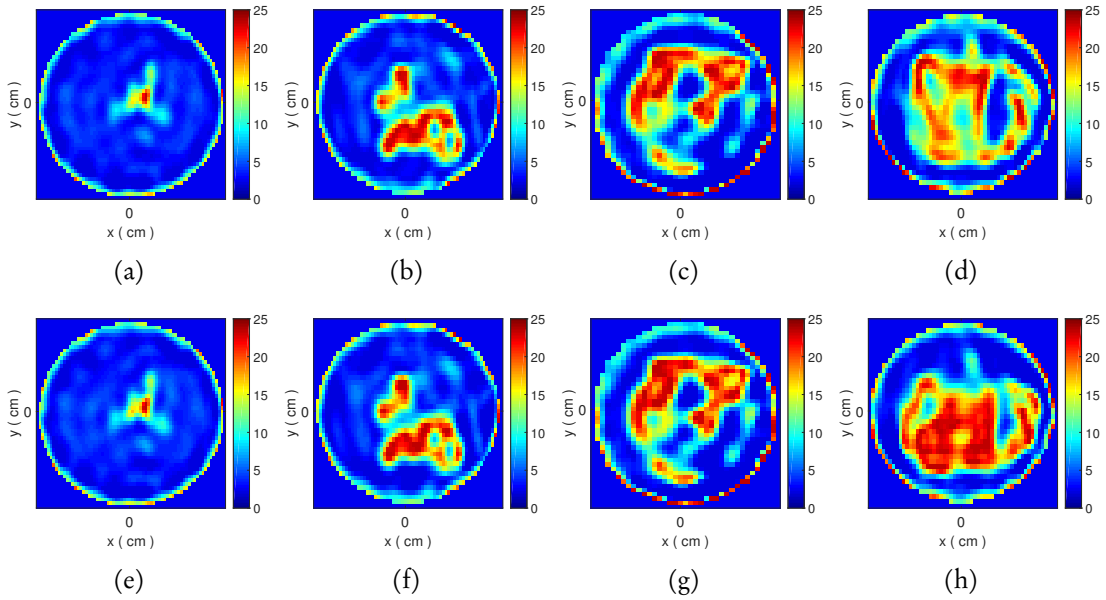

Figure 5.4: Reconstructed images of ϵ_∞ without and with optimisation of initial guess for 4 phantoms in 2 mm. (a–d) Reconstructions with a fixed initial guess representative of normal breast tissue average properties ($\epsilon_\infty = 5.76, \Delta\epsilon = 5.51, \sigma_s = 0.0802$); (e–h) Reconstructions with an optimised initial guess.

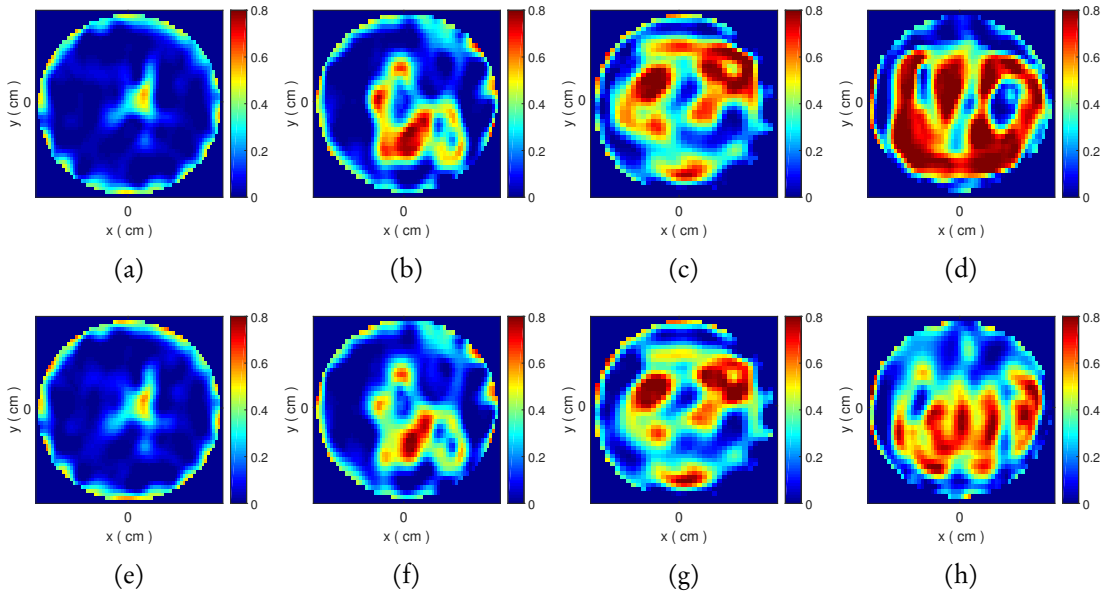

Figure 5.5: Reconstructed images of σ_s without and with optimisation of initial guess for 4 phantoms in 2 mm. (a–d) Reconstructions with a fixed initial guess representative of normal breast tissue average properties ($\epsilon_\infty = 5.76, \Delta\epsilon = 5.51, \sigma_s = 0.0802$); (e–h) Reconstructions with an optimised initial guess

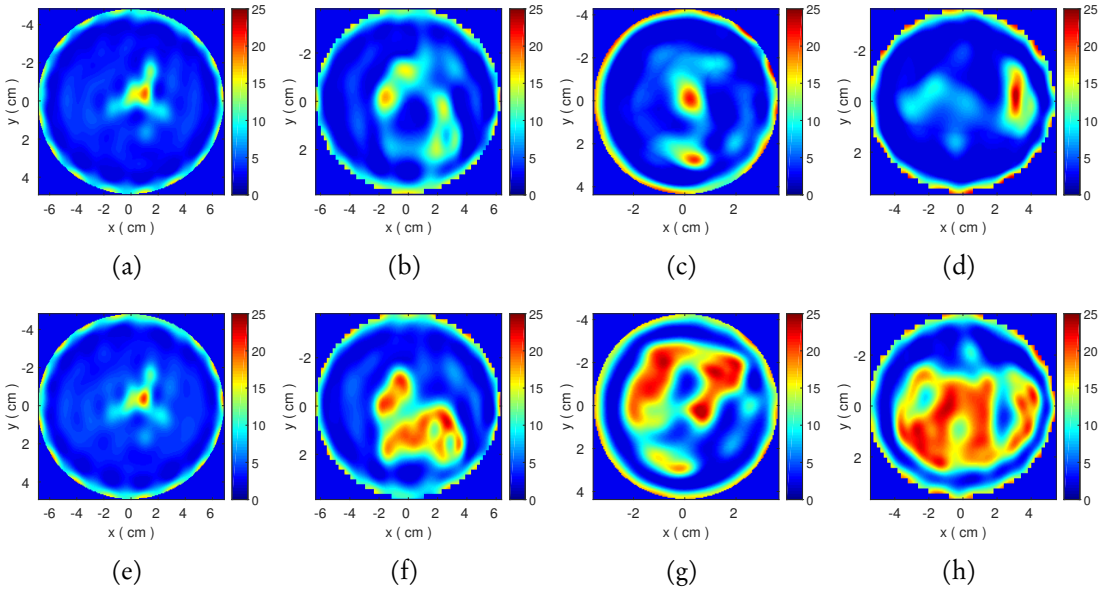

Figure 5.6: Reconstructed images of ϵ_∞ without and with optimisation of initial guess for 4 phantoms in 0.5 mm. (a–d) Reconstructions with a fixed initial guess representative of normal breast tissue average properties ($\epsilon_\infty = 5.76, \Delta\epsilon = 5.51, \sigma_s = 0.0802$); (e–h) Reconstructions with an optimised initial guess.

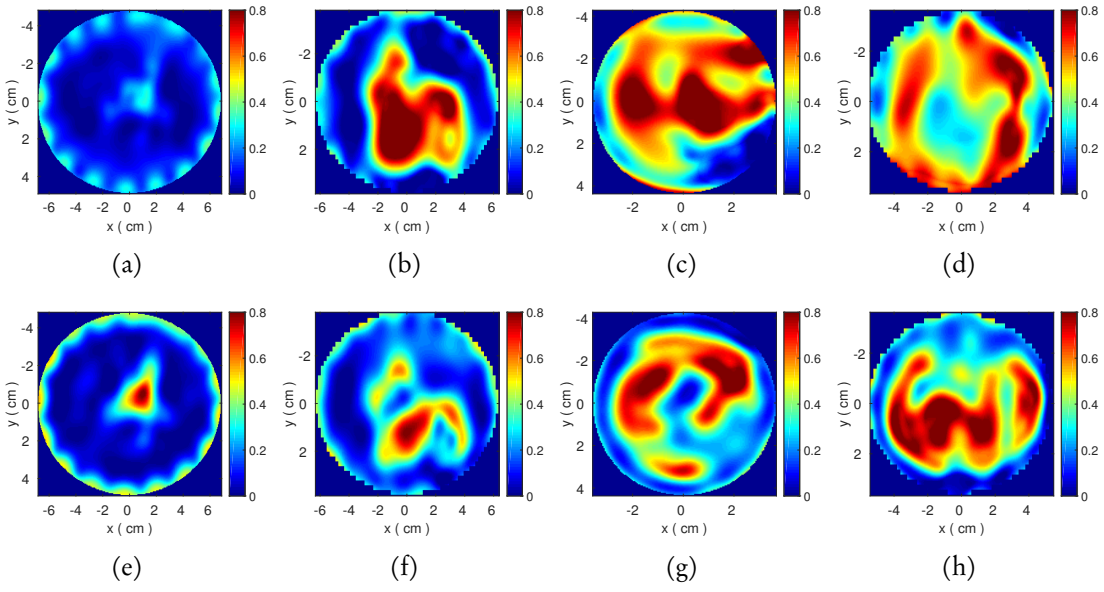

Figure 5.7: Reconstructed images of σ_s without and with optimisation of initial guess for 4 phantoms in 0.5 mm. (a–d) Reconstructions with a fixed initial guess representative of normal breast tissue average properties ($\epsilon_\infty = 5.76, \Delta\epsilon = 5.51, \sigma_s = 0.0802$); (e–h) Reconstructions with an optimised initial guess

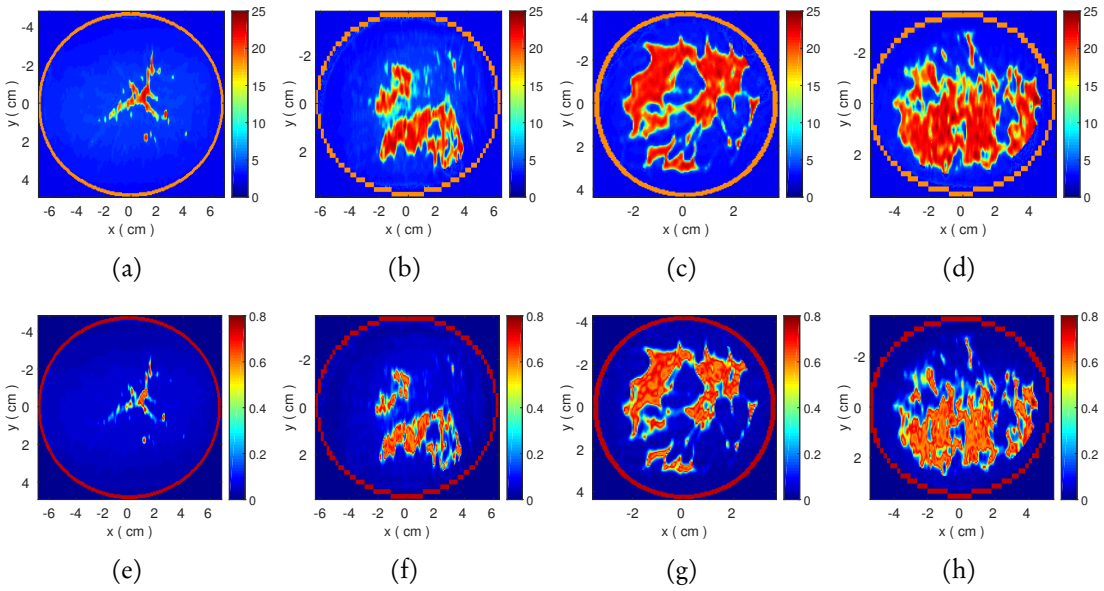

Figure 5.8: Original 2-D images of 4 breast phantoms (mostly fatty, scattered fibroglandular, heterogeneously dense and very dense from left to right). (a–d) is ϵ_∞; (e–h) is σ_s.

grids for the very dense breast phantom, where the difference in the Debye parameters of the fixed initial guess from the true average Debye parameters is the most significant. It is also true for 3 of the 4 phantoms in the highest 0.5 mm resolution grid, where the number of unknowns (and thus the degree of ill-posedness of the LIP) increases dramatically relative to the low 2 mm resolution grid. Besides, Fig. 5.5 and Fig. 5.7 demonstrate more significant improvement in the conductivity part which is harder for reconstruction than permittivity. Therefore, optimising the initial guess can increase the algorithm's robustness and enhance the accuracy of reconstruction in high resolution.

5.3.2 L^1 Norm Regularisation Effect

In all the previous reconstructions, stability in the DBIM–TwIST algorithm has been achieved by terminating the TwIST iterations based on an adaptive strategy presented in previous work [132]. Although noise has not been added to the simulated data, this implicit regularisation strategy can ensure stability in cases of noise or measurement uncertainties, similar to previous implementations using the CGLS method [121, 131,

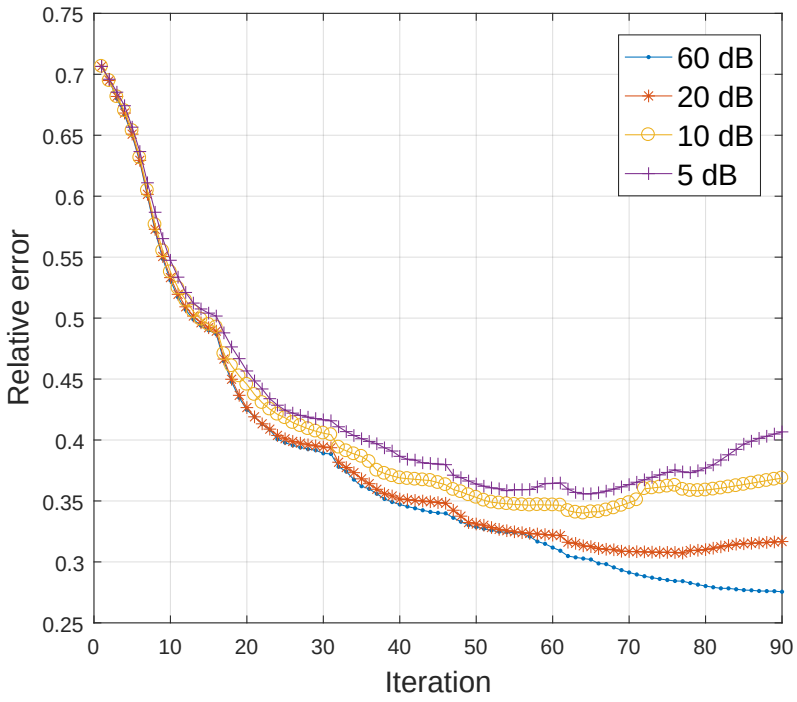

Figure 5.9: Comparison of reconstruction quality for different SNR levels of noise and phantom '062204'.

133]. To illustrate this, reconstructions of Section 5.3.1 have been repeated with an increasing level of noise in the data, and the relative reconstruction errors have been plotted against the experimental phantom '062204' in Fig. 5.9. The plot confirms that convergence is not affected by noise levels with signal to noise ratios (SNRs) as low as 20 dB, but for lower SNRs there is noticeable degradation in the reconstruction quality.

It is important to note that these low SNRs would not correspond to thermal noise in an experimental MWI system, but rather to errors due to measurement uncertainties, environmental factors and mismatch errors between this model and a true experiment. These errors depend on the signal level at each antenna. This 'measurement noise' has been modelled as an additive Gaussian in the absence of a better model, with the power level dependent on the signal at each antenna. Noise of the same power at each antenna would correspond to thermal noise, which would be well below the level of the signals that are processed by our algorithm and would therefore have a negligible effect in our reconstructions.

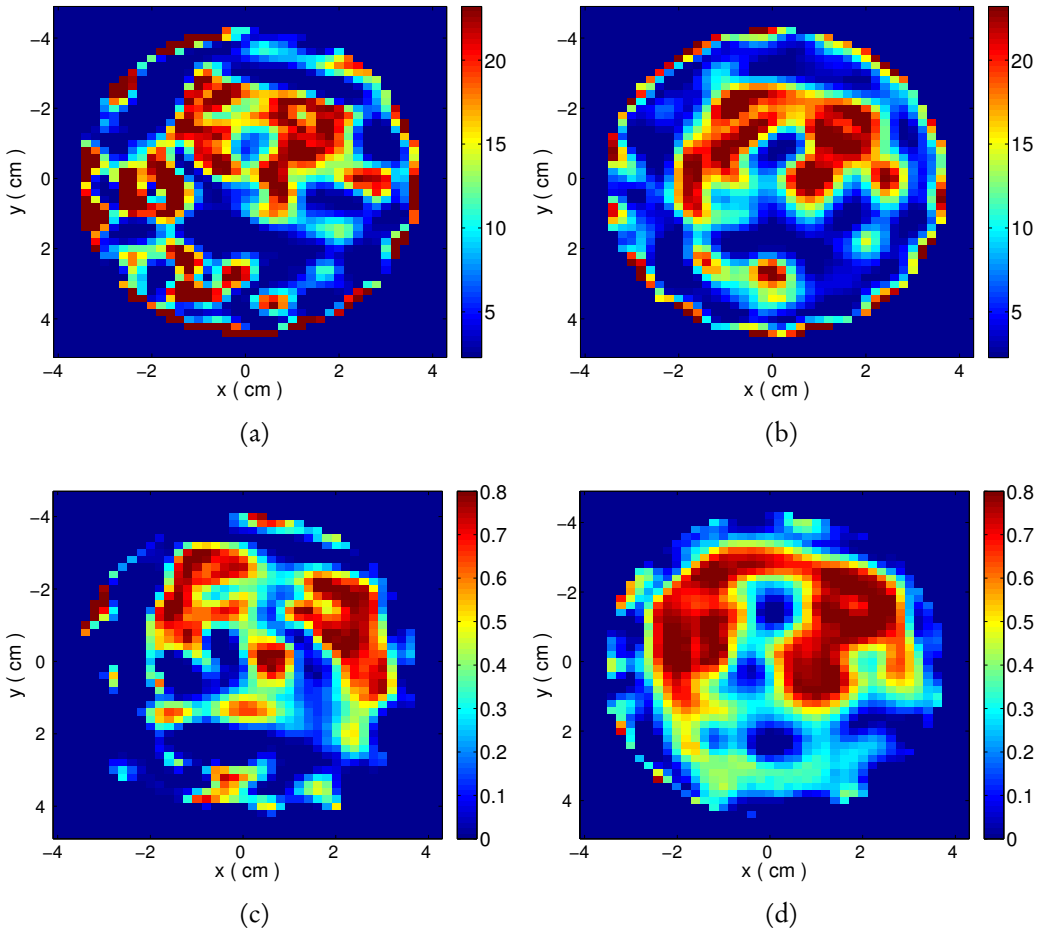

Figure 5.10: Reconstructed images of ϵ_∞ and σ_s in 2 mm under 5 dB noise. Top: Estimates of ϵ_∞ without (a) and with (b) L^1 regularisation. Bottom: Images of σ_s without (c) and with (d) L^1 regularisation.

To deal with cases of very low SNR where the TwIST termination criterion is not sufficient to guarantee optimal convergence, (10 dB or below in Fig. 5.9), the L^1 regularisation strategy can be employed based on the Pareto curve analysis presented in Section 5.2.2. To illustrate the effect of L^1-regularisation approach, the reconstructed images of ϵ_∞ and σ_s are compared in Fig. 5.10 without and with our L^1 regularisation for an SNR of 5 dB. These images demonstrate that our L^1 regularisation approach can assist in recovering the true breast composition, while very strong noise artefacts occur when the DBIM–TwIST is implemented without the L^1-regularisation correction. As expected, noise artefacts are stronger in the fatty tissue, and affect the σ_s images more than ϵ_∞.

5.4 Impact of Uncertainties in Prior Information and Losses in Coupling Medium

The previous reconstructions assumed prior knowledge of the outer outline of the breast model and a fixed relaxation time τ for all Debye parameters. Moreover, a hypothetical lossless coupling medium with low dielectric constant has been considered, motivated by the use of low-loss coupling media such as safflower oil. In this section, the impact on the reconstruction due to losses in the coupling medium is considered, as well as the effect of uncertainties in the knowledge of the breast outline and the relaxation constant.

The impact of the coupling medium in microwave breast imaging has been considered in various previous studies, both in radar-based and tomographic approaches. For example, its effect in terms of signal level has been studied in [161], while the use of losses to reduce unwanted signals in microwave tomography has been demonstrated in [162]. It is evident that a lossy coupling medium will reduce the level of signals scattered by the breast, and this loss of information can affect the quality of reconstructions.

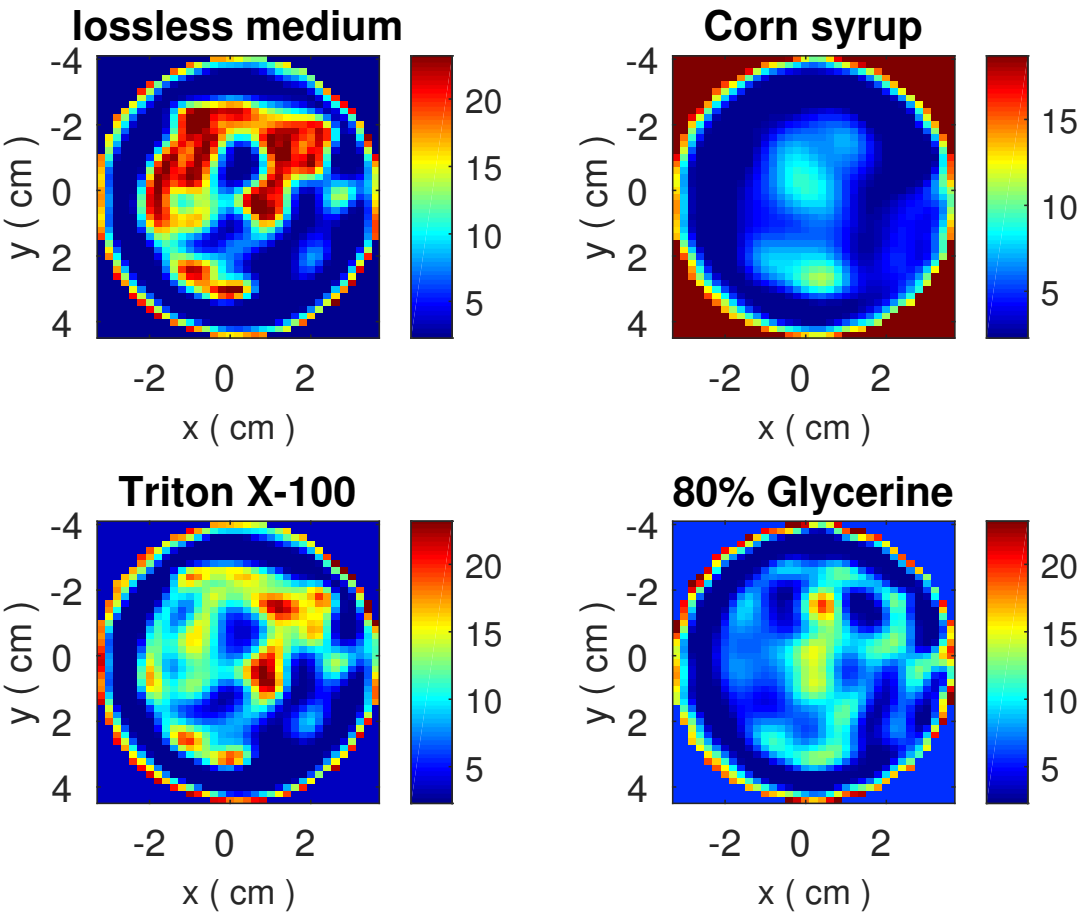

Figure 5.11: Reconstructed images in different lossy coupling media

Table 5.3: Relative reconstruction errors for various coupling media based on the phantom '062204'

coupling medium	ϵ_∞	$\Delta\epsilon$	σ_s	τ	Relative error
Ideal lossless	2.6	0	0	17.1	0.322
Corn syrup	18.7	0	0.64	13.6	0.698
Triton X-100	3.51	2.58	0.066	41.6	0.415
80% Glycerine	5.73	16.7	0.415	111.1	0.621

Table 5.4: Relative reconstruction errors for phantom '062204' due to uncertainties in the breast outline

Error of model's dimension		Error of model's position	
model error	Relative error	model error	Relative error
2.67%	0.376	5.65%	0.450
8.40%	0.450	8.84%	0.544
15.97%	0.430	16.05%	0.597

Table 5.3 and Fig. 5.11 quantify the effect of considering several commonly used lossy coupling media, such as 'corn syrup', Triton X-100 and 80% glycerine. Here, 'corn syrup' 'Sample 1' is employed from [163], and the data of the Triton X-100 and 80% glycerine are based on this study's measurements. It is evident that a higher conductivity in the coupling medium leads to less accurate reconstructed images due to the additional signal loss. This was confirmed by performing additional reconstructions for hypothetical media with the same dielectric constants as in Table 5.3 but without losses, where no degradation in quality was observed.

The breast and skin layer's position is the crucial prior information for the MWI reconstruction. In realistic experiment, we can detect the skin layer by a series of scanning technologies, such as the 3-D laser scanning technology, but it may be impossible to have exact knowledge of the outer outline of the breast model. Thus, an error level analysis was performed for uncertainties in the position and size of the breast structure, presented in Table 5.4. Reconstructions with uncertainties in the assumed breast size and position have been analysed separately. Their errors are calculated in this table and reconstructed images are shown in Fig. 5.12 and Fig. 5.13. The relative reconstruction error is not affected significantly by uncertainties in the breast size, but misalignments of the assumed breast outline from the true position affect the reconstruction quality only for over 8% error. These results suggest that the algorithm is robust with respect to uncertainties in the knowledge of the breast shape.

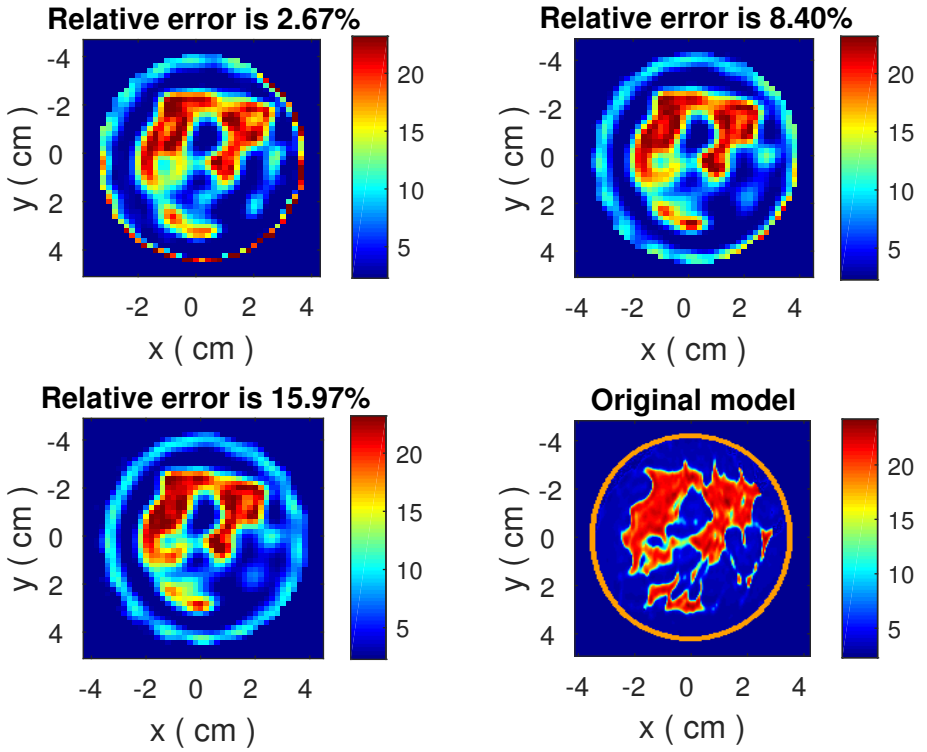

Figure 5.12: Reconstructed images due to the error of model's dimension

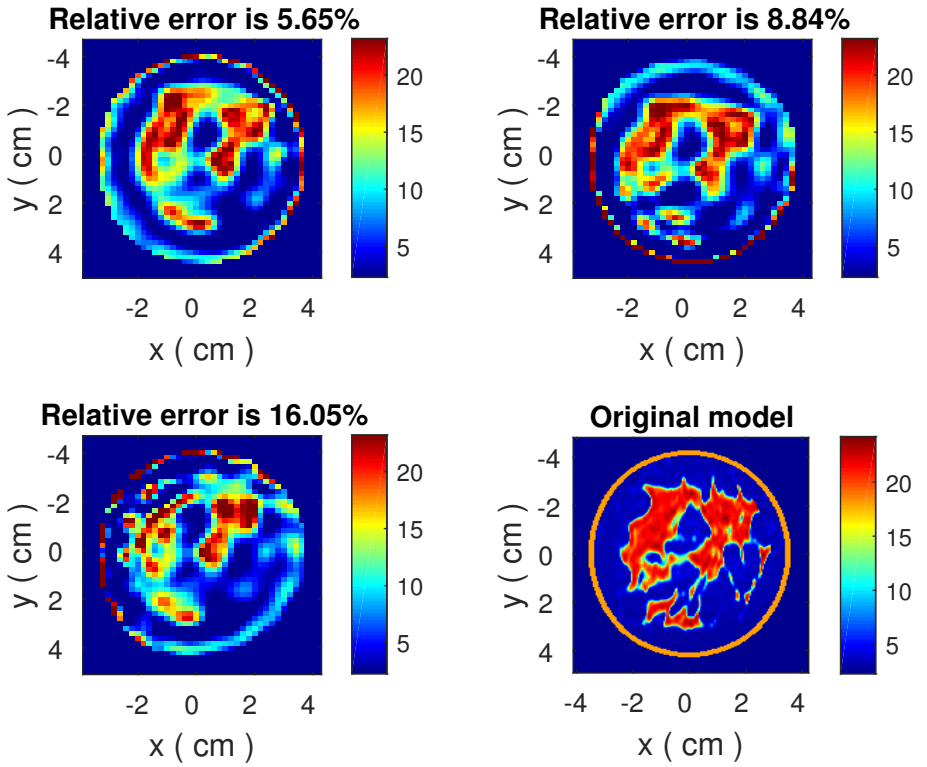

Figure 5.13: Reconstructed images due to the error of model's position

Table 5.5: Relative reconstruction errors for phantom '062204' due to various biases of τ in different coupling mediums

Precise relaxation time		Relative error		
coupling medium	$\tau(ps)$	5%	10%	20%
Ideal lossless	17.1	0.3789	0.3777	0.3798
Corn syrup	13.6	0.7004	0.6998	0.7045
Triton X-100	41.6	0.5299	0.5627	0.6307
80% Glycerine	111.1	0.6656	0.6893	0.7224

Finally, the impact of performing reconstructions in different mediums with a relaxation time τ was also examined, which is different from the assumed value of 17.125 ps for the breast tissue Debye models by a variation of up to 20%. Our results in Table 5.5 remain unaffected by this mismatch in the assumed model, producing visually similar images and relative error with a maximum variation of 1% for ideal losses and 'corn syrup'. However, the variation of relative error increases to over 10% for the rest of two high lossy mediums, which evidences higher sensitivity of high-loss coupling media when inevitable uncertainties appeal in the process of experimental measurement and reconstruction algorithm.

5.5 Conclusion

In this chapter, we have proposed a new approach to obtain an optimised initial guess of the average breast tissues properties by sampling along the range of possible values while also running a few DBIM iterations to identify the minimum error. Considering the condition of the limit number of antennas given by (4.3), we use 16-antenna system with point source in 2-D as the simulation testbed. Six sampling frequencies are selected at 0.5 GHz spacing from 1.0 to 3.5 GHz to reduce similarity of the measurements between neighbouring frequencies.

Moreover, reconstructions have been performed in multiple resolutions to examine the benefits of our optimisation strategies. This allowed us to argue that the optimised initial guess can be obtained in low resolution grids, and that this step prior to estimating the true distributions is essential to minimise relative reconstruction errors, especially for reconstruction in high resolutions grids where the number of unknowns increases dramatically. Then we have proposed the L^1 norm regularisation of the TwIST method is based on the Pareto curve, which contributes to de-noising and stabilising the algorithm convergence.

Finally, we have analysed the impact on the reconstruction due to losses in the coupling medium, and the effect of uncertainties in the knowledge of the breast outline and the relaxation constant of the Debye model. This contributes to understanding the sensitivity of the reconstruction algorithm to the uncertainties of the prior knowledge.

Chapter 6

APPLICATION TO DATA FROM A MICROWAVE IMAGING EXPERIMENTAL PROTOTYPE

6.1 Introduction

In this chapter, we focus on the application of the optimized DBIM-TwIST algorithm to data obtained from an MWI prototype. Two types of data are considered: direct measured data from MWI experiments, and numerical data from a CAD model emulating the MWI experiments using CST EM software. An efficient measurement calibration method is introduced to assist the data transformation from 3-D measurement to 2-D reconstruction. The first experimental application stems from collaborative research with Politecnico di Torino, supported by COST TD1301 'MiMed' and by the Microwave Imaging for Combined Early Diagnostics of Breast Cancer (MICENEA) FIRB project. Most of our results, however, are produced by an in-house experimental MWI system, that is currently being developed at King's College. Our new eight-antenna microwave system is based on a small triangular patch printed monopole developed by Syed Ahsan who is in charge of designing antenna, simulating the 3-D CST model, conducting the

realistic experiment and achieving all measurement data [164]. Another colleague, Ziwen Guo contributes to data cleaning and building corresponding 2-D model used by the 2-D FDTD solver.

Our results demonstrate that the algorithm is able to image cylindrical targets immersed in a background (known) medium despite the model errors due to approximating the real experiment with our 2-D FDTD model. Moreover, this study is valuable in analysing sources of error and important aspects of the MWI system design. To gain insight in the impact of the model mismatch between our forward FDTD solver and the true imaging prototype, we have performed 2-D image reconstructions from 3-D CST simulation. The 3-D simulation approaches to the realistic experiment environment, and can therefore verify our antenna system and reconstruction algorithm. Moreover, a frequency selection method based on correlation analysis is proposed to improve the usage of the frequency information. Finally, we examine imaging performance using a two-layer medium in order to enhance signal transmission through the imaging domain but reduce the unwanted multi-signals that cannot be accounted in our simplified 2-D FDTD forward model.

6.2 Measurement Calibration

The experimental data measured by hardware (such as multi-port vector network analysers) generally contains environment noise, thermal noise, antenna mutual coupling and machine noise. For white noise sources, we can apply de-noising techniques after measurement or in the process of reconstruction. For other types of error such as antenna coupling and interference, however, we have to employ a calibration method to reduce the impact in our imaging algorithm, which uses a simplified 2-D solver with point sources as antennas. A simple strategy based on the measurement data is to apply the difference between measurement in inhomogeneous medium (with target) and in

the homogeneous medium (without target). The difference is shown as

$$\begin{aligned} \Delta\Gamma_{dB} &= |E^{inhomo}|_{dB} - |E^{homo}|_{dB} \\ \Delta\Phi &= \Phi(E^{inhomo}) - \Phi(E^{inhomo}). \end{aligned} \tag{6.1}$$

Then the calibrated data can be achieved as

$$\begin{aligned} \Gamma_{E_m} &= |E^{homo}|_{dB} + \Delta\Gamma_{dB} \\ \Phi_{E_m} &= \Phi(E^{homo}) + \Delta\Phi \end{aligned} \tag{6.2}$$

where Γ denotes the magnitude of the received signals in frequency domain, and Φ denotes the corresponding phase. E_{cal}^{homo} is generated by the FDTD forward solver based on the assumed background medium. The corresponding Debye parameters of the background medium are achieved by curving fitting method to data from experimental media measurement to account for frequency dispersion using the Debye model. After that, the calibrated data Γ_{E_m} and Φ_{E_m} will be processed as the input of the reconstruction algorithm.

To analyse the received signals associated with the different transmit antennas, we record the received antennas by relative location ordering, in which the receiver is counted relative to the current transmitter anti-clockwise. The advantage of this receiver ordering scheme is that we can compare signal data (amplitude or phase) at different receivers due to the same transmit antenna in one figure. An example is shown in Fig. 6.4, which is associated with Antenna 1 transmitting in a sixteen-antenna system.

6.3 Application of the DBIM-TwIST to Experimental Microwave Imaging Data

This work presents some results from applying our previously developed MWI algorithm based on the TwIST to data measured from an experimental MWI system. Combining

Figure 6.1: Set-up of the two-antenna experimental MWI system developed in Politecnico di Torino.

the DBIM with the TwIST linear solver, our 2-D algorithm is applied to reconstruct 2-D slices of the complex permittivity of the interrogated imaging domain. Experimental data are obtained by rotating a two-antenna system along the cylindrical imaging domain, which is filled with Triton X-100. The imaging object is an anatomically realistic breast phantom with a tube filled water representing the tumor-like target. Measurements are covered in frequencies ranging from 0.5 GHz to 4.0 GHz.

6.3.1 Experimental Procedure

The mechanical structure of the imaging set-up is shown in Fig. 6.1. To replicate an 16-element tomographic system, a static and robust circular base holds the entire structure. A programmable motor that creates the desirable motion steps is placed above the ground static base of the system. Another circular but movable wooden base is then placed above the motor to hold the cylinder containing immersion liquid to be used as background material. Four vertical wooden columns placed at 45 degrees with respect to each other have been connected with the static base to form the support for antenna

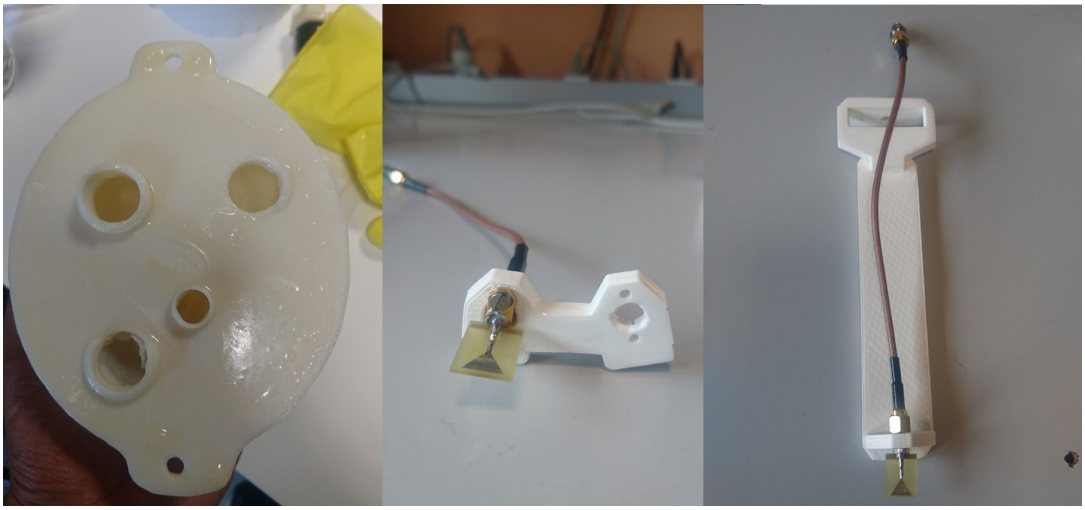

Figure 6.2: From left to right bottom view of Geps-L2S Phantom, the bracket to accommodate 22.5 degree angle between antennas and the vertical support of the antenna with small Inverted Triangular Patch Antenna mounted.

holding structures. 3D printed plastic supports that hold the antennas are connected with the horizontal wooden structures. A small 3D printed connector that attaches with the vertical plastic column connected with the horizontal wooden slider, provides the ability to achieve 22.5 or 45 degree angle between the antennas as shown in Fig. 6.1.

The imaging domain comprises a plastic cylindrical tank surrounded by an Eccosorb MCS absorber which is shielded with the metallic sheet. The purpose of the absorber is to minimize the effect of surface waves propagating along the periphery of the container. There is a strong chance of occurrence of the aforementioned surface wave phenomenon due to the fact that the distance between the antenna and the surface of the container is not large. The Eccosorb MCS is a thin, flexible, magnetically loaded, silicone rubber material that is electrically non-conductive. This product is particularly suitable for cavity resonance reduction applications in the 800 MHZ to 6 GHz range.

Fig. 6.2 depicts that the mechanical fixtures hold the antenna at a steady position and the 3D printed bracket allows for changing the angle between the antennas. The 3D printed phantom base [165, 166] provides several holes to insert a tube as an inhomogeneity (target) into the phantom (by filling the tube with another medium different from the background). The phantom is fully immersed inside a coupling liquid, which was chosen

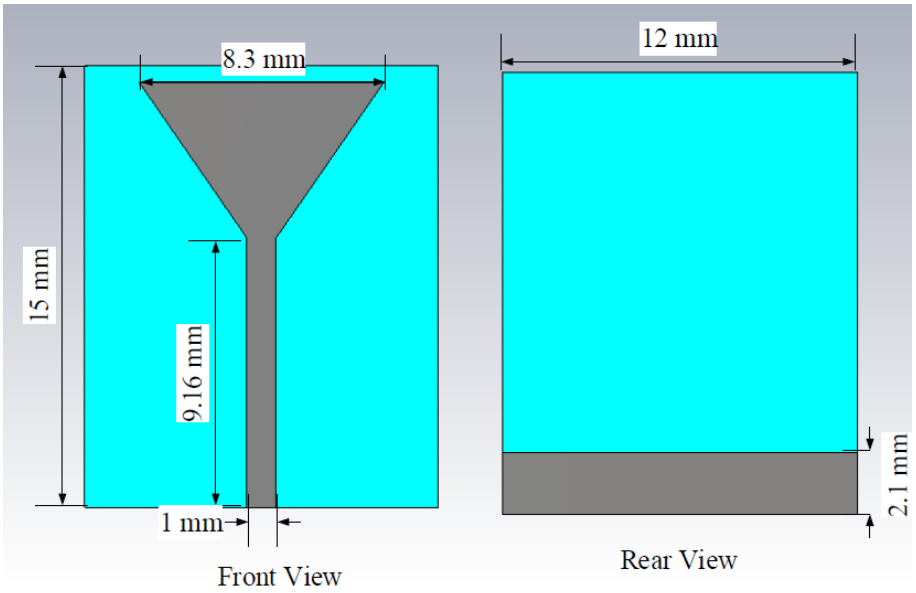

Figure 6.3: The schematic of triangular patch printed monopole antenna. Front and rear view with the geometry and dimensions of the proposed monopole for imaging.

to be Triton X-100 for the present experiment that mimics the dielectric characteristics of the 85—100% adipose tissue content of the normal breast tissue in the considered frequency range [166, 167]. The target comprises a 3D printed cylinder of radius 9 mm filled with pure water. Three cases have been considered for the experimental data: (a) Phantom with target; (b) Phantom without target, and (c) Immersion liquid alone.

Besides, my colleague proposes a compact, robust and simple printed monopole design used in this experiment. The triangular patch printed monopole is presented in Fig. 6.2, which is designed on an FR-4 substrate material. This particular antenna has been designed to operate in a lossy immersion liquid and therefore we have considered the design and optimization of the monopole in sight inside 80% glycerine water solution which has been widely reported in the literature for imaging applications. Fig. 6.3 shows the front and rear view of the proposed antenna modelled in CST microwave studio. The printed monopole under study is constructed of a triangular patch, a transmission line of length 9.16 mm and width 1 mm is used to match the antenna impedance with the 50 ohm coaxial feed. Compared with the traditional monopole, this antenna is smaller in dimension, and can enhance the imaging quality of the MWI tomography.

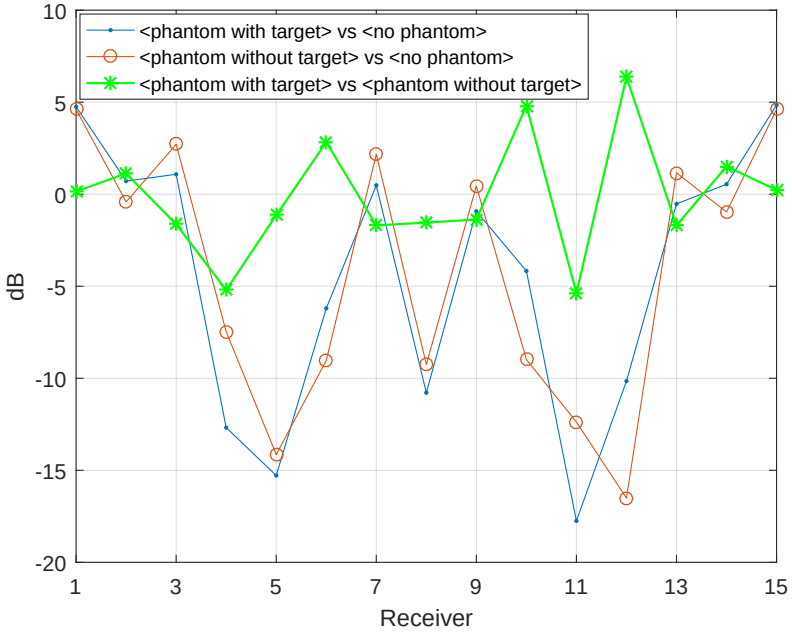

Figure 6.4: Measured amplitudes of the signals scattered from the target and phantom, the phantom alone, and their difference. The data was measured by the receiver at 15 different angles surrounding the phantom evenly, as the transmitter is fixed at the same position.

6.3.2 Experimental Result

An example of the level of signals measured in our experiments in shown in Fig. 6.4, which the signal from the target is quite low relative to the signal from phantom and thus sensitive to measurement noise. Fig. 6.5 presents reconstructed permittivity and conductivity results for a 2-D slice halfway between the bottom of the phantoms and the top of the target. The voxel size for our DBIM-TwIST algorithm was 2 mm, and the algorithm converged after 15 iterations. As the phantom was immersed inside the coupling liquid (Triton X-100 bath with $\epsilon_r = 6.2836$ and $\sigma_s = 0.0950$ at 0.9 GHz), the only scattered signals are from the plastic phantom boundary (which corresponds to a "skin" boundary of unknown thickness) and from the cylindrical target filled with water (with $\epsilon_r = 80.1$ and $\sigma_s = 0.01$ at 0.9 GHz).

In the reconstruction stage, we have included an approximate outline of the phantom with properties of plastic and unknown thickness. Due to the weak signal scattered

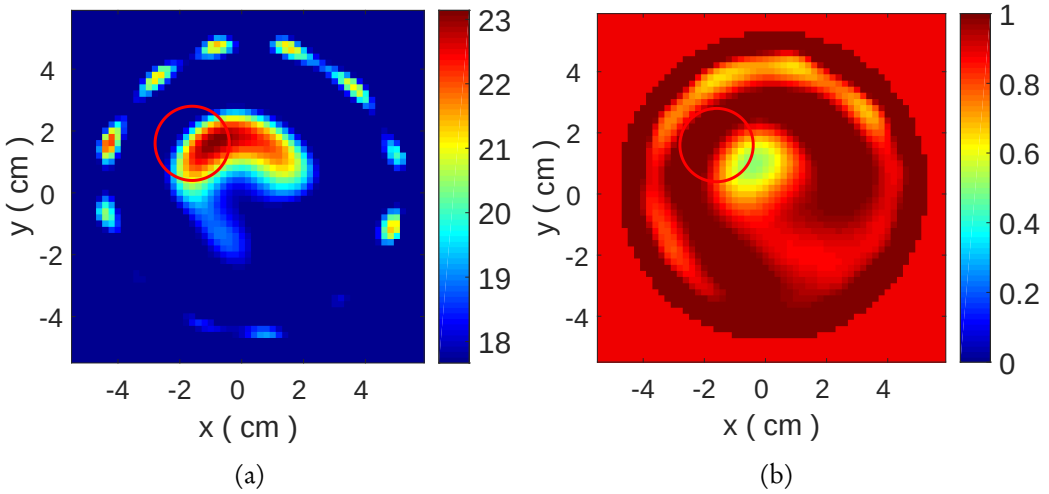

Figure 6.5: Reconstructed images in 2 mm at 0.9 GHz, in condition of unknown skin. (a) image of permittivity; (b) image of conductivity.

from the target relative to the signal caused by (see Fig. 6.4) the plastic boundary, it is challenging to reconstruct the target beyond the plastic boundary in practice. This is evident in Fig. 6.5, where the final reconstructed image manages to detect and localize the target, but underestimates its dielectric constant and overestimates its conductivity value. Moreover, reconstruction errors appear in the areas near the antenna locations.

6.4 2-D Microwave Image Reconstructions from 3-D CST of an In-House MWI Experimental Prototype

6.4.1 Geometry of Eight-antenna System

The CST software is the leading edge tool for the fast and accurate 3-D simulation of high frequency devices in time domain and frequency domain simulation. It can describe the electromagnetic wave propagation in a complex 3-D electromagnetic environment which includes full simulation of a realistic antenna system. In this section, we will reconstruct 2-D images using the simulated measurement data obtained from 3-D electromagnetic wave simulation by the software of 'CST STUDIO SUITE'. In comparison, we also

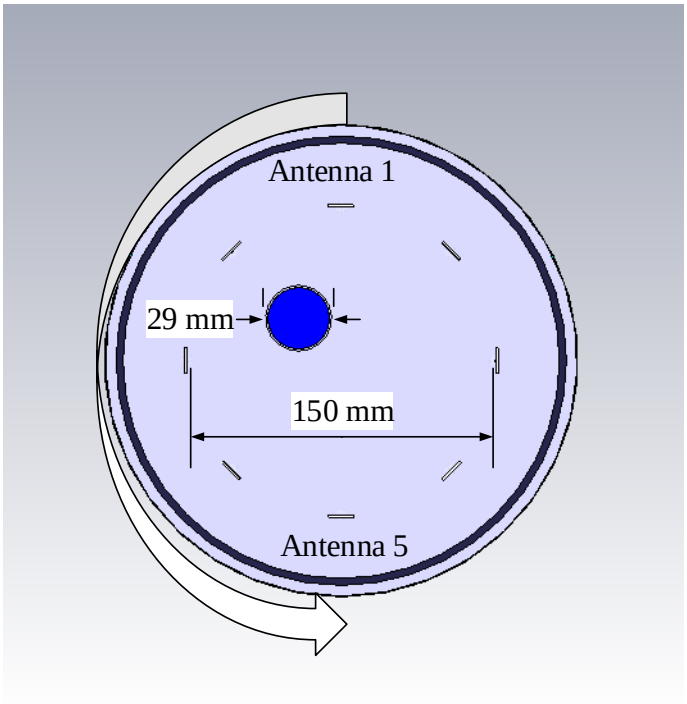

Figure 6.6: Geometry of the eight-antenna system with a simple target in a cylinder filled with pure water.

complete a 2-D inversion based on the same 2-D scalar model by our 2-D FDTD forward solution. To simulate and compare the experimental data in the next section, we consider an eight-antenna microwave system based on the small triangular patch printed monopole introduced in the previous section. The selected antenna is wideband in nature and can operate immersed in different dielectric media, in order to analyse the impact on the robustness of reconstruction associated with various coupling media.

The geometry of the antenna system is depicted in Fig. 6.6. The diameter of the exterior tank is 200 mm and the 8 printed monopole antennas used in the previous section, are positioned in a ring that has a diameter in 150 mm, and in height of 80 mm from the bottom. A thin acrylic glass tube in diameter of 29 mm is placed in the upper right filled with the pure water as a target, close to Antenna 2. The antennas are counted clockwise from y-axis.

In our study, three types of immersion liquids are considered: Trion X-100, 92% corn syrup mixture (with 8% water) and 80% glycerine mixture (with 20% water). The

Table 6.1: Fitted Debye parameters of our simulation materials

Medium	ϵ_∞	$\Delta\epsilon$	σ_s	τ
Triton	3.512	2.582	0.0655	5.3505×10^{-11}
80% Glycerine	4.75	30	0.3779	1.2346×10^{-10}
92% Corn syrup	4.124	12.01	0.3405	1.6667×10^{-10}
Cylinder	3.5	0	0.055	0
Pure Water	78	0	1.59	0

corresponding Debye parameters are acquired by curving fitting method to data from experimental media measurement between 1.0 GHz and 3.0 GHz. The pure water is filled in the inner cylinder as the target. Corresponding fitted Debye parameters are shown in Table 6.1.

In addition, we design the same cross-section model associated with the 3-D model and then obtain 2-D reconstruction from the 2-D FDTD forward simulation, in order to compare the reconstruction performance with the 3-D CST simulation. Our 2-D model considers eight antennas surrounding the 2-D target, representing point sources excited with a wideband Gaussian pulse in a TM configuration, instead of the small triangular patch printed monopole antenna in the same position of the 3-D model. The complete MATLAB codes for 2-D forward FDTD simulation are shown in Appendix A.5.

6.4.2 Reconstruction Results

We have conducted several numerical experiments using the simulated data from 3-D simulation and 2-D FDTD forward solution. Depending on whether the data comes from the 3-D CST or the 2-D FDTD model, we implement a 2-D/2-D or 3-D/2-D reconstruction approach (since our imaging algorithm always uses a 2-D forward solver). The DBIM-TwIST algorithm and frequency hopping approach are employed, in which the reconstruction frequency is assumed from 1.5 GHz to 2.7 GHz. The parameter of the initial guess is assumed as the same as the background medium as *a priori* information.

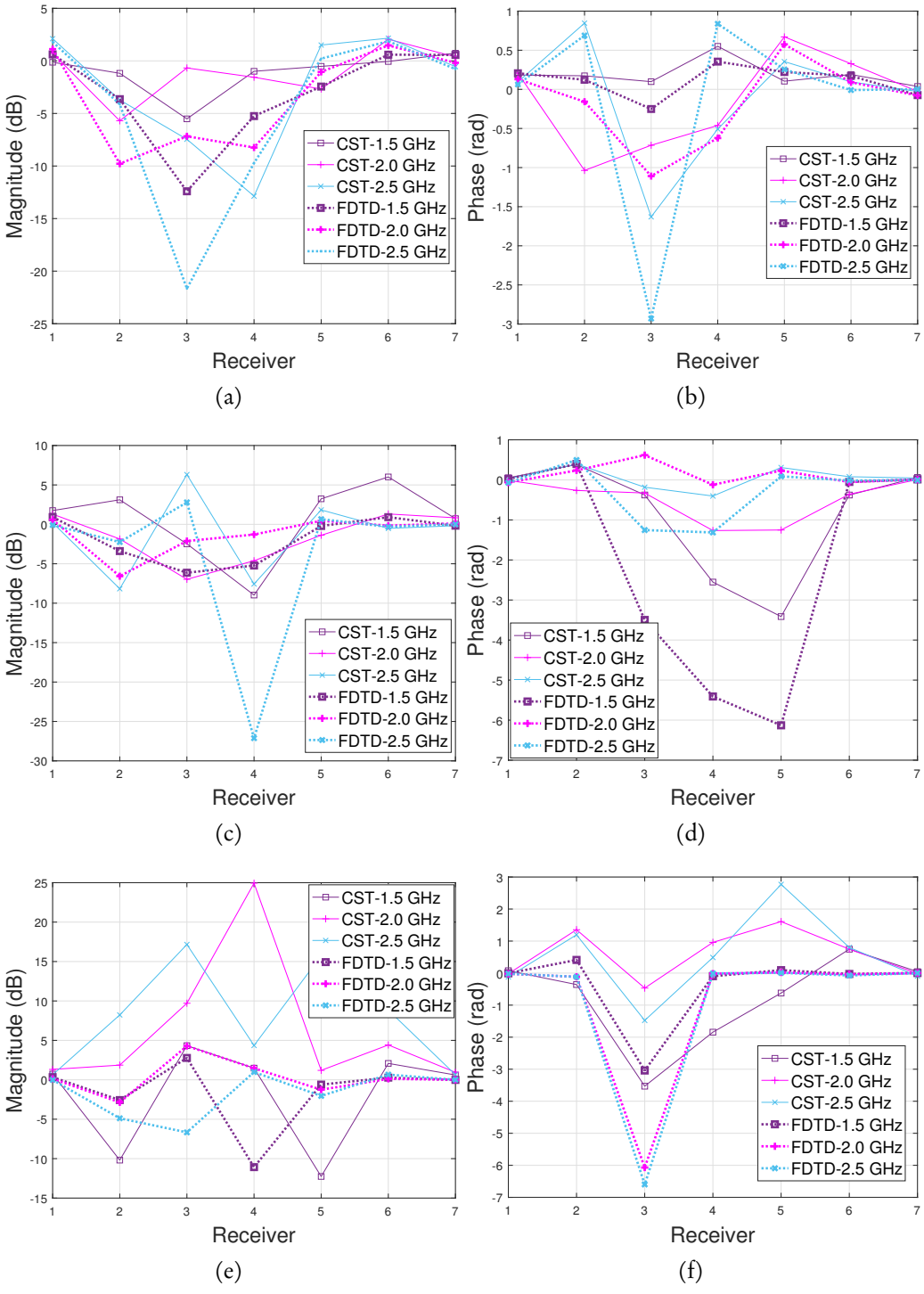

Figure 6.7: Comparison of the measurement differences (with target versus without target) between 3-D and 2-D simulations in condition of the transmitter 1. (a–b) in coupling medium of Triton X-100; (c–d) in coupling medium of 90% corn syrup; (e–f) in coupling medium of 80% Glycerine.

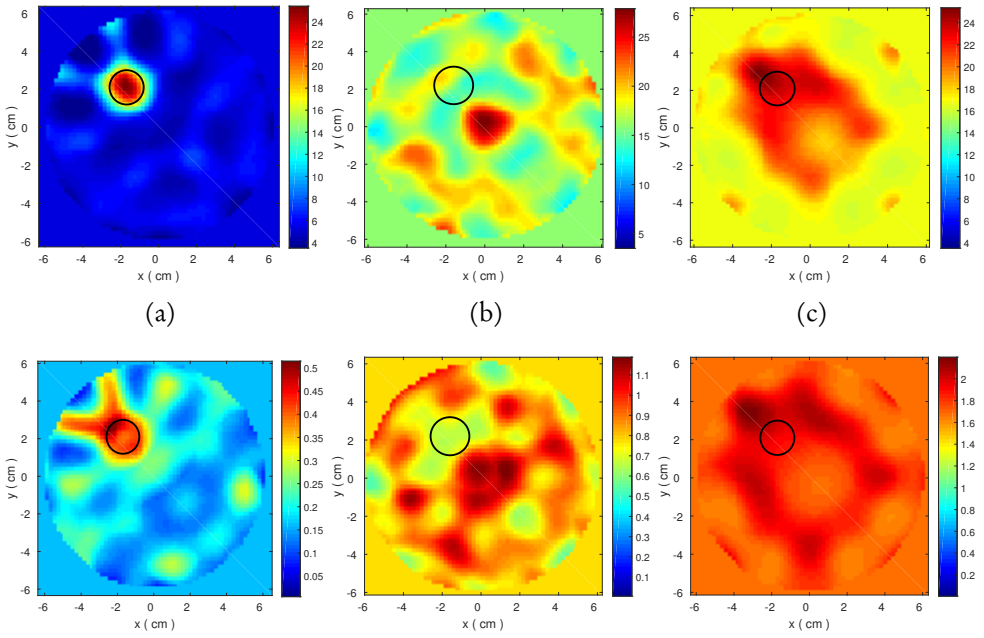

Figure 6.8: 2-D Reconstructed images from 3-D CST simulated measurement for three coupling media. (a–c) the images of ϵ' for Triton, 90% corn syrup and 80% glycerine from left to right; (d–f) the images of corresponding ϵ''.

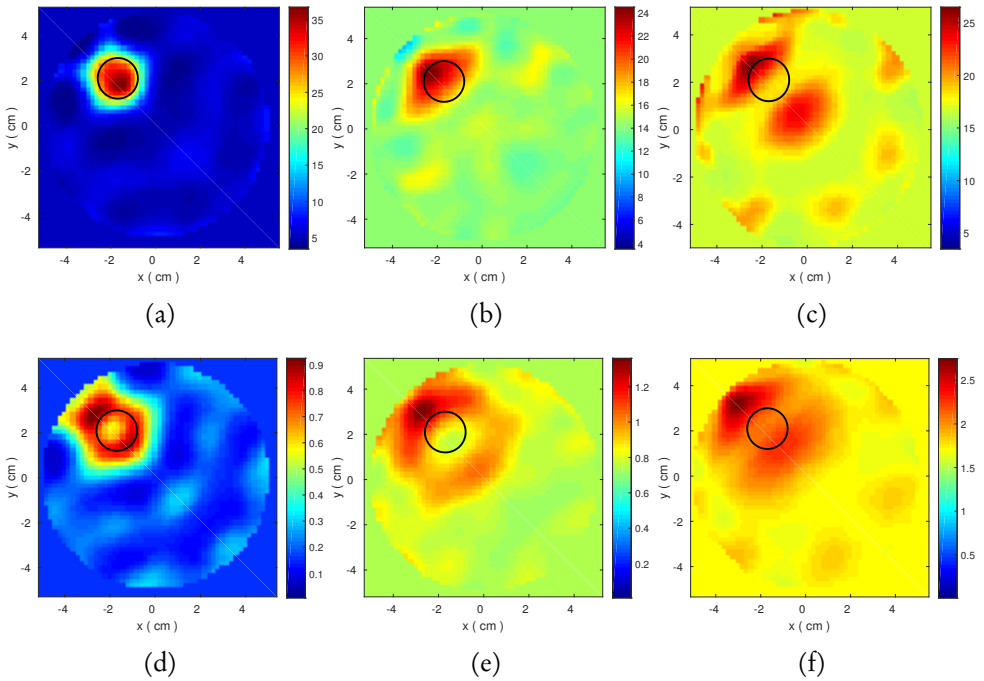

Figure 6.9: 2-D Reconstructed images from 2-D FDTD for three coupling media. (a–c) the images of ϵ' for Triton, 90% corn syrup and 80% glycerine from left to right; (d–f) the images of corresponding ϵ''.

Prior to presenting the reconstructed images, we draw an analogy of the measurement difference (between the simulated measurement data and the background data) between two schemes shown in Fig. 6.7. The sub-figure (a–b) indicate a similar trend between 3-D CST and 2-D FDTD, which suggests that the 2-D FDTD approach with ideal point sources is not far from the true propagation model in this scenario. Further, the inflection point of the v shape pointing at the Receiver 3 suggests a probable location of the target between Antenna 1 (Transmitter) and Antenna 4 (Receiver 3 corresponding to the transmitter). However, we also observe a clear mismatch between two schemes at 2.5 GHz in Fig. 6.7(a) and at 2.0 GHz in Fig. 6.7(b), due to the incident signals scattered by the target and inevitable numerical dispersion in electromagnetic simulation. Besides, we can also observe this mismatch increasing as the losses of the coupling medium increase in (c–f). Especially for 80% glycerine, the magnitude of the measurement tends to unstable in all frequencies, which will affect the convergence of the reconstruction algorithm severely.

The reconstructed images from 3-D CST and 2-D FDTD are shown in Fig. 6.8 and Fig. 6.9 respectively. The ϵ' and ϵ'' are transformed from the Debye distributions in 1.5 GHz. It is clear that good reconstructed images can be achieved both cases for Triton X-100 which is the least lossy medium from the three.Image reconstruction for the other two media is much worse in both CTS and FDTD cases, is correlated to inconsistencies in the transmitted signals for the cases of corn syrup and glycerine in Fig. 6.7. An interesting result is obtained in Fig. 6.8 is that the reconstructed results in the corn syrup are worse than in the 80% glycerine, in spite of the fact that the latter is a more lossy medium.This motivates a need to perform efficient frequency selection by evaluating the measured data. To tackle this problem, we will propose a frequency selection method based on correlation analysis, and the optimised result will be presented in the next section.

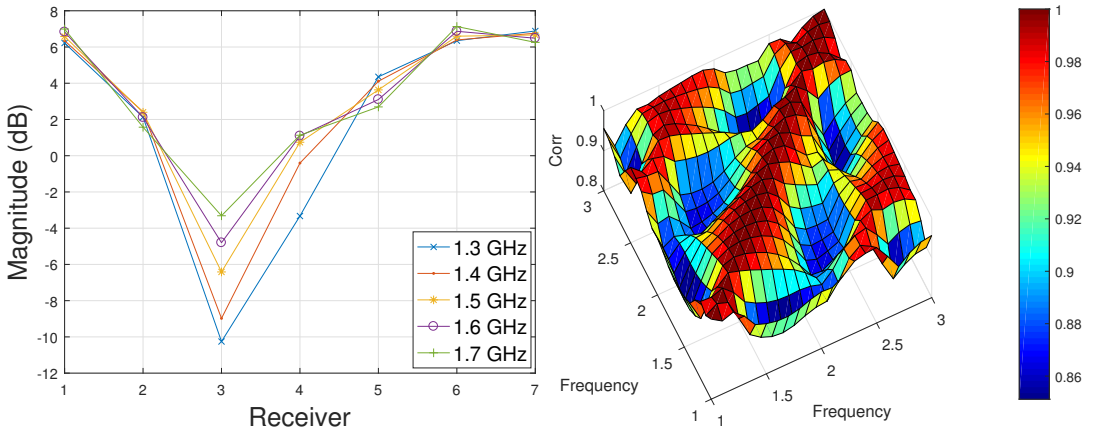

(a) (b)

Figure 6.10: (a) An ideal representation of relative measurement in low frequencies for Triton. (b) Corresponding cross-correlation map between 1.0 GHz and 3.0 GHz for Transmitter 1.

6.5 A Frequency Selection Method Based on Correlation Analysis

In a real MWI experiment, inconsistencies and errors in the received signals at different frequencies can be due to many factors, including outside interference as well as the antenna operation characteristics , which makes it is impossible to obtain a completely smooth measurement in the wideband between 1.0 GHz and 3.0 GHz. By applying the calibration method introduced in Section 6.2, we can acquire an observable trend of the relative measured magnitude and phase between adjacent frequencies in a certain sub-bands. Prof. Meaney has illustrated related research in [168], where magnitude and phase have a gradual change along with frequency change. Thus, we consider categorising the adjacent frequencies with similar trends into a group as high correlation group and the rest into moderate and low correlation group.

Considered two variables X and Y, Pearson's correlation coefficient is defined as ,

$$\rho(X,Y) = \frac{cov(X,Y)}{\sigma_X \sigma_Y} \tag{6.3}$$

where cov is the covariance, and σ_X and σ_Y denote the standard deviation of X and Y respectively. In this section, assuming an N-antenna system, we define 21 variables $F_1^n, F_2^n, \ldots, F_{21}^n$ representing the received information for the n_{th} transmitter in frequencies from 1.0 to 3.0 GHz. Every variable F_i includes $N-1$ elements of magnitude of the received signals, described as

$$F_i = [R_{(i,1)}, R_{(i,2)}, \ldots, R_{(i,N-1)}]^T. \tag{6.4}$$

Thus, we can obtain the correlation coefficient matrix $\boldsymbol{P}^n$ for the n_{th} transmitter described as,

$$\boldsymbol{P}^n = \begin{bmatrix} \rho(F_1,F_1) & \rho(F_1,F_2) & \ldots & \rho(F_1,F_{21}) \\ \rho(F_2,F_1) & \rho(F_2,F_2) & \ldots & \rho(F_2,F_{21}) \\ \vdots & \vdots & \vdots & \vdots \\ \rho(F_{21},F_1) & \rho(F_{21},F_2) & \ldots & \rho(F_{21},F_{21}) \end{bmatrix} \tag{6.5}$$

and then the final cross-correlation matrix is the average of correlation coefficient P^n for all transmitters shown as,

$$\bar{\boldsymbol{P}} = \frac{1}{21}\sum_{n=1}^{21} \boldsymbol{P}^n \tag{6.6}$$

An ideal representation of correlated measurement with similar trends in low frequencies is demonstrated in Fig. 6.10(a), using the 2-D forward FDTD based on the eight-antenna system introduced in Section 6.4. The model including a single object submerged in Triton X-100 can generate smooth measurement due to low losses. The cross-correlation map is shown in Fig. 6.10(b). It is clear that the red areas mainly cover two sub-bands, in which one group is below 2 GHz and the other group is above 2.5 GHz. Finally, by repeating this for all transmitters, we can achieve the mean of cross-correlation distributions in the whole frequency range.

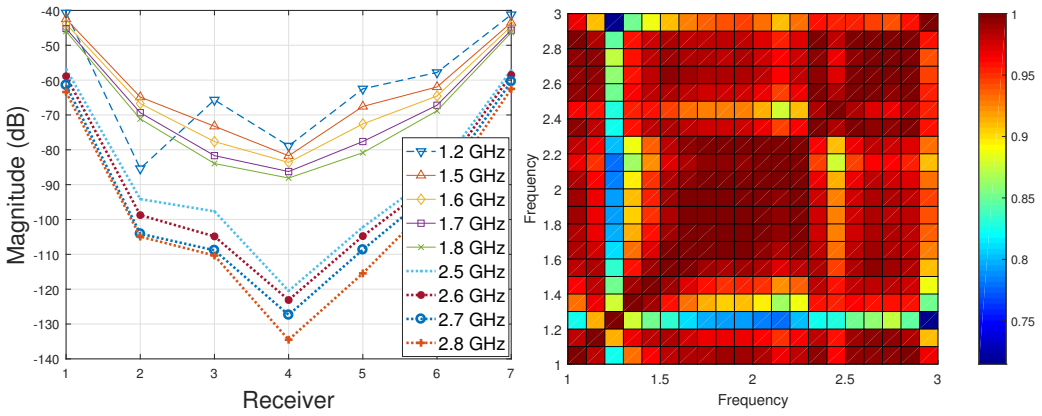

(a) (b)

Figure 6.11: (a) A representation of correlated measurement in two sub-bands from 3-D CST in 90% corn syrup. (b) Corresponding cross-correlation map between 1.0 GHz and 3.0 GHz in an average of all transmitters.

Note that the high correlation measurement cannot guarantee a good reconstruction in related frequencies. Conversely, the low cross-correlation frequencies may also contain useful information used in frequency hopping approach. Thus, the correlation analysis just provides a perspective to verify the validity of the measurement in various frequencies.

Besides, the low correlation information may suggest that there are some measurement errors at certain non-consecutive frequencies, which suggests excluding these unnecessary frequencies in the reconstruction process. Thus, we can substitute the relative measurement with the absolute measurement (the measurement with target) to apply correlation analysis. The absolute measurement denotes the experimental or CST measurement with target (pure water in the tube), which generally exist higher cross-correlation in frequencies because the measurement noise is far smaller than the power of the incident signals. Thus, an abnormal measurement at a certain frequency will be highlighted in the cross-correlation map.

To present the effect of the frequency selection method based on the absolute measurement, we employ the simulated measurement from 3-D CST simulation that sets 90% corn syrup as the coupling medium, and the model introduced in Section 6.4. The measured data and the corresponding cross-correlation map have been shown in Fig. 6.11.

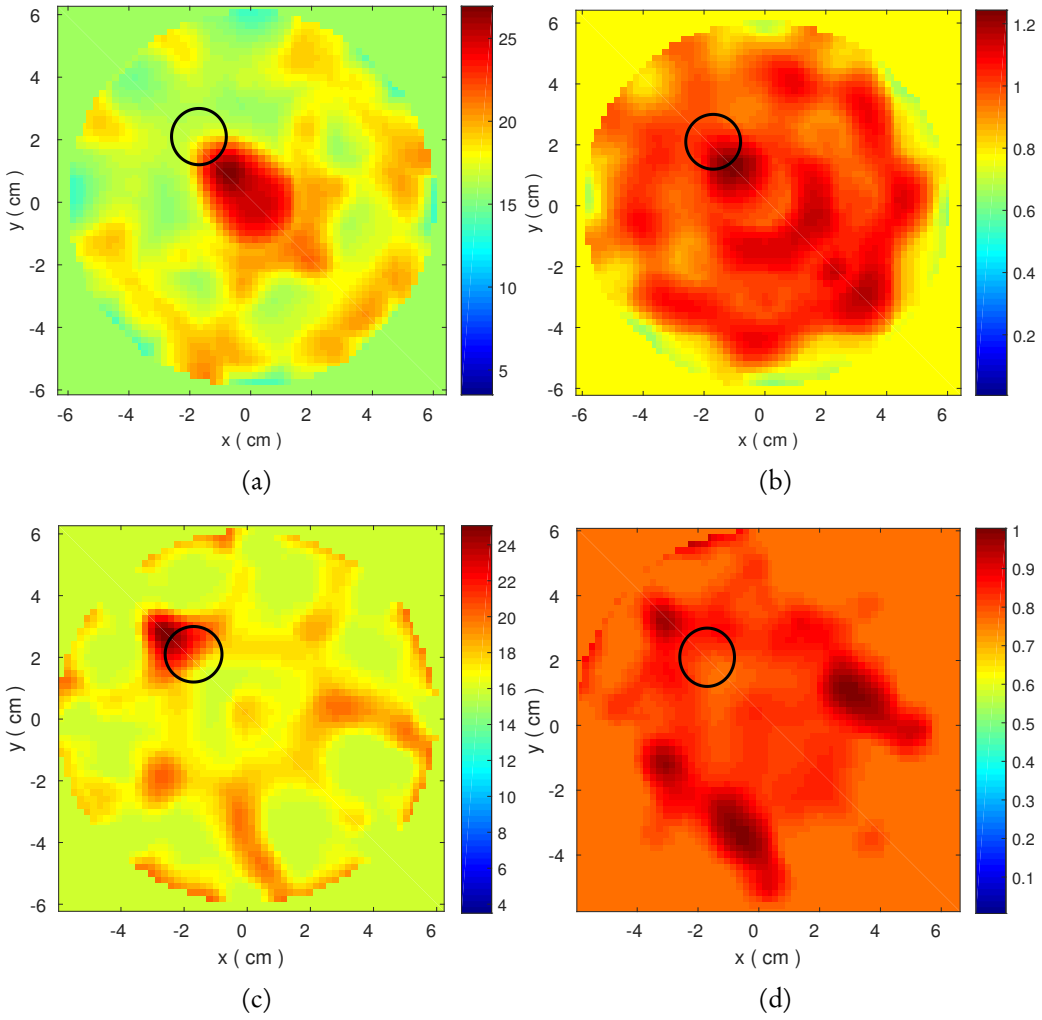

Figure 6.12: Reconstructed images based on the low-frequency and high-frequency group respectively. (a–b) the images of ϵ' (left) and ϵ'' (right) reconstructed by the frequency hopping approach from 1.5 to 1.8 GHz; (c–d) the images of ϵ' (left) and ϵ'' (right) reconstructed by the frequency hopping approach from 2.5 to 2.8 GHz.

It is easy in Fig. 6.11(b) to find a "blue belt" at 1.2 GHz which denotes a low correlation against all other frequencies. The corresponding plot is depicted in Fig. 6.11(a), where the received signals at 1.2 GHz is not similar to any other lines. As discussed above, it possibly suggests the received signal at 1.2 GHz belongs to measurement error or environment error which is much stronger than the power of the incident signals. Thus, the frequency at 1.2 GHz will be removed in the process of image reconstruction. Except the abnormal frequency, the cross-correlation map suggests two sub-bands as the representatives of the low and high frequency group. The reconstructed images are shown in Fig. 6.12 by low frequency group (1.5, 1.6, 1.7, and 1.8 GHz) and high-frequency group (2.5, 2.6, 2.7, and 2.8 GHz). Compared with the results in Fig. 6.9 (b) and (e), the distinct improvement is observed from Fig. 6.12 (c) and (d).

Conversely, low-frequency information cannot provide a reliable reconstruction in this case. As the long wavelengths in these frequencies can only locate a large target and the outline of the target.

In the end, it is concluded that we propose a novel analysis tool to choose the reconstruction frequency and examine the reliability of the measurement. The frequency selection method does not tend to optimize the reconstruction result from any of the relative or absolute measurement, but provides a new interpretation of the received signals at different frequencies. The distribution of the cross-correlation coefficients represents a category of similarity of the measurement in several sub-bands. We can not only take advantage of the characteristic in every sub-band to achieve an optimal reconstruction images by frequency hopping approach, but also avoid the measurement error at a certain frequency. In the next section, our frequency-selection method will process the real experimental measurement data and provide an optimal set of frequencies used for reconstruction.

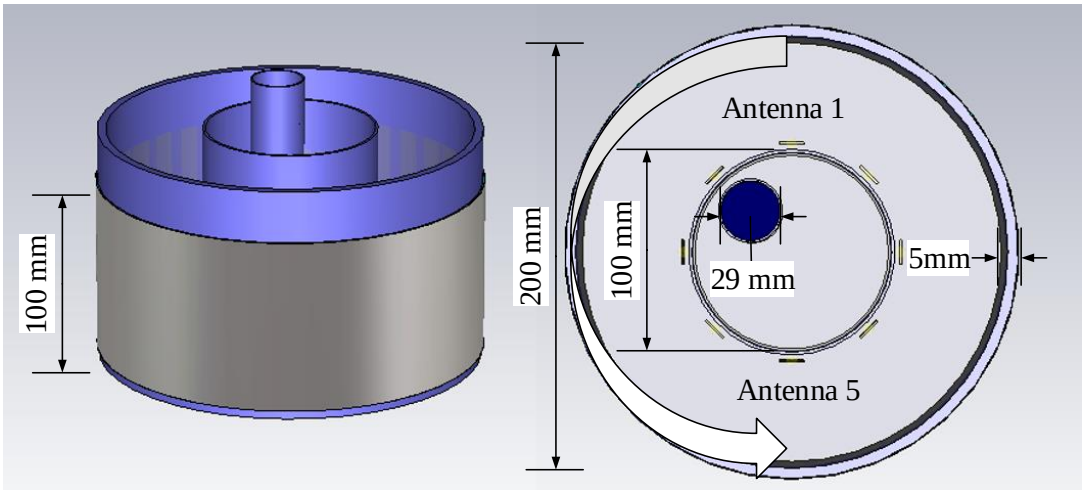

Figure 6.13: The geometry of improved eight-antenna system based on a two-layer medium.

6.6 Application to An Experimental MWI System with a Two-layer Medium

6.6.1 Introduction of Experiment System Geometry

In the previous section we considered different dielectric background media and deduced that higher loss of immersion medium is vital to minimize the cross coupling between array elements, however the hardware requirement for collecting these low signal levels is completely altered when we use high loss medium as background. Therefore, there is a need of high sensitivity transceivers to collect the information which incurs higher cost to the system. Also, from the practical point of view, considering the actual breast anatomy, we can confidently assume that the EM signal will not have to traverse in the background medium across the entire array diameter. Hence, we introduce another layer in the imaging domain by placing two different-size tanks where background immersion is filled between two tanks and another low loss medium is filled in the interior tank that mimics low loss fatty tissues inside the breast. The small tube filled with the pure water is placed in the interior tank as a target.

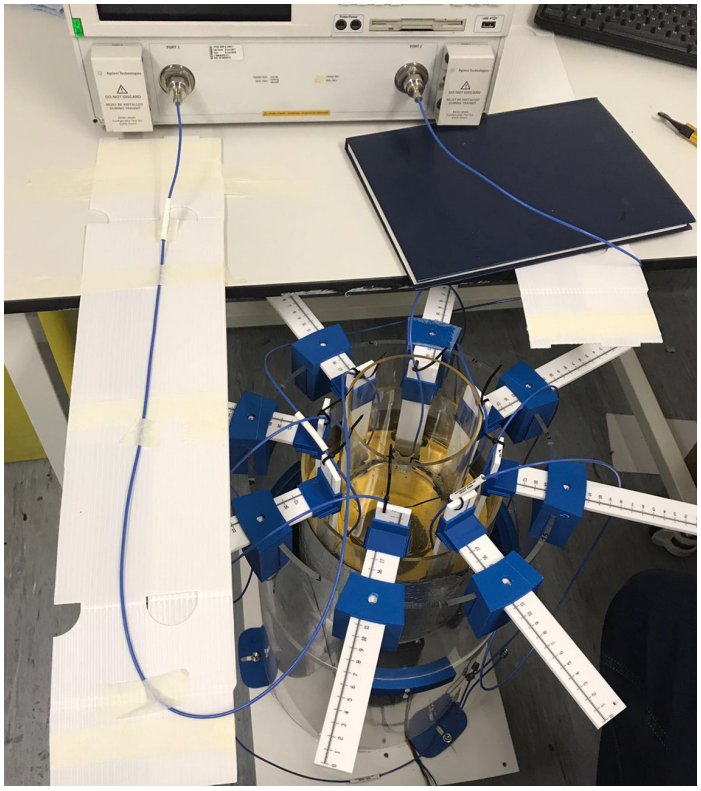

Figure 6.14: Photo of our experimental MWI system

We propose an improved antenna system based on the two-layer medium shown in Fig. 6.13. The exterior tank in diameter of 200 mm is wrapped by the absorber layer. An extra interior tank in diameter of 100 mm is placed in the centre inside, which is surrounded by 8 triangular patch printed monopole antennas with a diameter of 130 mm. All antennas are submerged into the outer medium between two tanks, close to the interior tank by 15 mm. Safflower oil as the inner medium is filled in the interior tank with a cylinder in 29 mm as a target of the pure water. To analyse the performance of the improved system, 80% glycerine and 90% corn syrup are chosen as the outer medium in comparison. According to the previous introduction, the radiation performances of the antenna immersed two types of the media have been verified by the CST simulation and the realistic experiment. In the next section, reconstruction results based on these two media will be presented.

The data acquisition mechanical structure for collection of the imaging data has to be accurate and robust in order to collect data that minimizes errors. The data acquisition process is very prone to errors and therefore the mechanical set-up has to be designed very carefully so that the potential errors are minimized. The sources of errors range from the physical position of the antennas to the method of acquiring the mono-static data. We have considered a cylindrical geometry for our set-up which provides a symmetry on horizontal and vertical axes. The mechanical structure shown in Fig. 6.14.

The horizontal and vertical position of the antennas are controlled manually by using the calibrated supports which allow us to easily and precisely adjust the position of antennas forming the array. And we still use the printed monopole antenna mentioned in 6.3.1. A circular disc having holes of different diameters at four different locations has been 3D printed to situate the target holding acrylic tube, which allows precise control of target location inside the imaging domain. Moreover, the phenomenon of surface waves and multipath signal propagation has also been considered in our design and in order to curb the interfering signals and surface waves we have introduced an absorber layer with metallic coating along the exterior of the tank holding the dielectric medium. The mechanical system also requires a smooth and robust base so that the whole system remains stationary throughout the data collection.

6.6.2 2-D Image Reconstruction based on DBIM-TwIST Method

In this section, the DBIM-TwIST method and frequency hopping approach are applied to reconstruct 2-D images in specific frequencies selected by the frequency selection method. To analyse the impact of the outer medium's loss, two different outer media will be compared in the eight-antenna system with a two-layer medium, including the 90% corn syrup and 90% corn syrup. The safflower is used for two cases as the interior medium.

Fig. 6.15 (a–b) demonstrate two cross-correlation maps regarding the relative measurement (the difference of experiment measurement between with target and without

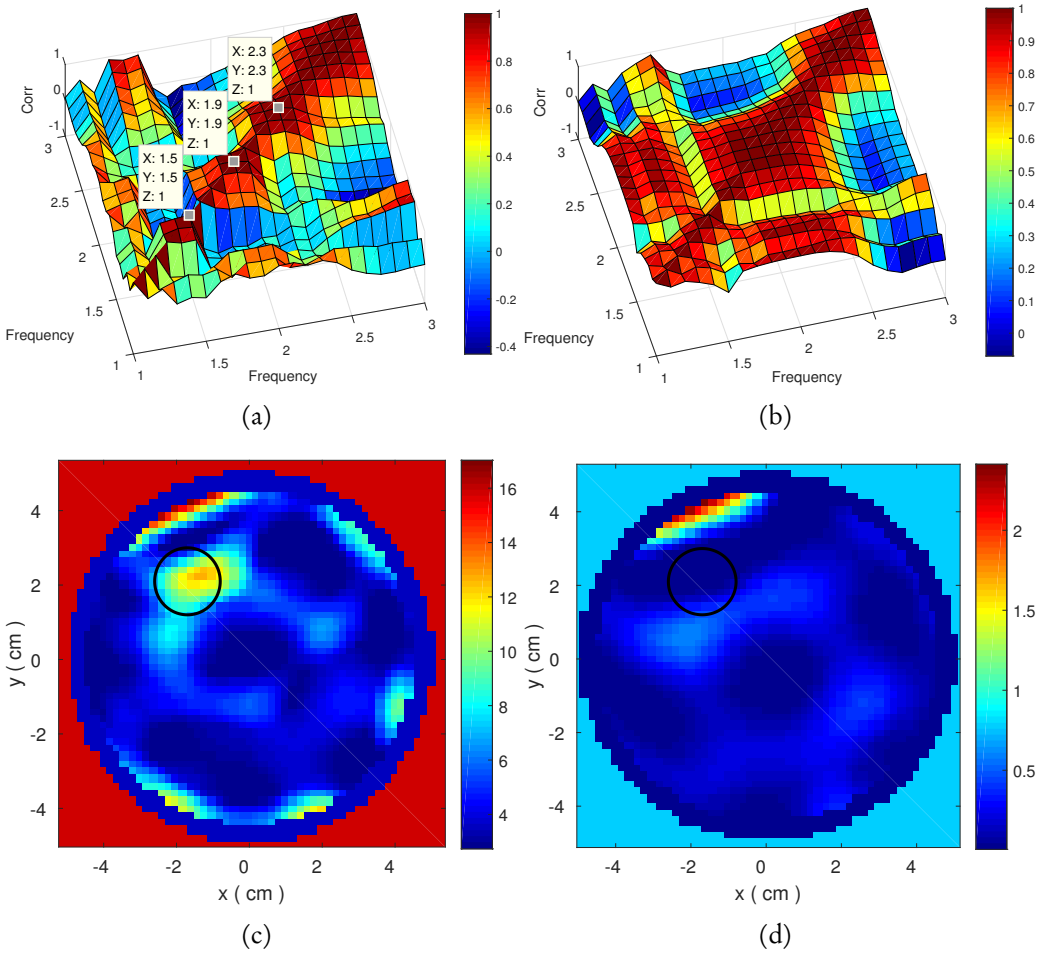

Figure 6.15: Cross-correlation maps based on 90% corn syrup(outer medium) and safflower(inner medium). (a) Cross-correlation map based on the relative measurement (b) Cross-correlation map based on the absolute measurement. Reconstructed images of ϵ' in (c) and ϵ'' in (d) by frequency hopping approach at 1.5, 1.9, and 2.3 GHz in Case 1.

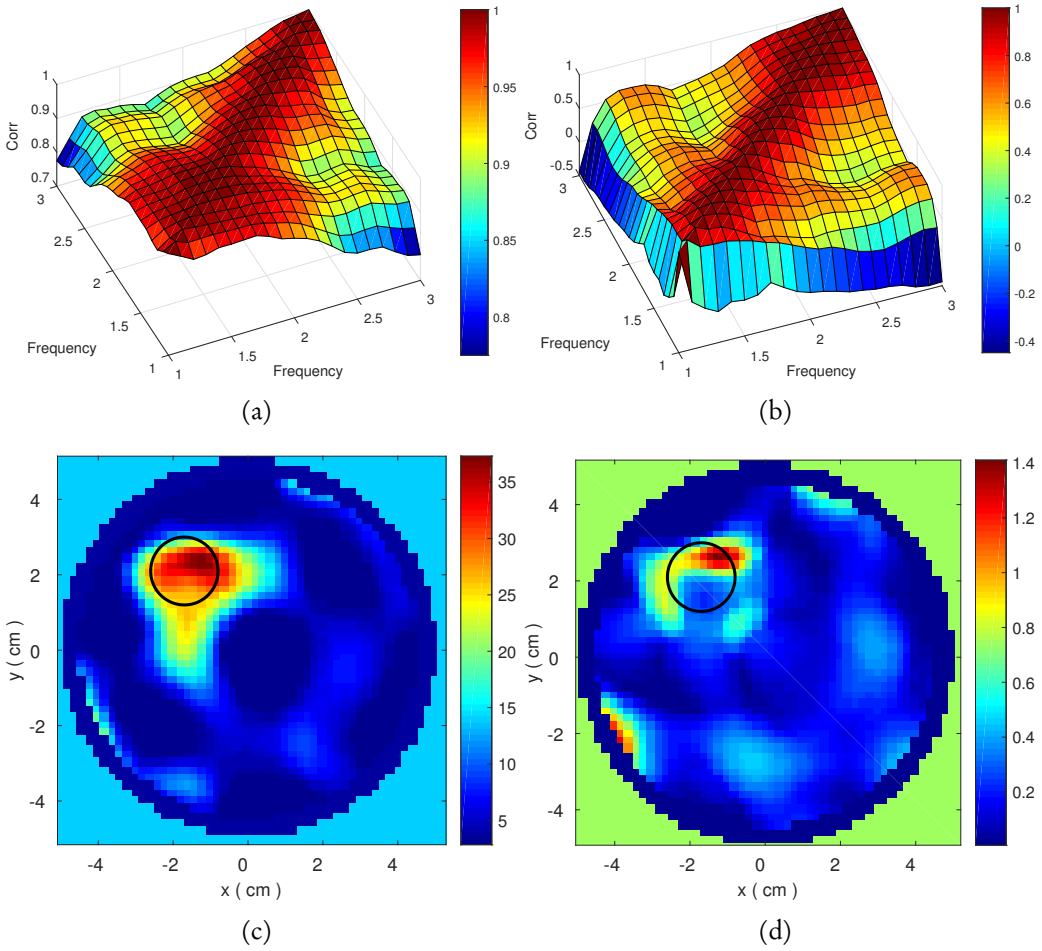

Figure 6.16: Cross-correlation maps based on 80% glycerine(outer medium) and safflower(inner medium). (a) Cross-correlation map based on the relative measurement (b) Cross-correlation map based on the absolute measurement. Reconstructed images of ϵ' in (c) and ϵ'' in (d) by frequency hopping approach in 1.5, 1.6, and 1.7 GHz in Case 2.

target) and the absolute measurement (the measurement with target). It is clear that there are four areas with high-correlation coefficient around 1.5, 1.9, and 2.3 GHz. The reconstructed images are shown in Fig. 6.15. The image of ϵ' is better than ϵ''. A part of reason is that the pure water as the target provides high contrast of ϵ_∞ in the Debye model but the $\Delta\epsilon$ is set to zero. The Debye model combining with the non-dispersive model causes an inevitable bias of the Debye parameter estimate starting from the initial guess, as well as in terms of setting of hard constraints.

In comparison, two smoother cross-correlation maps regarding the relative and absolute measurement in Case 2 are presented in Fig. 6.16 (a) and (b). Due to the high dispersion from 80% glycerine, exterior environment noise and the interfering signals are reduced heavily to obtain evener signals. It leads to better reconstructed results and steady convergence shown in Fig. 6.16. It is clear that the target is located precisely in ϵ', and ϵ'' performs much better than the results in Case 1 of Fig. 6.15. Besides, using the same number of iterations in two cases, the dielectric value of ϵ' and ϵ'' based on the glycerine is closer to the real value of the pure water than that in 90% corn syrup. Thus, it is concluded that we propose a complete new microwave antenna system based on the two-layer medium, in which the exterior medium is immersed by antennas, and contributes to reduction of interfering signals and environment noise. The interior medium with low dispersion enhances the signal radiation inside. Reconstructed images for two types of the exterior media suggests that the high loss exterior medium contributes to smooth measurements compared with the low loss material. Using the frequency selection method and frequency hopping approach, we demonstrate a distinct improvement of the reconstructed images in comparison to a single-medium system.

6.7 Conclusion

In this chapter, we focus on the application of our DBIM-TwIST algorithm to our experimental antenna system. The collaborative research with Politecnico di Torino gave

us an initial experience to process the experimental data relating to Triton X-100 in their two-antenna system. Then the 3-D CST simulations provide a series of comparisons regarding radiation performances using different background media and corresponding reconstruction performances in the eight-antenna system. These work finally contribute to the implementation of the enhanced-scatter MWI system based on the two-layer medium. The reconstructed images suggest that the use of safflower as a low loss material improves the quality of the measured data, enabling our algorithm to perform well, in combination with the frequency selection approach presented in the chapter.

Chapter 7

CONCLUSIONS and FUTURE WORK

7.1 Summary of Contributions

In this thesis, the overriding purpose of this study is to reconstruct the complex permittivity of 2-D anatomically realistic numerical breast phantoms and experimental measurements. We implemented a complete 2-D microwave breast imaging technique based on the DBIM-TwIST algorithm, and also proposed a series of MWI optimization strategies to improve robustness of the TwIST algorithm, and to enhance quality of multiple-frequency reconstructions in multiple resolutions by optimizing initial guess, the L^1 norm regularization method, and the novel frequency selection method. The main contributions in this thesis are as follows.

- This study proposed the adaptive TwIST method to solve the linear problem and optimized the algorithm's parameters for MWI for the first time. Compared with CGLS and LSQR, the adaptive TwIST method enhanced the flexibility and robustness of the MWI reconstruction.

- A new way of combining multiple frequency information is proposed to improve further the performance of the DBIM-TwIST algorithm for microwave breast imaging. And a series of the FDTD improvement strategies increased the computational efficiency of the forward FDTD solver based on a resolution adjustment.

- A novel two-step DBIM algorithm is proposed to optimize the initial guess of the DBIM, where the first step estimates the average breast properties with low computational cost. The optimal initial guess avoided false solutions and converged the algorithm to an optimal solution. The reconstruction quality for different breast phantoms are enhanced in various resolutions.

- A novel regularization technique based on the Pareto curve and L^1 norm regularization is proposed for the first time in MWI, which improved convergence stability of the TwIST algorithm. We improved the differentiability and continuity of the TwIST algorithm's convergence by employing curve fitting method of cubic polynomials to smooth the Pareto curve. And the computation cost is reduced by applying an exponential distribution sampling of the regularization parameter.

- The proposed MWI algorithm is assessed for realistic experiments with a unique approach, using a three-dimensional (3-D) CAD model first to assess model error without additional random experimental errors such as interference, before moving to data from the true experimental system. The impact of the model mismatch between the forward FDTD solver and the true imaging prototype is analysed to ensure the reliability of the reconstruction from the experimental measurement.

- Impact of frequency selection in reconstructions from experimental data is systematically studied for the first time using cross-correlation metrics that are applied to the experimental data directly. Two approaches of the frequency selection method based on the relative measurement and absolute measurement improved

the efficiency of selecting frequency used in the DBIM reconstruction by removing the measurement error.

Moreover, we focused on developing a complete software system for MWI in MATLAB, supporting 2-D image reconstruction in multiple resolutions from numerical breast phantoms, 3-D CST, and experimental measurement. The reconstruction system integrated the DBIM with frequency hopping, multiple frequency and hybrid frequency approaches. The proposed regularization method and initial guess optimization method are integrated in the DBIM-TwIST algorithm as an optional optimization method respectively.

Besides, an application interface of generic self-defined modelling tool is developed to support self-define 2-D FDTD model. A data-connected tool is developed to process rare S-parameter measurement data from 3-D CST simulation and experimental measurement.

Finally, the FDTD computation efficiency is optimized by parallel computing technique and GPU computing technique. The FDTD computation time reduces by 90% from 9 second per DBIM iteration to 0.8 second, based on i7-6700HQ CPU working at 2.6 GHz with 16 GB memory.

7.2 Future Work

Acceleration of Electromagnetic Simulation

In this thesis, the FDTD with CPML is employed to simulate the propagation of EM wave. Considering that the FDTD computation cost accounts for 90% in total, we can optimize the FDTD computation by parallel GPU computing to distribute the propagation simulations from different transmitters into multiple parallel GPUs. Besides, for the large-scale model, we can apply finite element method (FEM) combined with the FDTD to reduce the computation cost. The FEM and the FDTD are applied for outside of the reconstruction domain and inside of the reconstruction domain respectively.

Moreover, the multiple-grid technique of the FDTD can be employed to enhance the reconstruction quality in a specific reconstruction area.

Optimization of the DBIM

The DBIM is used for transforming the non-linear problem to linear problem by approximating the Green function G^b and electric field E^b. That can be optimized by obtaining the higher precision approximation by modifying the DBIM. The challenge is how to guarantee a stationary iterative convergence of the modified DBIM.

On the other hand, another important research is how to optimize the number of the DBIM iterations. In this study, the iteration number is set as 15 or 10 iterations per frequency. However, as one distinct advantage of the MWI is that the permittivity as well as the conductivity of the human tissues including tumours can be reconstructed as an extra measure compared with traditional imaging methods. The total number of the DBIM iteration must be optimized to obtain the best estimate of the dielectric values. This challenge is not only how to terminate the DBIM iterations, but also how to reconstruct the real human tissue properties without *a priori* information relating to the human interior properties. To this end, that is the reason why the current study just can localize the tumour in high contrast.

Moreover, this study has proposed a novel two-step method to optimize the initial guess. In the future research, we can optimize the sampling method to find the optimal initial guess. For example, a progressive sampling in multiple steps can be designed to reduce the number of sampling. In the first step, we can obtain N samplings between lower bound and upper bound of the initial guesses. Following by finding an optimal solution, we then obtain new N samplings around the optimal initial guess in the first step and then to find the final optimal initial guess. This strategy provides N^2 precision to estimate the optimal initial guess but just doubles the computation cost.

Further Development of Experimental System with Two-Layer Medium

In the last chapter, our latest experimental system with two-layer medium presents a great improvement in enhancing the scattered signal and reducing reflection and multi-path signals. The future work can keep optimizing this system by trying different combinations of the interior and outer media. Moreover, the impact of the antenna's position (including distance to tank, distance to bottom of tank) will be discovered.

In addition, the maximum number of antennas applied in the experimental system should be discussed. On the one hand, we should analyse the limit of the number of antennas in the reconstruction process using the multiple frequency approach, considering the computation capacity in the TwIST. On the other hand, we can design a rotatable antenna array to reduce the number of the realistic antenna which leads to reduction of cross-coupling signals. Finally, the quality of the MWI can be enhanced by amplifying the scattered signals.

References

[1] P. T. Huynh, A. M. Jarolimek, and S. Daye, "The false-negative mammogram," *Radiographics*, vol. 18, no. 5, pp. 1137–1154, 1998.

[2] U. P. S. T. Force *et al.*, "Screening for breast cancer: Us preventive services task force recommendation statement," *Annals of internal medicine*, vol. 151, no. 10, p. 716, 2009.

[3] S. P. Poplack, T. D. Tosteson, W. A. Wells, B. W. Pogue, P. M. Meaney, A. Hartov, C. A. Kogel, S. K. Soho, J. J. Gibson, and K. D. Paulsen, "Electromagnetic breast imaging: results of a pilot study in women with abnormal mammograms," *Radiology*, vol. 243, no. 2, pp. 350–359, 2007.

[4] L. Sha, E. R. Ward, and B. Stroy, "A review of dielectric properties of normal and malignant breast tissue," in *SoutheastCon, 2002. Proceedings IEEE*, 2002, pp. 457–462.

[5] P. M. Meaney, M. W. Fanning, D. Li, S. P. Poplack, and K. D. Paulsen, "A clinical prototype for active microwave imaging of the breast," *IEEE Transactions on Microwave Theory and Techniques*, vol. 48, no. 11, pp. 1841–1853, 2000.

[6] P. M. Meaney, A. P. Gregory, N. R. Epstein, and K. D. Paulsen, "Microwave open-ended coaxial dielectric probe: interpretation of the sensing volume re-visited," *BMC medical physics*, vol. 14, no. 1, p. 3, 2014.

[7] A. Rosen, M. A. Stuchly, and A. Vander Vorst, "Applications of rf/microwaves in medicine," *IEEE Transactions on Microwave Theory and Techniques*, vol. 50, no. 3, pp. 963–974, 2002.

[8] X. Li, S. K. Davis, S. C. Hagness, D. W. Van der Weide, and B. D. Van Veen, "Microwave imaging via space-time beamforming: Experimental investigation of tumor detection in multilayer breast phantoms," *IEEE Transactions on Microwave Theory and techniques*, vol. 52, no. 8, pp. 1856–1865, 2004.

[9] X. Li, E. J. Bond, B. D. Van Veen, and S. C. Hagness, "An overview of ultra-wideband microwave imaging via space-time beamforming for early-stage breast-cancer detection," *IEEE Antennas and Propagation Magazine*, vol. 47, no. 1, pp. 19–34, 2005.

[10] E. J. Bond, X. Li, S. C. Hagness, and B. D. Van Veen, "Microwave imaging via space-time beamforming for early detection of breast cancer," *IEEE Transactions on Antennas and Propagation*, vol. 51, no. 8, pp. 1690–1705, 2003.

[11] J. Bourqui, M. A. Campbell, J. Sill, M. Shenouda, and E. C. Fear, "Antenna performance for ultra-wideband microwave imaging," in *Radio and Wireless Symposium, 2009. RWS'09. IEEE*, 2009, pp. 522–525.

[12] E. Fear and M. Stuchly, "Microwave detection of breast cancer," *IEEE Transactions on Microwave Theory and Techniques*, vol. 48, no. 11, pp. 1854–1863, 2000.

[13] E. C. Fear, S. C. Hagness, P. M. Meaney, M. Okoniewski, and M. A. Stuchly, "Enhancing breast tumor detection with near-field imaging," *IEEE Microwave magazine*, vol. 3, no. 1, pp. 48–56, 2002.

[14] E. C. Fear, X. Li, S. C. Hagness, and M. A. Stuchly, "Confocal microwave imaging for breast cancer detection: Localization of tumors in three dimensions," *IEEE Transactions on Biomedical Engineering*, vol. 49, no. 8, pp. 812–822, 2002.

[15] A. H. Barrett and P. C. Myers, *Basic principles and applications of microwave thermography*. Piscataway, NJ: IEEE Press, 1986.

[16] L. V. Wang, X. Zhao, H. Sun, and G. Ku, "Microwave-induced acoustic imaging of biological tissues," *Review of scientific instruments*, vol. 70, no. 9, pp. 3744–3748, 1999.

[17] E. C. Fear, J. Bourqui, C. Curtis, D. Mew, B. Docktor, and C. Romano, "Microwave breast imaging with a monostatic radar-based system: A study of application to patients," *IEEE transactions on microwave theory and techniques*, vol. 61, no. 5, pp. 2119–2128, 2013.

[18] Y. Zhang, S. Tu, R. K. Amineh, and N. K. Nikolova, "Sensitivity-based microwave imaging with raster scanning," in *Microwave Symposium Digest (MTT), 2012 IEEE MTT-S International*, 2012, pp. 1–3.

[19] M. Klemm, I. J. Craddock, J. A. Leendertz, A. Preece, and R. Benjamin, "Radar-based breast cancer detection using a hemispherical antenna array—experimental results," *IEEE transactions on antennas and propagation*, vol. 57, no. 6, pp. 1692–1704, 2009.

[20] N. K. Nikolova, "Microwave biomedical imaging," *Wiley Encyclopedia of Electrical and Electronics Engineering*, 2014.

[21] R. K. Amineh, M. Ravan, A. Trehan, and N. K. Nikolova, "Near-field microwave imaging based on aperture raster scanning with tem horn antennas," *IEEE Transactions on Antennas and Propagation*, vol. 59, no. 3, pp. 928–940, 2011.

[22] P. M. Meaney, M. W. Fanning, T. Raynolds, C. J. Fox, Q. Fang, C. A. Kogel, S. P. Poplack, and K. D. Paulsen, "Initial clinical experience with microwave breast imaging in women with normal mammography," *Academic radiology*, vol. 14, no. 2, pp. 207–218, 2007.

[23] P. Meaney, M. Fanning, T. Zhou, A. Golnabi, S. Geimer, and K. Paulsen, "Clinical microwave breast imaging—2d results and the evolution to 3d," in *Electromagnetics in Advanced Applications, 2009. ICEAA'09. International Conference on*, 2009, pp. 881–884.

[24] T. M. Grzegorczyk, P. M. Meaney, P. A. Kaufman, K. D. Paulsen *et al.*, "Fast 3-d tomographic microwave imaging for breast cancer detection," *IEEE Transactions on Medical Imaging*, vol. 31, no. 8, pp. 1584–1592, 2012.

[25] A. E. Souvorov, A. E. Bulyshev, S. Y. Semenov, R. H. Svenson, and G. P. Tatsis, "Two-dimensional computer analysis of a microwave flat antenna array for breast cancer tomography," *IEEE Transactions on Microwave Theory and Techniques*, vol. 48, no. 8, pp. 1413–1415, 2000.

[26] A. E. Bulyshev, S. Y. Semenov, A. E. Souvorov, R. H. Svenson, A. G. Nazarov, Y. E. Sizov, and G. P. Tatsis, "Computational modeling of three-dimensional microwave tomography of breast cancer," *IEEE Transactions on Biomedical Engineering*, vol. 48, no. 9, pp. 1053–1056, 2001.

[27] L. Sha, L. W. Nolte, Z. Q. Zhang, and Q. H. Liu, "Performance analysis for bayesian microwave imaging in decision aided breast tumor diagnosis," in *Biomedical Imaging, 2002. Proceedings. 2002 IEEE International Symposium on*, 2002, pp. 1039–1042.

[28] P. Meaney, S. Pendergrass, M. Fanning, and K. Paulsen, "Importance of using a reduced contrast coupling medium in 2d microwave breast imaging," *Journal of Electromagnetic Waves and Applications*, vol. 17, no. 2, pp. 333–355, 2003.

[29] G. N. Bindu, S. J. Abraham, A. Lonappan, V. Thomas, C. K. Aanandan, and K. Mathew, "Active microwave imaging for breast cancer detection," *Progress In Electromagnetics Research*, vol. 58, pp. 149–169, 2006.

[30] M. Xu, A. Sabouni, P. Thulasiraman, S. Noghanian, and S. Pistorius, "Image reconstruction using microwave tomography for breast cancer detection on distributed memory machine," in *Parallel Processing, 2007. ICPP International Conference on*, 2007, pp. 36–36.

[31] M. Xu *et al.*, "A parallel algorithmic approach for microwave tomography in breast cancer detection," in *Parallel and Distributed Processing Symposium, 2007. IPDPS IEEE International*, 2007, pp. 1–8.

[32] N. Irishina, O. Dorn, and M. Moscoso, "A level set evolution strategy in microwave imaging for early breast cancer detection," *Computers & Mathematics with Applications*, vol. 56, no. 3, pp. 607–618, 2008.

[33] M. Guardiola, S. Capdevila, S. Blanch, J. Romeu, and L. Jofre, "Uwb high-contrast robust tomographic imaging for medical applications," in *Electromagnetics in Advanced Applications, 2009. ICEAA'09. International Conference on*, 2009, pp. 560–563.

[34] J. D. Shea, P. Kosmas, S. C. Hagness, and B. D. Van Veen, "Three-dimensional microwave imaging of realistic numerical breast phantoms via a multiple-frequency inverse scattering technique," *Medical physics*, vol. 37, no. 8, pp. 4210–4226, 2010.

[35] A. Diaz-Bolado, P.-A. Barriere, and J.-J. Laurin, "On the effect of breast compression and measurement setup configuration in microwave tomography for breast cancer detection," in *Antennas and Propagation (APSURSI), 2011 IEEE International Symposium on*, 2011, pp. 714–717.

[36] A. Diaz-Bolado, T. Henriksson, P.-A. Barriere, H. Memarzadeh-Tehran, N. Joachimowicz, C. Conessa, A. Joisel, B. Duchêne, J.-J. Laurin, and J.-C. Bolomey, "Towards a planar microwave tomography system for early stage breast cancer detection," in *General Assembly and Scientific Symposium, 2011 XXXth URSI*, 2011, pp. 1–4.

[37] X. Zeng, A. Fhager, and M. Persson, "Effects of noise on tomographic breast imaging," in *General Assembly and Scientific Symposium, 2011 XXXth URSI*, 2011, pp. 1–4.

[38] M. Xu, P. Thulasiraman, and S. Noghanian, "Microwave tomography for breast cancer detection on cell broadband engine processors," *Journal of Parallel and Distributed Computing*, vol. 72, no. 9, pp. 1106–1116, 2012.

[39] M. Haynes, J. Stang, and M. Moghaddam, "Microwave breast imaging system prototype with integrated numerical characterization," *Journal of Biomedical Imaging*, vol. 2012, p. 2, 2012.

[40] N. Simonov, S.-I. Jeon, S.-H. Son, J.-M. Lee, and H.-J. Kim, "3d microwave breast imaging based on multistatic radar concept system," in *Synthetic Aperture Radar (APSAR), 2011 3rd International Asia-Pacific Conference on*, 2011, pp. 1–4.

[41] K.-C. Kwon, Y.-T. Lim, C.-H. Kim, N. Kim, C. Park, K.-H. Yoo, S.-H. Son, and S.-I. Jeon, "Microwave tomography analysis system for breast tumor detection," *Journal of medical systems*, vol. 36, no. 3, pp. 1757–1767, 2012.

[42] A. Diaz-Bolado, P.-A. Barriere, and J.-J. Laurin, "Study of microwave tomography measurement setup configurations for breast cancer detection based on breast compression," *International Journal of Antennas and Propagation*, vol. 2013, 2013.

[43] N. Epstein, P. Meaney, and K. Paulsen, "3d parallel-detection microwave tomography for clinical breast imaging," *Review of Scientific Instruments*, vol. 85, no. 12, p. 124704, 2014.

[44] S. Ahsan, B. Yeboah-Akowuah, P. Kosmas, H. C. García, G. Palikaras, and E. Kallos, "Balanced antipodal vivaldi antenna for microwave tomography," in *Wireless Mobile Communication and Healthcare (Mobihealth), 2014 EAI 4th International Conference on*, 2014, pp. 316–319.

[45] J. Kim, K. Lee, S. Son, S. Jeon, and N. Kim, "Temperature influence of matching liquid in a microwave tomography platform system," *Microwave and Optical Technology Letters*, vol. 56, no. 12, pp. 2978–2981, 2014.

[46] S. Ahsan, Z. Guo, I. Gouzouasis, E. Kallos, and P. Kosmas, "Development of a slotted triangular patch antenna for microwave tomography," in *Antennas and Propagation (EuCAP), 2016 10th European Conference on*, 2016, pp. 1–2.

[47] A. Shahzad, M. O'Halloran, M. Glavin, and E. Jones, "A novel optimized parallelization strategy to accelerate microwave tomography for breast cancer screening," in *Engineering in Medicine and Biology Society (EMBC), 2014 36th Annual International Conference of the IEEE*, 2014, pp. 2456–2459.

[48] P. M. Meaney, K. D. Paulsen, and T. P. Ryan, "Two-dimensional hybrid element image reconstruction for tm illumination," *IEEE transactions on antennas and propagation*, vol. 43, no. 3, pp. 239–247, 1995.

[49] P. M. Meaney, K. D. Paulsen, A. Hartov, and R. K. Crane, "An active microwave imaging system for reconstruction of 2-d electrical property distributions," *IEEE Transactions on Biomedical Engineering*, vol. 42, no. 10, pp. 1017–1026, 1995.

[50] P. M. Meaney, K. D. Paulsen, A. Hartov, and R. Crane, "Microwave imaging for tissue assessment: Initial evaluation in multitarget tissue-equivalent phantoms," *IEEE Transactions on Biomedical Engineering*, vol. 43, no. 9, pp. 878–890, 1996.

[51] P. M. Meaney, K. D. Paulsen, and J. T. Chang, "Near-field microwave imaging of biologically-based materials using a monopole transceiver system," *IEEE Transactions on Microwave Theory and Techniques*, vol. 46, no. 1, pp. 31–45, 1998.

[52] S. Kwon and S. Lee, "Recent advances in microwave imaging for breast cancer detection," *International journal of biomedical imaging*, vol. 2016, 2016.

[53] G. Bindu, S. J. Abraham, A. Lonappan, V. Thomas, C. Aanandan, and K. Mathew, "Detection of dielectric contrast of breast tissues using confocal microwave technique," *Microwave and Optical Technology Letters*, vol. 48, no. 6, pp. 1187–1190, 2006.

[54] M. Ambrosanio, P. Kosmasy, and V. Pascazio, "An adaptive multi-threshold iterative shrinkage algorithm for microwave imaging applications," in *Antennas and Propagation (EuCAP), 2016 10th European Conference on*, 2016, pp. 1–3.

[55] O. M. Bucci, G. Bellizzi, A. Borgia, S. Costanzo, L. Crocco, G. Di Massa, and R. Scapaticci, "Experimental feasibility assessment of mnp enhanced microwave diagnostics of breast cancer," in *Antennas and Propagation (EuCAP), 2016 10th European Conference on*, 2016, pp. 1–4.

[56] R. Scapaticci, G. Bellizzi, I. Catapano, L. Crocco, and O. M. Bucci, "An effective procedure for mnp-enhanced breast cancer microwave imaging," *IEEE Transactions on Biomedical Engineering*, vol. 61, no. 4, pp. 1071–1079, 2014.

[57] S. Ley, M. Helbig, and J. Sachs, "Preliminary investigations of magnetic modulated nanoparticles for microwave breast cancer detection," *Current directions in biomedical engineering*, vol. 1, no. 1, pp. 302–305, 2015.

[58] O. M. Bucci, G. Bellizzi, A. Borgia, S. Costanzo, L. Crocco, G. Di Massa, and R. Scapaticci, "Characterization of a laboratory set-up for assessing the feasibility of magnetic nanoparticles enhanced microwave imaging," in *Antennas and Propagation (EuCAP), 2016 10th European Conference on*, 2016, pp. 1–4.

[59] H. Luyen, S. C. Hagness, and N. Behdad, "A balun-free helical antenna for minimally invasive microwave ablation," *IEEE Transactions on Antennas and Propagation*, vol. 63, no. 3, pp. 959–965, 2015.

[60] R. O. Mays, L. Neira, H. Luyen, L. Wilke, N. Behdad, and S. Hagness, "Advances in microwave ablation antennas for breast tumor treatment," in *Antennas and Propagation (EuCAP), 2016 10th European Conference on*, 2016, pp. 1–3.

[61] D. A. Iero, T. Isernia, A. F. Morabito, I. Catapano, and L. Crocco, "Optimal constrained field focusing for hyperthermia cancer therapy: A feasibility assessment on realistic phantoms," *Progress In Electromagnetics Research*, vol. 102, pp. 125–141, 2010.

[62] X. Li and S. C. Hagness, "A confocal microwave imaging algorithm for breast cancer detection," *IEEE Microwave and wireless components letters*, vol. 11, no. 3, pp. 130–132, 2001.

[63] I. Craddock, M. Klemm, J. Leendertz, A. Preece, and R. Benjamin, "Development and application of a uwb radar system for breast imaging," in *Antennas and Propagation Conference, 2008. LAPC 2008. Loughborough*, 2008, pp. 24–27.

[64] S. C. Hagness, A. Taflove, and J. E. Bridges, "Two-dimensional fdtd analysis of a pulsed microwave confocal system for breast cancer detection: Fixed-focus and antenna-array sensors," *IEEE Transactions on Biomedical Engineering*, vol. 45, no. 12, pp. 1470–1479, 1998.

[65] R. Nilavalan, A. Gbedemah, I. J. Craddock, X. Li, and S. C. Hagness, "Numerical investigation of breast tumour detection using," *Electronics Letters*, vol. 39, no. 25, pp. 1787–1789, Dec 2003.

[66] R. Nilavalan, J. Leendertz, I. Craddock, A. Preece, and R. Benjamin, "Numerical analysis of microwave detection of breast tumours using synthetic focussing techniques," in *Antennas and Propagation Society International Symposium, 2004. IEEE*, vol. 3, 2004, pp. 2440–2443.

[67] R. Nilavalan, I. Craddock, J. Leendertz, A. Preece, and R. Benjamin, "A wideband planar antenna for in-body imaging," in *Antennas and Propagation Society International Symposium, 2005 IEEE*, vol. 1, 2005, pp. 848–851.

[68] S. K. Davis, H. Tandradinata, S. C. Hagness, and B. D. Van Veen, "Ultrawideband microwave breast cancer detection: a detection-theoretic approach using the generalized likelihood ratio test," *IEEE transactions on biomedical engineering*, vol. 52, no. 7, pp. 1237–1250, 2005.

[69] H. B. Lim, N. T. T. Nhung, E.-P. Li, and N. D. Thang, "Confocal microwave imaging for breast cancer detection: Delay-multiply-and-sum image reconstruction algorithm," *IEEE Transactions on Biomedical Engineering*, vol. 55, no. 6, pp. 1697–1704, 2008.

[70] M. O'Halloran, M. Glavin, and E. Jones, "Channel-ranked beamformer for the early detection of breast cancer," *Progress In Electromagnetics Research*, vol. 103, pp. 153–168, 2010.

[71] D. Byrne, M. O'Halloran, M. Glavin, and E. Jones, "Data independent radar beamforming algorithms for breast cancer detection," *Progress In Electromagnetics Research*, vol. 107, pp. 331–348, 2010.

[72] M. O'Halloran, E. Jones, and M. Glavin, "Quasi-multistatic mist beamforming for the early detection of breast cancer," *IEEE Transactions on Biomedical Engineering*, vol. 57, no. 4, pp. 830–840, 2010.

[73] Y. Chen, I. J. Craddock, P. Kosmas, M. Ghavami, and P. Rapajic, "Multiple-input multiple-output radar for lesion classification in ultrawideband breast imaging," *IEEE Journal of Selected Topics in Signal Processing*, vol. 4, no. 1, pp. 187–201, 2010.

[74] A. Shahzad, M. O'halloran, E. Jones, and M. Glavin, "Prefiltered beamforming for early-stage breast cancer detection," *IEEE Antennas and Wireless Propagation Letters*, vol. 12, pp. 500–503, 2013.

[75] L. Xu, X. Xiao, and T. Kikkawa, "Improved beamforming algorithm for imaging reconstruction for early breast cancer detection by uwb," *Journal of Circuits, Systems, and Computers*, vol. 22, no. 10, p. 1340027, 2013.

[76] M. Elahi, A. Shahzad, M. Glavin, E. Jones, and M. O'halloran, "Hybrid artifact removal for confocal microwave breast imaging," *IEEE Antennas and Wireless Propagation Letters*, vol. 13, pp. 149–152, 2014.

[77] X. Xia, S. Hang, W. Zong-Jie, and W. Liang, "A progressive processing method for breast cancer detection via uwb based on an mri-derived model," *Chinese Physics B*, vol. 23, no. 7, 2014.

[78] Q. Li, X. Xiao, H. Song, L. Wang, and T. Kikkawa, "Tumor response extraction based on ensemble empirical mode decomposition for early breast cancer detection by uwb," in *Biomedical Circuits and Systems Conference (BioCAS), 2014 IEEE*, 2014, pp. 97–100.

[79] M. Elahi, C. Curtis, E. Jones, M. Glavin, E. Fear, and M. O'Halloran, "Detailed evaluation of artifact removal algorithms for radar-based microwave imaging of the breast," in *Radio Science Meeting (Joint with AP-S Symposium), 2015 USNC-URSI*, 2015, pp. 307–307.

[80] J. Moll, D. Wörtge, D. Byrne, M. Klemm, and V. Krozer, "Experimental phantom for contrast enhanced microwave breast cancer detection based on 3d-printing technology," in *Antennas and Propagation (EuCAP), 2016 10th European Conference on*, 2016, pp. 1–4.

[81] D. O'Loughlin, F. Krewer, M. Glavin, E. Jones, and M. O'Halloran, "Estimating average dielectric properties for microwave breast imaging using focal quality metrics," in *Antennas and Propagation (EuCAP), 2016 10th European Conference on*, 2016, pp. 1–5.

[82] D. Byrne and I. J. Craddock, "Time-domain wideband adaptive beamforming for radar breast imaging," *IEEE Transactions on Antennas and Propagation*, vol. 63, no. 4, pp. 1725–1735, 2015.

[83] D. J. Griffiths, *Introduction to electrodynamics*. AAPT, 2005.

[84] K. Yee, "Numerical solution of initial boundary value problems involving maxwell's equations in isotropic media," *IEEE Transactions on antennas and propagation*, vol. 14, no. 3, pp. 302–307, 1966.

[85] S. Salon and M. Chari, *Numerical methods in electromagnetism*. Academic press, 1999.

[86] R. Holland and J. W. Williams, "Total-field versus scattered-field finite-difference codes: A comparative assessment," *IEEE Transactions on Nuclear Science*, vol. 30, no. 6, pp. 4583–4588, 1983.

[87] A. Bayliss, M. Gunzburger, and E. Turkel, "Boundary conditions for the numerical solution of elliptic equations in exterior regions," *SIAM Journal on Applied Mathematics*, vol. 42, no. 2, pp. 430–451, 1982.

[88] G. Mur, "Absorbing boundary conditions for the finite-difference approximation of the time-domain electromagnetic-field equations," *IEEE transactions on Electromagnetic Compatibility*, no. 4, pp. 377–382, 1981.

[89] T. G. Moore, J. G. Blaschak, A. Taflove, and G. A. Kriegsmann, "Theory and application of radiation boundary operators," *IEEE Transactions on Antennas and Propagation*, vol. 36, no. 12, pp. 1797–1812, 1988.

[90] R. L. Higdon, "Absorbing boundary conditions for difference approximations to the multidimensional wave equation," *Mathematics of computation*, vol. 47, no. 176, pp. 437–459, 1986.

[91] R. Higdon, "Numerical absorbing boundary conditions for the wave equation," *Mathematics of computation*, vol. 49, no. 179, pp. 65–90, 1987.

[92] J.-P. Berenger, "A perfectly matched layer for the absorption of electromagnetic waves," *Journal of computational physics*, vol. 114, no. 2, pp. 185–200, 1994.

[93] J. A. Roden and S. D. Gedney, "Convolution pml (cpml): An efficient fdtd implementation of the cfs–pml for arbitrary media," *Microwave and Optical Technology Letters*, vol. 27, no. 5, pp. 334–339, 2000.

[94] R. J. Luebbers and F. Hunsberger, "Fdtd for nth-order dispersive media," *IEEE transactions on Antennas and Propagation*, vol. 40, no. 11, pp. 1297–1301, 1992.

[95] J. H. Beggs, R. J. Luebbers, K. S. Yee, and K. S. Kunz, "Finite-difference time-domain implementation of surface impedance boundary conditions," *IEEE Transactions on Antennas and Propagation*, vol. 40, no. 1, pp. 49–56, Jan 1992.

[96] K. Foster and H. Schwan, "Dielectric properties of tissues and biological materials: A critical review," *Critical reviews in biomedical engineering*, vol. 17, pp. 25–104, Feb 1989.

[97] M. Lazebnik, L. McCartney, D. Popovic, C. B. Watkins, M. J. Lindstrom, J. Harter, S. Sewall, A. Magliocco, J. H. Booske, M. Okoniewski *et al.*, "A large-scale study of the ultrawideband microwave dielectric properties of normal breast tissue obtained from reduction surgeries," *Physics in medicine and biology*, vol. 52, no. 10, p. 2637, 2007.

[98] L. Liberman and J. H. Menell, "Breast imaging reporting and data system (bi-rads)," *Radiologic Clinics*, vol. 40, no. 3, pp. 409–430, 2002.

[99] D. W. Winters, E. J. Bond, B. D. Van Veen, and S. C. Hagness, "Estimation of the frequency-dependent average dielectric properties of breast tissue using a time-domain inverse scattering technique," *IEEE Transactions on Antennas and Propagation*, vol. 54, no. 11, pp. 3517–3528, 2006.

[100] S. K. Davis, *Ultrawideband radar-based detection and classification of breast tumors*. University of Wisconsin–Madison, 2006.

[101] M. Converse, E. J. Bond, B. Veen, and C. Hagness, "A computational study of ultra-wideband versus narrowband microwave hyperthermia for breast cancer treatment," *IEEE transactions on microwave theory and techniques*, vol. 54, no. 5, pp. 2169–2180, 2006.

[102] S. Gabriel, R. Lau, and C. Gabriel, "The dielectric properties of biological tissues: Iii. parametric models for the dielectric spectrum of tissues," *Physics in medicine and biology*, vol. 41, no. 11, p. 2271, 1996.

[103] W. C. Chew and W. C. Chew, *Waves and fields in inhomogeneous media*. IEEE press New York, 1995, vol. 522.

[104] M. Born and E. Wolf, "Principles of optics, 1980," *Figure*, vol. 10, pp. 524–526, 1980.

[105] W. C. Chew and Y.-M. Wang, "Reconstruction of two-dimensional permittivity distribution using the distorted born iterative method," *IEEE transactions on medical imaging*, vol. 9, no. 2, pp. 218–225, 1990.

[106] M. Bertero and P. Boccacci, *Introduction to inverse problems in imaging*. CRC press, 1998.

[107] J. Dongarra and F. Sullivan, "Guest editors introduction to the top 10 algorithms," *Computing in Science Engineering*, vol. 2, no. 1, pp. 22–23, Jan 2000.

[108] K. Bredies, D. A. Lorenz, and P. Maass, "A generalized conditional gradient method and its connection to an iterative shrinkage method," *Computational Optimization and Applications*, vol. 42, no. 2, pp. 173–193, 2009.

[109] C. Chaux, P. L. Combettes, J.-C. Pesquet, and V. R. Wajs, "A variational formulation for frame-based inverse problems," *Inverse Problems*, vol. 23, no. 4, p. 1495, 2007.

[110] P. L. Combettes and V. R. Wajs, "Signal recovery by proximal forward-backward splitting," *Multiscale Modeling & Simulation*, vol. 4, no. 4, pp. 1168–1200, 2005.

[111] I. Daubechies, M. Defrise, and C. De Mol, "An iterative thresholding algorithm for linear inverse problems with a sparsity constraint," *Communications on pure and applied mathematics*, vol. 57, no. 11, pp. 1413–1457, 2004.

[112] M. A. Figueiredo and R. D. Nowak, "An em algorithm for wavelet-based image restoration," *IEEE Transactions on Image Processing*, vol. 12, no. 8, pp. 906–916, 2003.

[113] E. T. Hale, W. Yin, and Y. Zhang, "Fixed-point continuation for l_1-minimization: Methodology and convergence," *SIAM Journal on Optimization*, vol. 19, no. 3, pp. 1107–1130, 2008.

[114] I. Bayram and I. W. Selesnick, "A subband adaptive iterative shrinkage/thresholding algorithm," *IEEE Transactions on Signal Processing*, vol. 58, no. 3, pp. 1131–1143, 2010.

[115] M. A. Figueiredo and R. D. Nowak, "A bound optimization approach to wavelet-based image deconvolution," in *Image Processing, 2005. ICIP 2005. IEEE International Conference on*, vol. 2, 2005.

[116] J. M. Bioucas-Dias and M. A. Figueiredo, "A new twist: Two-step iterative shrinkage/thresholding algorithms for image restoration," *IEEE Transactions on Image processing*, vol. 16, no. 12, pp. 2992–3004, 2007.

[117] S. Semenov, "Microwave tomography: review of the progress towards clinical applications," *Philosophical Transactions of the Royal Society of London A: Mathematical, Physical and Engineering Sciences*, vol. 367, no. 1900, pp. 3021–3042, 2009.

[118] D. W. Winters, J. D. Shea, P. Kosmas, B. D. Van Veen, and S. C. Hagness, "Three-dimensional microwave breast imaging: Dispersive dielectric properties estimation using patient-specific basis functions," *IEEE Transactions on Medical Imaging*, vol. 28, no. 7, pp. 969–981, 2009.

[119] C. Gilmore, A. Abubakar, W. Hu, T. M. Habashy, and P. M. van den Berg, "Microwave biomedical data inversion using the finite-difference contrast source inversion method," *IEEE Transactions on Antennas and Propagation*, vol. 57, no. 5, pp. 1528–1538, 2009.

[120] R. Scapaticci, I. Catapano, and L. Crocco, "Wavelet-based adaptive multiresolution inversion for quantitative microwave imaging of breast tissues," *IEEE Transactions on Antennas and Propagation*, vol. 60, no. 8, pp. 3717–3726, 2012.

[121] P. Kosmas, J. D. Shea, B. D. Van Veen, and S. C. Hagness, "Three-dimensional microwave imaging of realistic breast phantoms via an inexact gauss-newton algorithm," in *Antennas and Propagation Society International Symposium, 2008. AP-S 2008. IEEE*, 2008, pp. 1–4.

[122] M. Azghani, P. Kosmas, and F. Marvasti, "Microwave medical imaging based on sparsity and an iterative method with adaptive thresholding," *IEEE transactions on medical imaging*, vol. 34, no. 2, pp. 357–365, 2015.

[123] W. Chew and J. Lin, "A frequency-hopping approach for microwave imaging of large inhomogeneous bodies," *IEEE Microwave and Guided Wave Letters*, vol. 5, no. 12, pp. 439–441, 1995.

[124] D. M. Young, *Iterative solution of large linear systems*. Elsevier, 2014.

[125] M. Azghani and F. Marvasti, "Iterative methods for random sampling and compressed sensing recovery," in *Sampling Theory and Applications. Proceedings of 10th International Conference on Eurasip*, 2013.

[126] O. Axelsson, *Iterative solution methods*. Cambridge university press, 1996.

[127] T. Blumensath and M. E. Davies, "Iterative thresholding for sparse approximations," *Journal of Fourier Analysis and Applications*, vol. 14, no. 5, pp. 629–654, 2008.

[128] M. Hanke, "Accelerated landweber iterations for the solution of ill-posed equations," *Numerische mathematik*, vol. 60, no. 1, pp. 341–373, 1991.

[129] Y. Wang and W. C. Chew, "An iterative solution of the two-dimensional electromagnetic inverse scattering problem," *International Journal of Imaging Systems and Technology*, vol. 1, no. 1, pp. 100–108, 1989.

[130] E. Zastrow, S. K. Davis, M. Lazebnik, F. Kelcz, B. D. Van Veen, and S. C. Hagness, "Development of anatomically realistic numerical breast phantoms with accurate dielectric properties for modeling microwave interactions with the human breast," *IEEE Transactions on Biomedical Engineering*, vol. 55, no. 12, pp. 2792–2800, 2008.

[131] M. Azghani *et al.*, "Microwave medical imaging based on sparsity and an iterative method with adaptive thresholding," *IEEE Trans. Med. Imag.*, 2015.

[132] Z. Miao and P. Kosmas, "Microwave breast imaging based on an optimized two-step iterative shrinkage/thresholding method," in *Antennas and Propagation (EuCAP), 2015 9th European Conference on*, 2015, pp. 1–4.

[133] J. D. Shea *et al.*, "Three-dimensional microwave imaging of realistic numerical breast phantoms via a multiple-frequency inverse scattering technique," *Medical Physics*, vol. 37, no. 8, pp. 4210–4226, 2010.

[134] W. Chew and J. Lin, "A frequency-hopping approach for microwave imaging of large inhomogeneous bodies," *Microwave and Guided Wave Letters, IEEE*, vol. 5, no. 12, pp. 439–441, Dec 1995.

[135] R. Scapaticci *et al.*, "Wavelet-based regularization for robust microwave imaging in medical applications," *IEEE Trans. Biomed. Eng.*, vol. 62, no. 4, pp. 1195–1202, April 2015.

[136] E. Zastrow *et al.*, "Development of anatomically realistic numerical breast phantoms with accurate dielectric properties for modeling microwave interactions with the human breast," *IEEE Trans. Biomed. Eng.*, vol. 55, no. 12, pp. 2792–2800, Dec 2008.

[137] O. Bucci and T. Isernia, "Electromagnetic inverse scattering: Retrievable information and measurement strategies," *Radio Science*, vol. 32, no. 6, pp. 2123–2137, 1997.

[138] Y. Saad, *Iterative methods for sparse linear systems*. SIAM, 2003.

[139] M. R. Hestenes and E. Stiefel, *Methods of conjugate gradients for solving linear systems*. NBS, 1952, vol. 49, no. 1.

[140] A. Van der Sluis and H. A. van der Vorst, "The rate of convergence of conjugate gradients," *Numerische Mathematik*, vol. 48, no. 5, pp. 543–560, 1986.

[141] J. R. Shewchuk *et al.*, *An introduction to the conjugate gradient method without the agonizing pain*. Carnegie-Mellon University. Department of Computer Science, 1994.

[142] P. C. Hansen, *Rank-deficient and discrete ill-posed problems: numerical aspects of linear inversion*. SIAM, 1998.

[143] C. Paige and M. Saunders, "Lsqr: An algorithm for sparse linear equations and sparse least squares," *ACM transactions on mathematical software*, vol. 8, no. 1, pp. 43–71, 1982.

[144] C. C. Paige and M. A. Saunders, "Algorithm 583: Lsqr: Sparse linear equations and least squares problems," *ACM Transactions on Mathematical Software (TOMS)*, vol. 8, no. 2, pp. 195–209, 1982.

[145] G. H. Golub and C. F. Van Loan, "Matrix computations, the john's hopkins univ," *Press, Baltimore*, 1983.

[146] G. Strang, G. Strang, G. Strang, and G. Strang, *Introduction to linear algebra*. Wellesley-Cambridge Press Wellesley, MA, 1993, vol. 3.

[147] Å. Björck and T. Elfving, "Accelerated projection methods for computing pseudoinverse solutions of systems of linear equations," *BIT Numerical Mathematics*, vol. 19, no. 2, pp. 145–163, 1979.

[148] C. Lanczos, *An iteration method for the solution of the eigenvalue problem of linear differential and integral operators*. United States Governm. Press Office Los Angeles, CA, 1950.

[149] G. Golub and W. Kahan, "Calculating the singular values and pseudo-inverse of a matrix," *Journal of the Society for Industrial and Applied Mathematics, Series B: Numerical Analysis*, vol. 2, no. 2, pp. 205–224, 1965.

[150] P. C. Hansen, *The L-curve and its use in the numerical treatment of inverse problems*. IMM, Department of Mathematical Modelling, Technical Universityof Denmark, 1999.

[151] F. Gao *et al.*, "Sensitivity of the distorted born iterative method to the initial guess in microwave breast imaging," *IEEE Trans. Antennas Propag.*, vol. 63, no. 8, pp. 3540–3547, 2015.

[152] T. Grzegorczyk *et al.*, "Fast 3-d tomographic microwave imaging for breast cancer detection," *IEEE Trans. Med. Imag.*, vol. 31, no. 8, pp. 1584–1592, Aug 2012.

[153] T. Isernia *et al.*, "On the local minima in a tomographic imaging technique," *IEEE Trans. Geosci. Remote Sens.*, vol. 39, no. 7, pp. 1596–1607, Jul 2001.

[154] A. Borsic *et al.*, "In vivo impedance imaging with total variation regularization," *IEEE Trans. Med. Imag.*, vol. 29, no. 1, pp. 44–54, Jan 2010.

[155] J. Nasehi Tehrani *et al.*, "A comparison between compressed sensing algorithms in electrical impedance tomography," in *Engineering in Medicine and Biology Society (EMBC), 2010 Annual International Conference of the IEEE*, Aug 2010, pp. 3109–3112.

[156] R. K. Amineh *et al.*, "Three-dimensional near-field microwave holography using reflected and transmitted signals," *IEEE Trans. on Antennas Propag.*, vol. 59, no. 12, pp. 4777–4789, Dec 2011.

[157] M. H. Bakr and N. K. Nikolova, "An adjoint variable method for time domain tlm with fixed structured grids," in *IEEE MTT-S International Microwave Symposium Digest, 2003*, vol. 2, June 2003, pp. 1121–1124 vol.2.

[158] C. Gilmore *et al.*, "A wideband microwave tomography system with a novel frequency selection procedure," *IEEE Transactions on Biomedical Engineering*, vol. 57, no. 4, pp. 894–904, April 2010.

[159] S. S. Chen *et al.*, "Atomic decomposition by basis pursuit," *SIAM journal on scientific computing*, vol. 20, no. 1, pp. 33–61, 1998.

[160] C.R.Vogel, "Non-convergence of the l-curve regularization parameter selection method," *Inverse problems*, vol. 12, no. 4, p. 535, 1996.

[161] P. Kosmas, C. M. Rappaport, and E. Bishop, "Modeling with the fdtd method for microwave breast cancer detection," *IEEE Trans. Microw. Theory Tech.*, vol. 52, no. 8, pp. 1890–1897, 2004.

[162] G. Colin *et al.*, "A study of matching fluid loss in a biomedical microwave tomography system," *Medical Physics*, vol. 40, no. 2, 2013.

[163] G. Bindu *et al.*, "Dielectric studies of corn syrup for applications in microwave breast imaging," *Progress In Electromagnetics Research*, vol. 59, pp. 175–186, 2006.

[164] M. Koutsoupidou, P. Kosmas, S. Ahsan, Z. Miao, I. Sotiriou, and T. Kallos, "Towards a microwave imaging prototype based on the dbim-twist algorithm and a custom-made transceiver system," in *2017 8th International Conference on Environmental Engineering and Applications (ICEEA 2017)*, 2017.

[165] N. Joachimowicz, C. Conessa, T. Henriksson, and B. Duchêne, "Breast phantoms for microwave imaging," *IEEE Antennas and Wireless Propagation Letters*, vol. 13, pp. 1333–1336, 2014.

[166] N. Joachimowicz, B. Duchêne, C. Conessa, and O. Meyer, "Easy-to-produce adjustable realistic breast phantoms for microwave imaging," in *Antennas and Propagation (EuCAP), 2016 10th European Conference on*, 2016, pp. 1–4.

[167] S. Romeo, L. Di Donato, O. M. Bucci, I. Catapano, L. Crocco, M. R. Scarfì, and R. Massa, "Dielectric characterization study of liquid-based materials for mimicking breast tissues," *Microwave and Optical Technology Letters*, vol. 53, no. 6, pp. 1276–1280, 2011.

[168] P. M. Meaney, K. D. Paulsen, B. W. Pogue, and M. I. Miga, "Microwave image reconstruction utilizing log-magnitude and unwrapped phase to improve high-contrast object recovery," *IEEE transactions on medical imaging*, vol. 20, no. 2, pp. 104–116, 2001.

Appendix A

Implementation of Breast Microwave Imaging in Matlab Code

A.1 Core Matlab Code of 2-D FDTD Simulation with CPML

```
% LOAD VARIABLES FROM MIAN PROGRAM
function FDTD_Prep_path = FDTD_Preprocess(filename, delT, ...
    pml_coarse, dimX, dimY, bbox_interior_mask, ...
 mu0, eps0, delX, EpsS, antLocations_coarse_2D)
% nmax = timeSteps;
dt = delT;
%%%%%%%%%%%%%%%%%%%%%%%%%%%%%%%%%%%%%%%%%%%%%%%%%%%%%%%%%%%%%%%%%%%%%%%%%%%%
% PML thickness in each direction
pml_size = pml_coarse; % pml_coarse is loaded in sim_params_2D.mat
Imax = dimX+2*pml_size;
Jmax = dimY+2*pml_size;
XBB = (1+pml_size):(Imax-pml_size);
YBB = (1+pml_size):(Jmax-pml_size);
```

```
13 [I, J] = ind2sub([dimX dimY], bbox_interior_mask);
14 bbox_interior_mask_extend = sub2ind([Imax Jmax], I+pml_size, ...
       J+pml_size);
15 % transfer the location of the antenna to an extended field with PML
16 isource = antLocations_coarse_2D+pml_size; %the position of antennas
17 isource_ind = sub2ind([Imax, Jmax], isource(:, 1), isource(:, 2));
18 % = = =  = = set PML parameters = = = = = = =
19 eta = sqrt(mu0/ (eps0*EpsS));
20 poly_m = 3; % polynomial order for pml grading
21 alpha_m = 1.0;
22 m = poly_m;
23 ma = alpha_m;
24 sig_opt = 0.8*(poly_m+1.0) / (eta*delX);
25 sig_x_max = sig_opt;
26 sig_y_max = sig_x_max;
27 alpha_x_max = 0.03; %0.24;
28 alpha_y_max = alpha_x_max;
29 kappa_x_max = 1.0; %2.0;
30 kappa_y_max = kappa_x_max;
31 % = = = = FDTD parameters for E and H fields = = = = = = = =
32 % E-Field
33 % x-dir
34 be_x_1 = zeros(pml_size, 1);
35 ce_x_1 = zeros(pml_size, 1);
36 alphae_x_PML_1 = zeros(pml_size, 1);
37 sige_x_PML_1 = zeros(pml_size, 1);
38 kappae_x_PML_1 = zeros(pml_size, 1);
39 be_x_2 = zeros(pml_size, 1);
40 ce_x_2 = zeros(pml_size, 1);
41 alphae_x_PML_2 = zeros(pml_size, 1);
42 sige_x_PML_2 = zeros(pml_size, 1);
43 kappae_x_PML_2 = zeros(pml_size, 1);
44 % y-dir
```

```
45 be_y_1 = zeros(pml_size, 1);
46 ce_y_1 = zeros(pml_size, 1);
47 alphae_y_PML_1 = zeros(pml_size, 1);
48 sige_y_PML_1 = zeros(pml_size, 1);
49 kappae_y_PML_1 = zeros(pml_size, 1);
50 be_y_2 = zeros(pml_size, 1);
51 ce_y_2 = zeros(pml_size, 1);
52 alphae_y_PML_2 = zeros(pml_size, 1);
53 sige_y_PML_2 = zeros(pml_size, 1);
54 kappae_y_PML_2 = zeros(pml_size, 1);
55 %%%%%%%%%%%%%%%%%%%%%%%%%%%%%%%%%%%%%%%%
56 % H-Field
57 % x-dir
58 bh_x_1 = zeros(pml_size-1, 1);
59 ch_x_1 = zeros(pml_size-1, 1);
60 alphah_x_PML_1 = zeros(pml_size-1, 1);
61 sigh_x_PML_1 = zeros(pml_size-1, 1);
62 kappah_x_PML_1 = zeros(pml_size-1, 1);
63 bh_x_2 = zeros(pml_size-1, 1);
64 ch_x_2 = zeros(pml_size-1, 1);
65 alphah_x_PML_2 = zeros(pml_size-1, 1);
66 sigh_x_PML_2 = zeros(pml_size-1, 1);
67 kappah_x_PML_2 = zeros(pml_size-1, 1);
68 % y-dir
69 bh_y_1 = zeros(pml_size-1, 1);
70 ch_y_1 = zeros(pml_size-1, 1);
71 alphah_y_PML_1 = zeros(pml_size-1, 1);
72 sigh_y_PML_1 = zeros(pml_size-1, 1);
73 kappah_y_PML_1 = zeros(pml_size-1, 1);
74 bh_y_2 = zeros(pml_size-1, 1);
75 ch_y_2 = zeros(pml_size-1, 1);
76 alphah_y_PML_2 = zeros(pml_size-1, 1);
77 sigh_y_PML_2 = zeros(pml_size-1, 1);
```

```
78 kappah_y_PML_2 = zeros(pml_size-1, 1);
79 % Denominators for the update equations
80 den_ex = zeros(Imax, Jmax);
81 den_hx = zeros(Imax-1, Jmax-1);
82 den_ey = zeros(Imax, Jmax);
83 den_hy = zeros(Imax-1, Jmax-1);
84 % SET CPML PARAMETERS IN EACH DIRECTION
85 % x-dir
86  for i = 1:pml_size
87   sige_x_PML_1(i) = sig_x_max * ( (pml_size - i) / (pml_size - ...
        1.0) )^m;
88   alphae_x_PML_1(i) = alpha_x_max*((i-1.0) / (pml_size-1.0))^ma;
89   kappae_x_PML_1(i) = 1.0+(kappa_x_max-1.0) *((pml_size - i) / ...
        (pml_size - 1.0))^m;
90   be_x_1(i) = exp(-(sige_x_PML_1(i) / kappae_x_PML_1(i) + ...
        alphae_x_PML_1(i)) *dt/eps0);
91   if ((sige_x_PML_1(i) == 0.0) && (alphae_x_PML_1(i) == 0.0) && ...
        (i == pml_size))
92    ce_x_1(i) = 0.0;
93   else
94    ce_x_1(i) = sige_x_PML_1(i) *(be_x_1(i)-1.0) / ...
         (sige_x_PML_1(i)+kappae_x_PML_1(i) *alphae_x_PML_1(i)) / ...
         kappae_x_PML_1(i);
95   end
96  end
97  for i = 1:pml_size-1
98   sigh_x_PML_1(i) = sig_x_max * ( (pml_size - i - 0.5) / ...
        (pml_size-1.0))^m;
99   alphah_x_PML_1(i) = alpha_x_max*((i-0.5) / (pml_size-1.0))^ma;
100  kappah_x_PML_1(i) = 1.0+(kappa_x_max-1.0) *((pml_size - i - ...
        0.5) / (pml_size - 1.0))^m;
101  bh_x_1(i) = exp(-(sigh_x_PML_1(i) / kappah_x_PML_1(i) + ...
        alphah_x_PML_1(i)) *dt/eps0);
```

```
102    ch_x_1(i) = sigh_x_PML_1(i) *(bh_x_1(i)-1.0) / ...
           (sigh_x_PML_1(i)+kappah_x_PML_1(i) *alphah_x_PML_1(i)) / ...
           kappah_x_PML_1(i);
103   end
104  %-------------------
105   for i = 1:pml_size
106    sige_x_PML_2(i) = sig_x_max * ( (pml_size - i) / (pml_size - ...
           1.0) )^m;
107    alphae_x_PML_2(i) = alpha_x_max*((i-1.0) / (pml_size-1.0))^ma;
108    kappae_x_PML_2(i) = 1.0+(kappa_x_max-1.0) *((pml_size - i) / ...
           (pml_size - 1.0))^m;
109    be_x_2(i) = exp(-(sige_x_PML_2(i) / kappae_x_PML_2(i) + ...
           alphae_x_PML_2(i)) *dt/eps0);
110    if ((sige_x_PML_2(i) == 0.0) && (alphae_x_PML_2(i) == 0.0) && ...
           (i == pml_size))
111     ce_x_2(i) = 0.0;
112    else
113     ce_x_2(i) = sige_x_PML_2(i) *(be_x_2(i)-1.0) / ...
            (sige_x_PML_2(i)+kappae_x_PML_2(i) *alphae_x_PML_2(i)) / ...
            kappae_x_PML_2(i);
114    end
115   end
116   for i = 1:pml_size-1
117    sigh_x_PML_2(i) = sig_x_max * ( (pml_size - i - 0.5) / ...
           (pml_size-1.0))^m;
118    alphah_x_PML_2(i) = alpha_x_max*((i-0.5) / (pml_size-1.0))^ma;
119    kappah_x_PML_2(i) = 1.0+(kappa_x_max-1.0) *((pml_size - i - ...
           0.5) / (pml_size - 1.0))^m;
120    bh_x_2(i) = exp(-(sigh_x_PML_2(i) / kappah_x_PML_2(i) + ...
           alphah_x_PML_2(i)) *dt/eps0);
121    ch_x_2(i) = sigh_x_PML_2(i) *(bh_x_2(i)-1.0) / ...
           (sigh_x_PML_2(i)+kappah_x_PML_2(i) *alphah_x_PML_2(i)) / ...
           kappah_x_PML_2(i);
```

```
122  end
123 % y-dir
124  for j = 1:pml_size
125   sige_y_PML_1(j) = sig_y_max * ( (pml_size - j ) / (pml_size - ...
        1.0) )^m;
126   alphae_y_PML_1(j) = alpha_y_max*((j-1) / (pml_size-1.0))^ma;
127   kappae_y_PML_1(j) = 1.0+(kappa_y_max-1.0) *((pml_size - j) / ...
        (pml_size - 1.0))^m;
128   be_y_1(j) = exp(-(sige_y_PML_1(j) / kappae_y_PML_1(j) + ...
        alphae_y_PML_1(j)) *dt/eps0);
129   if ((sige_y_PML_1(j) == 0.0) && (alphae_y_PML_1(j) == 0.0) && ...
        (j == pml_size))
130    ce_y_1(j) = 0.0;
131   else
132    ce_y_1(j) = sige_y_PML_1(j) *(be_y_1(j)-1.0) / ...
         (sige_y_PML_1(j)+kappae_y_PML_1(j) *alphae_y_PML_1(j)) / ...
         kappae_y_PML_1(j);
133   end
134  end
135  for j = 1:pml_size-1
136   sigh_y_PML_1(j) = sig_y_max * ( (pml_size - j - 0.5) / ...
        (pml_size-1.0))^m;
137   alphah_y_PML_1(j) = alpha_y_max*((j-0.5) / (pml_size-1.0))^ma;
138   kappah_y_PML_1(j) = 1.0+(kappa_y_max-1.0) *((pml_size - j - ...
        0.5) / (pml_size - 1.0))^m;
139   bh_y_1(j) = exp(-(sigh_y_PML_1(j) / kappah_y_PML_1(j) + ...
        alphah_y_PML_1(j)) *dt/eps0);
140   ch_y_1(j) = sigh_y_PML_1(j) *(bh_y_1(j)-1.0) / ...
        (sigh_y_PML_1(j)+kappah_y_PML_1(j) *alphah_y_PML_1(j)) / ...
        kappah_y_PML_1(j);
141  end
142 %-------------------
143  for j = 1:pml_size
```

```
144    sige_y_PML_2(j) = sig_y_max * ( (pml_size - j ) / (pml_size - ...
           1.0) )^m;
145    alphae_y_PML_2(j) = alpha_y_max*((j-1) / (pml_size-1.0))^ma;
146    kappae_y_PML_2(j) = 1.0+(kappa_y_max-1.0) *((pml_size - j) / ...
           (pml_size - 1.0))^m;
147    be_y_2(j) = exp(-(sige_y_PML_2(j) / kappae_y_PML_2(j) + ...
           alphae_y_PML_2(j)) *dt/eps0);
148    if ((sige_y_PML_2(j) == 0.0) && (alphae_y_PML_2(j) == 0.0) && ...
           (j == pml_size))
149     ce_y_2(j) = 0.0;
150    else
151     ce_y_2(j) = sige_y_PML_2(j) *(be_y_2(j)-1.0) / ...
            (sige_y_PML_2(j)+kappae_y_PML_2(j) *alphae_y_PML_2(j)) / ...
            kappae_y_PML_2(j);
152    end
153   end
154   for j = 1:pml_size-1
155    sigh_y_PML_2(j) = sig_y_max * ( (pml_size - j - 0.5) / ...
           (pml_size-1.0))^m;
156    alphah_y_PML_2(j) = alpha_y_max*((j-0.5) / (pml_size-1.0))^ma;
157    kappah_y_PML_2(j) = 1.0+(kappa_y_max-1.0) *((pml_size - j - ...
           0.5) / (pml_size - 1.0))^m;
158    bh_y_2(j) = exp(-(sigh_y_PML_2(j) / kappah_y_PML_2(j) + ...
           alphah_y_PML_2(j)) *dt/eps0);
159    ch_y_2(j) = sigh_y_PML_2(j) *(bh_y_2(j)-1.0) / ...
           (sigh_y_PML_2(j)+kappah_y_PML_2(j) *alphah_y_PML_2(j)) / ...
           kappah_y_PML_2(j);
160   end
161  %-------------------------------------------------------
162  % FILL IN DENOMINATORS FOR FIELD UPDATES
163  %-------------------------------------------------------
164   ii = pml_size-1;
165   for i = 1:Imax-1
```

```
166   if (i ≤ pml_size-1)
167    den_hx(i, :) = 1.0/ (kappah_x_PML_1(i) *delX);
168   elseif (i ≥ Imax+1-pml_size)
169    den_hx(i, :) = 1.0/ (kappah_x_PML_2(ii) *delX);
170    ii = ii-1;
171   else
172    den_hx(i, :) = 1.0/delX;
173   end
174  end
175  jj = pml_size-1;
176  for j = 1:Jmax-1
177   if (j ≤ pml_size-1)
178    den_hy(:, j) = 1.0/ (kappah_y_PML_1(j) *delX);
179   elseif (j ≥ Jmax+1-pml_size)
180    den_hy(:, j) = 1.0/ (kappah_y_PML_2(jj) *delX);
181    jj = jj-1;
182   else
183    den_hy(:, j) = 1.0/delX;
184   end
185  end
186  %-------------------
187  ii = pml_size;
188  for i = 1:Imax-1
189   if (i ≤ pml_size)
190    den_ex(i, :) = 1.0/ (kappae_x_PML_1(i) *delX);
191   elseif (i ≥ Imax+1-pml_size)
192    den_ex(i, :) = 1.0/ (kappae_x_PML_2(ii) *delX);
193    ii = ii-1;
194   else
195    den_ex(i, :) = 1.0/delX;
196   end
197  end
198  jj = pml_size;
```

```
199   for j = 1:Jmax-1
200    if (j ≤ pml_size)
201     den_ey(:, j) = 1.0/ (kappae_y_PML_1(j) *delX);
202    elseif (j ≥ Jmax+1-pml_size)
203     den_ey(:, j) = 1.0/ (kappae_y_PML_2(jj) *delX);
204     jj = jj-1;
205    else
206     den_ey(:, j) = 1.0/delX;
207    end
208   end
209 %%% == = = = = = = = temp value for computing = = = = = = = = =
210 den_ex = den_ex(2:Imax-1, 2:Jmax-1);
211 den_ey = den_ey(2:Imax-1, 2:Jmax-1);
212 %---------- optimize the code on 12/11/2016--------
213 be_x_all = repmat(cat(1, be_x_1(2:end), zeros(Imax-2*pml_size, ...
        1), flip(be_x_2(2:end))) , 1, Jmax-2);
214 be_y_all = repmat(cat(2, be_y_1(2:end)', zeros(1, ...
        Jmax-2*pml_size), flip(be_y_2(2:end)')), Imax-2, 1);
215 ce_x_all = repmat(cat(1, ce_x_1(2:end), zeros(Imax-2*pml_size, ...
        1), flip(ce_x_2(2:end))) , 1, Jmax-2);
216 ce_y_all = repmat(cat(2, ce_y_1(2:end)', zeros(1, ...
        Jmax-2*pml_size), flip(ce_y_2(2:end)')), Imax-2, 1);
217
218 bh_x_all = repmat(cat(1, bh_x_1, zeros(Imax-1-2*(pml_size-1), ...
        1), flip(bh_x_2)), 1, Jmax-1);
219 bh_y_all = repmat(cat(2, bh_y_1', zeros(1, ...
        Jmax-1-2*(pml_size-1)), flip(bh_y_2')), Imax-1, 1);
220 ch_x_all = repmat(cat(1, ch_x_1, zeros(Imax-1-2*(pml_size-1), ...
        1), flip(ch_x_2)), 1, Jmax-1);
221 ch_y_all = repmat(cat(2, ch_y_1', zeros(1, ...
        Jmax-1-2*(pml_size-1)), flip(ch_y_2')), Imax-1, 1);
222 FDTD_Prep_path = ['FDTD_Prep' filename '.mat'];
```

```
223 save(FDTD_Prep_path, 'be_x_all', 'be_y_all', 'ce_x_all', ...
      'ce_y_all', 'bh_x_all', ...
224  'bh_y_all', 'ch_x_all', 'ch_y_all', 'den_ex', 'den_ey', ...
       'den_hy', 'den_hx', 'dt'...
225  , 'Imax', 'Jmax', 'XBB', 'YBB', 'bbox_interior_mask_extend', ...
       'isource_ind');
226 end
```

```
1  function [greensFunctions_mag, greensFunctions_pha, ...
     receivedFields_mag, ...
2    receivedFields_pha, antObs_data_test] = ...
        project_FDTD_2D(FDTD_Prep_path, estEpsInf, ...
3    estEpsDelta, estCond, tauP, dt, eps0, mu0, delX, source, ...
        numAnts, numFreqs, ...
4    omegas, timeSteps, EpsS, bbSize, esource_mag, esource_pha)
5  % This is a matlab version of code for 2-D Debye model FDTD with ...
     CPML
6  % written by Zhenzhuang Miao (Supervisor: Dr. Panagiotis Kosmas)
7  % 04/09/2012
8  %%%%%%%%%%%%%%%%%%%%%%%%%%%%%%%%%%%%%%%%%%%%%%%%%%%%%%%%%%%%
9  running_time=tic;
10 load(FDTD_Prep_path);
11 %=============================================
12 eps_s = EpsS*ones(Imax, Jmax);
13 eps_inf = EpsS*ones(Imax, Jmax);
14 sigma_s = zeros(Imax, Jmax);
15 %---------------------------------------------
16 eps_inf(XBB, YBB) = estEpsInf;
17 eps_s(XBB, YBB) = estEpsDelta + estEpsInf;
18 sigma_s(XBB, YBB) = estCond;
19 % background material
20 eps_inf(eps_inf==0) = EpsS;
```

```
eps_s(eps_s==0) = EpsS;
sigma_s(sigma_s==0) = 0;
% FILL IN UPDATING COEFFICIENTS
Kd = (2 * tauP - dt) / (2 * tauP + dt);
Beta_d = (2 * eps0 * (eps_s - eps_inf) * dt) / (2 * tauP + dt);
DA = 1.0;
DB = (dt / mu0); % ????
CA = (2 * eps0 * eps_inf - sigma_s * dt + Beta_d) ./ ...
  (2 * eps0 * eps_inf + sigma_s * dt + Beta_d);
CA = CA(2:Imax-1, 2:Jmax-1);
CB = 2*dt./(2*eps0.*eps_inf+sigma_s*dt+Beta_d);
CB = CB(2:Imax-1, 2:Jmax-1);
Beta_d = Beta_d(2:Imax-1, 2:Jmax-1); %temp value for computing
%¬¬¬¬¬¬¬¬¬¬¬¬¬¬¬¬¬¬¬¬¬¬¬¬¬¬¬¬¬¬¬¬¬¬¬¬¬¬¬¬¬¬¬¬¬¬¬¬¬¬¬¬¬¬¬¬¬¬¬¬¬¬¬
%%%%% PRE-ALLOCATE MEMORY (large chunks first) %%%%%
% for saving phasors inside FDTD observation bounding box
greensFunctions_mag = zeros(numAnts, bbSize, numFreqs);
greensFunctions_pha = zeros(numAnts, bbSize, numFreqs);
% for saving phasors at the antennas in FDTD
% % receivedFields_mag = zeros(numAnts, numAnts, numFreqs);
% % receivedFields_pha = zeros(numAnts, numAnts, numFreqs);
antObs_data_test = zeros(numAnts, numAnts, timeSteps);
% t_iH=1:Imax-1; %para for updating function H
% t_jH=1:Jmax-1; %para for updating function H
t_iE=2:Imax-1; %para for updating function E
t_jE=2:Jmax-1; %para for updating function E
%============ BEGIN TO SIMULATE ALL ANTENNAS==========
for srcAnt= 1:numAnts
  scr=tic;
  %====initialize values for field=====
  % BEGIN TIME STEP
  Ez = zeros(Imax, Jmax);
  Hx = zeros(Imax-1, Jmax-1);
```

```
54    Hy = zeros(Imax-1, Jmax-1);
55    Jd = zeros(Imax-2, Jmax-2);% t_i=2:Imax-1;
56    % CPML
57    psi_Ezx = zeros(Imax-2, Jmax-2);
58    psi_Ezy = zeros(Imax-2, Jmax-2);
59    psi_Hx = zeros(Imax-1, Jmax-1);
60    psi_Hy = zeros(Imax-1, Jmax-1);
61    tempGre_imag = zeros(bbSize, numFreqs);
62    tempGre_real = zeros(bbSize, numFreqs);
63    %============BEGIN TIME STEP==========
64    for n = 1:timeSteps
65      %============update H==================
66      [Hx, Hy, psi_Hx, psi_Hy] = FDTD_Core_H(Ez, Hx, Hy, psi_Hx, ...
          psi_Hy, ...]
67        den_hy, den_hx, DA, DB, bh_x_all, ch_x_all, bh_y_all, ...
            ch_y_all, delX);
68      %============UPDATE Ez==================
69      [Ez(t_iE, t_jE), Jd, psi_Ezx, psi_Ezy] = ...
           FDTD_Core_Ez(Ez(t_iE, t_jE), Jd, ...
70        psi_Ezx, psi_Ezy, CA, CB, Hy, Hx, den_ex, den_ey, Kd, ...
            Beta_d, ...
71        dt, delX, be_x_all, ce_x_all, be_y_all, ce_y_all);
72      %====================source============================
73      Ez(isource_ind(srcAnt)) = source(n) + Ez(isource_ind(srcAnt));
74  %     imagesc(Ez);
75      % observe field data at every obstime_ds timesteps
76      bboxObs_data=Ez( bbox_interior_mask_extend);
77      antObs_data_test(srcAnt, :, n)=Ez(isource_ind);
78      % Computing frequency-domain quantities by FFT
79      tempGre_imag = tempGre_imag + bboxObs_data * sin(omegas*n*dt);
80      tempGre_real = tempGre_real + bboxObs_data * cos(omegas*n*dt);
81    end %loop timesteps
82    disp(['number of antenna is ' num2str(srcAnt)] )
```

```
83    toc(scr);
84    % convert observations to phasors and normalize by source
85    tempGre_imag = tempGre_imag / (timeSteps/2);
86    tempGre_real = tempGre_real / (timeSteps/2);
87    % this is not the real green function, but is the Ez which ...
          will be used
88    % to obtain green function later.
89    greensFunctions_mag(srcAnt, :, :) = sqrt( tempGre_imag.^2 + ...
          tempGre_real.^2 ) ...
90      ./ repmat(esource_mag, bbSize, 1);
91    greensFunctions_pha(srcAnt, :, :) = -atan2(tempGre_imag, ...
          tempGre_real) ...
92      - repmat(esource_pha, bbSize, 1);
93  end % loop over antenna simulations
94
95  [mag, pha] = fft_trans(reshape(antObs_data_test, numAnts^2, ...
        timeSteps), omegas, ...
96    dt, esource_mag, esource_pha);
97  receivedFields_mag = reshape(mag, numAnts, numAnts, numFreqs);
98  receivedFields_pha = reshape(pha, numAnts, numAnts, numFreqs);
99  disp('the whole running time of FDTD is ')
100 toc(running_time);
101 end
```

```
1  function [Hx, Hy, psi_Hx, psi_Hy]=FDTD_Core_H(Ez,Hx, Hy, psi_Hx, ...
       psi_Hy,den_hy,den_hx,...
2       DA,DB,bh_x_all,ch_x_all,bh_y_all,ch_y_all,delX)
3  temp_Ezx=-1*diff(Ez(1:end-1,:),1,2);
4  temp_Ezy=diff(Ez(:,1:end-1),1,1);
5  Hx = DA * Hx + DB * (temp_Ezx .* den_hy);
6  psi_Hx = bh_y_all .* psi_Hx + ch_y_all .* temp_Ezx / delX;
7  Hx=Hx + DB * psi_Hx;
```

```
Hy = DA * Hy + DB *( temp_Ezy .* den_hx);
psi_Hy = bh_x_all .* psi_Hy + ch_x_all .* temp_Ezy / delX;
Hy = Hy + DB * psi_Hy;
end
```

```
function [Ez_c,Jd,psi_Ezx,psi_Ezy] = ...
    FDTD_Core_Ez(Ez_c,Jd,psi_Ezx,psi_Ezy,CA,CB,Hy,Hx,den_ex,den_ey...
     ,Kd,Beta_d,dt,delX,be_x_all,ce_x_all,be_y_all,ce_y_all)
Ez_former=Ez_c;
temp_Hy=diff(Hy(:,2:end),1,1);
temp_Hx=-1*diff(Hx(2:end,:),1,2);
%=============update main field of Ez==========
Ez_c= CA.*Ez_c+CB.*(temp_Hy.*den_ex+temp_Hx.*den_ey - ...
    0.5*(1+Kd)*Jd);
Jd=Kd*Jd+Beta_d.*(Ez_c-Ez_former)/dt;
%========update pml of Ez in x direction=========
psi_Ezx = be_x_all.*psi_Ezx + ce_x_all.*temp_Hy/delX;
% Ez(t_i,t_j) = Ez(t_i,t_j) + CB(t_i,t_j).*psi_Ezx;
%=========update pml of Ez in y direction=======
psi_Ezy = be_y_all.*psi_Ezy + ce_y_all.*temp_Hx/delX;
Ez_c=Ez_c+CB.*(psi_Ezx+psi_Ezy);
end
```

```
function [estEpsInf, estEpsDelta, estCond, tauP, EpsS, bbSize, ...
    range_c,...
     bbox_interior_mask, constraints] = Load_FDTD_material_2D ...
     (Debye_coarse_2D_model, model_phantom, ...
         logic_skin,mode,init_index)
%bbox_interior_mask is the reconstruction area.
load(['..\data\model' num2str(model_phantom) '\all_material.mat']);
```

```
6  if (strcmp(mode,'Forward_original') || ...
       strcmp(mode,'Forward_background'))
7      logic_skin=0;
8  end
9  if logic_skin % known skin in inverse process
10     range_c=(Debye_coarse_2D_model.model==0.5);
11     bbox_interior_mask=find(range_c);
12 else
13     range_c=(Debye_coarse_2D_model.model==0.5 | ...
           Debye_coarse_2D_model.model==1);
14     bbox_interior_mask=find(range_c);
15 end
16 bbSize=length(bbox_interior_mask);
17
18
19 [dimX,dimY] = size(Debye_coarse_2D_model.model);
20 switch mode
21     case 'Forward_original'
22         estEpsInf   = Debye_coarse_2D_model.EpsInf;
23         estEpsDelta = Debye_coarse_2D_model.DeltaEps;
24         estCond     = Debye_coarse_2D_model.SigmaS;
25         tauP        = mats.immer.fit.Tau;
26         EpsS        = ...
               mats.immer.fit.EpsInf(1)+mats.immer.fit.DeltaEps(1);
27
28     case {'Forward_background','Inverse'}
29         % Note that the default of initial guess is the same as ...
               inner immersion.
30         % Build 2D model based on the property of outer immersion
31         estEpsInf   = mats.immer.fit.EpsInf*ones(dimX,dimY);
32         estEpsDelta = mats.immer.fit.DeltaEps*ones(dimX,dimY);
33         estCond     = mats.immer.fit.SigmaS*ones(dimX,dimY);
34         tauP        = mats.immer.fit.Tau;
```

```
35          EpsS        = mats.immer.fit.EpsInf+mats.immer.fit.DeltaEps;
36          % insert the inner immersion
37
38          if isfield(mats,'immer_inner')
39              estEpsInf   ...
                    (Debye_coarse_2D_model.model==mats.immer_inner.flag) ...
                    = mats.immer_inner.fit.EpsInf;
40              estEpsDelta ...
                    (Debye_coarse_2D_model.model==mats.immer_inner.flag) ...
                    = mats.immer_inner.fit.DeltaEps;
41              estCond     ...
                    (Debye_coarse_2D_model.model==mats.immer_inner.flag) ...
                    = mats.immer_inner.fit.SigmaS;
42              disp('Add the inner immersion!')
43          end
44          % add skin
45          if isfield(mats,'skin') && logic_skin
46              estEpsInf   ...
                    (Debye_coarse_2D_model.model==mats.skin.flag) = ...
                    mats.skin.fit.EpsInf;
47              estEpsDelta ...
                    (Debye_coarse_2D_model.model==mats.skin.flag) = ...
                    mats.skin.fit.DeltaEps;
48              estCond     ...
                    (Debye_coarse_2D_model.model==mats.skin.flag) = ...
                    mats.skin.fit.SigmaS;
49          end
50          %-----------------------------------------------
51          if strcmp(mode,'Inverse')
52              estEpsInf(bbox_interior_mask) = ...
                    init_guess.EpsInf(init_index);
53              estEpsDelta(bbox_interior_mask) = ...
                    init_guess.DeltaEps(init_index);
```

```
54              estCond(bbox_interior_mask) = ...
                    init_guess.SigmaS(init_index);
55          end
56      otherwise
57          error('The mode is not defined!');
58  end
59  % setup the property of tank on the model
60  if isfield(mats,'tank')
61      estEpsInf   (Debye_coarse_2D_model.model==mats.tank.flag) = ...
            mats.tank.fit.EpsInf;
62      estEpsDelta (Debye_coarse_2D_model.model==mats.tank.flag) = ...
            mats.tank.fit.DeltaEps;
63      estCond     (Debye_coarse_2D_model.model==mats.tank.flag) = ...
            mats.tank.fit.SigmaS;
64  end
65  disp(['The mode of loading material is ' mode]);
66  %set constraints there are some problems unsolved
67  if isfield(mats,'immer_inner')
68      constraints.EpsInf = mats.immer_inner.fit.EpsInf;
69      constraints.DeltaEps = mats.immer_inner.fit.DeltaEps;
70      constraints.SigmaS = mats.immer_inner.fit.SigmaS;
71  else
72      constraints.EpsInf = mats.immer.fit.EpsInf;
73      constraints.DeltaEps = mats.immer.fit.DeltaEps;
74      constraints.SigmaS = mats.immer.fit.SigmaS;
75  end
76  end
```

```
1  function [antLocations_coarse_2D, resolution, mul, ...
       coarse_grid_x, coarse_grid_y,...
2    Debye_coarse_2D_model,numAnts] = ...
         Transform_Resolution(input_struct)
```

```
% input_struct may be InP or fw.
% The function is important to initize the coarse model from ...
    fine model.
% All coarse data are saved in the file of temp_coarse_2D.
def_res = 0.5; %mm
if (mod(input_struct.new_res,def_res)¬ = 0)
  disp('resolution is not integral multiple of 0.5 mm')
  return
end
mul = input_struct.new_res/def_res;

load(['..\data\model' num2str(input_struct.model_phantom) ...
    '\model' ...
  num2str(input_struct.model_phantom) '.mat'])

antLocations_coarse_2D = ceil(antLocations_fine_2D/mul);
[numAnts,¬] = size(antLocations_coarse_2D);

Debye_coarse_2D_model.model = ...
    imresize(Debye_fine_test_model,1/mul, 'nearest');
Debye_coarse_2D_model.DeltaEps = ...
    imresize(Debye_fine_test_model_EpsDelta, 1/mul, 'nearest');
Debye_coarse_2D_model.EpsInf = ...
    imresize(Debye_fine_test_model_EpsInf, 1/mul, 'nearest');
Debye_coarse_2D_model.SigmaS = ...
    imresize(Debye_fine_test_model_Sigma_s, 1/mul, 'nearest');
resolution = input_struct.new_res/10^3;
[coarse_grid_x, coarse_grid_y] = size(Debye_coarse_2D_model.model);

end
```

```
function [PairTR] = Generate_Ant_index(numAnts)
```

```
k=1;
for i=1:numAnts
    for j=1:numAnts
        if i<j
            PairTR(k,1)=i;
            PairTR(k,2)=j;
            k=k+1;
        end
    end
end
end
```

A.2 Core Matlab Code of DBIM-TwIST Algorithm

```
%==================DBIM_MF_Fine
close all
% clear
% clc
% dbstop if all error
InP.test_name=input('Please enter name of this test:','s');
InP.new_res=input('Please enter a new coarse resolution on a ...
    mulitple of 0.5(mm):');
InP.logic_skin=input('Please choose if skin will be known or ...
    not( 1 or 0 ):');
InP.opt_init=input('Please choose whether to optimize initial ...
    guess(1 or 0):');
% InP.SNR=input('Please enter the SNR of signal(0¬150,1000 for ...
    no noise):');
InP.Opt_L1=input('Please decide whether to activate the L1-norm ...
    regularization (1 or 0):');
```

```
InP.linear_method=input('Please choose a linear method from ...
    TwIST, CGLS with L-curve, or LSQR (1, 2, or 3):');
InP.model_phantom=input('Please choose a kind of breast phantom ...
    ( 1¬99 ):');
% maximum total number of iterations
total_freqs{1} = [1.5]*1e9; %GHz
total_freqs{2} = [1.9]*1e9;
total_freqs{3} = [2.3]*1e9;
total_freqs{4} = [2.7]*1e9;
% total_freqs{5} = [1.9]*1e9;
% total_freqs{6} = [2.5]*1e9;
maxIter=[15 15 15 15 ];
% check input, frequency, and path
path = Check_Input(InP, total_freqs);
global multiple_sigma
multiple_sigma = 1;
disp(['Adjustment factor is ' num2str(multiple_sigma)]);
switch InP.opt_init
    case 0 % start DBIM without optimized initial guess
        Result = ...
            DBIM_Inverse_Fun(InP,total_freqs,maxIter,'Inverse',1,1);
        save([ path InP.test_name  '--Result.mat'],'Result');
        disp('All results has been saved!');
        Save_all_figures(path);
    case 1 %start DBIM with optimized initial guess
        maxIter_opt=input('Please input the number of iterations ...
            for changing the initial guess:');
        load(['..\data\model' num2str(InP.model_phantom) ...
            '\all_material.mat']);
        num_sample=length(init_guess.EpsInf);
        for i=1:num_sample
            init_result(i) = DBIM_Inverse_Fun...
                (InP,total_freqs(1),maxIter_opt,'Inverse',i,0);
```

```
        end
        plot_initial_guess(init_result,init_guess);
        opt_init = Analyze_optimized_init(init_result,init_guess);
        save([ path InP.test_name '--init_result.mat'], ...
            'init_result', 'opt_init');
        Save_all_figures(path);
        close all
        Result = DBIM_Inverse_Fun(InP,total_freqs, maxIter, ...
            'Inverse', opt_init,1);
        save([ path InP.test_name '--Result.mat'],'Result');
        disp('All results has been saved!');
        Save_all_figures(path);
end
```

```
function Result = DBIM_Inverse_Fun(InP,total_freqs,maxIter,...
    DBIM_mode,init_index,plot_flag)
%  written by Zhenzhuang Miao (Supervisor: Dr. Panagiotis Kosmas)
%  Created on 15/05/2017
global multiple_sigma
% Original parameters
load sim_params_2D
% transformed model and relevant parameters.
[antLocations_coarse_2D, resolution, mul, coarse_grid_x, ...
   coarse_grid_y,...
    Debye_coarse_2D_model, numAnts] = Transform_Resolution(InP);
warning(['The number of antenna is ' num2str(numAnts)]);
%============initialize parameters============
timeSteps = 6000;
obs_iter = 5;  % used to plot inverse solution
numTR = numAnts*(numAnts-1)/2;
PairTR = Generate_Ant_index(numAnts);
% computational domain dimensions
```

```
dimX = coarse_grid_x;%from temp_coarse_2D.mat
dimY = coarse_grid_y;%from temp_coarse_2D.mat
delX = resolution;%from temp_coarse_2D.mat
delT = delX/(2*c);
%========Create breast model=======
[estEpsInf, estEpsDelta, estCond, tauP, EpsS, bbSize, ...
    range_c,bbox_interior_mask, constraints] = ...
        Load_FDTD_material_2D...
    (Debye_coarse_2D_model, InP.model_phantom, InP.logic_skin, ...
    DBIM_mode,init_index);
%===============pre-process the FDTD parameters==================
FDTD_Prep_path = FDTD_Preprocess(InP.test_name, delT,pml_coarse, ...
    dimX,dimY,bbox_interior_mask,...
    mu0,eps0,delX,EpsS, antLocations_coarse_2D);
%==============load calibrated data============
load(['..\data\model' num2str(InP.model_phantom) ...
    '\Calibrated_data.mat']);
load(['..\data\model' num2str(InP.model_phantom) ...
    '\forward_para.mat']);
Calibrated_Mag=10.^(Calibrated_Mag/20);
% check the forward resolution is equal to the inverse ...
    resolution, if not, stop
if fw.new_res≠ resolution * 1e3
    error('inverse resolution is not the same as forward ...
        resolution!');
end
%=========initialization of recorded value=========
Result.residual3  = zeros(sum(maxIter),1);
Result.res_diff_1 = zeros(sum(maxIter),1);
Result.res_diff_2 = zeros(sum(maxIter),1);
Result.res_diff_3 = zeros(sum(maxIter),1);
Result.L_curve_x  = zeros(sum(maxIter),1);
Result.L_curve_Ax_b=zeros(sum(maxIter),1);
```

```
contrast           =zeros(bbSize*3,1);
Result.allContrast =zeros(bbSize*3,sum(maxIter));
iter_total=1;  % temp para for counting
disp('Start to reconstruct the MWI...')
for ind_freq = 1:length(total_freqs)  % frequency hopping approach
    fctrs = total_freqs{ind_freq};
    omegas = 2*pi*fctrs;
    numFreqs=length(fctrs);
    disp(['Current frequency is ' num2str(fctrs/1e9) ' GHz']);
    switch fw.mode
        case 'Forward_original'
            [source,timeSteps]=create_GMS(fw.fctr,delT,'wide',...
                timeSteps, dimX, dimY, 0);
        case 'Forward_background'
            [source,timeSteps]=create_GMS(fw.fctr,delT,'wide',...
                timeSteps, dimX, dimY, 0);
    end
    [esource_mag,esource_pha] = fft_trans(source, omegas, delT, ...
        0 ,0);
    %load the calibrated data from forward solution
    [¬,freq_index,¬]=intersect(round(fw.freqs/1e9,1), ...
        round(fctrs/1e9,1));
    measMag=squeeze(Calibrated_Mag(:,:,freq_index));
    measPha=squeeze(Calibrated_Pha(:,:,freq_index));
    disp(['The index of freq is ' num2str(freq_index(:)')]);
    %%%%%%%%%%%%%%%%%%%%%%%%%%
    %%%%% DBIM iterations %%%%%
    %%%%%%%%%%%%%%%%%%%%%%%%%%
    for iter_inner = 1:maxIter(ind_freq)
        disp(['iteration #' num2str(iter_inner) ' > forward ...
            solver ...(FDTD is running)' ])
        %--------------------project_FDTD_2D----------------------
```

```
76          [greensFunctions_mag, greensFunctions_pha, ...
               receivedFields_mag,...
77              receivedFields_pha, ¬] = ...
                   project_FDTD_2D(FDTD_Prep_path,...
78              estEpsInf, estEpsDelta, estCond, tauP, delT, eps0, ...
                   mu0,...
79              delX, source, numAnts, numFreqs, omegas,timeSteps, ...
                   EpsS,...
80              bbSize, esource_mag, esource_pha);
81          %========inverse solution setup ==========
82          disp(['iteration #' num2str(iter_inner) ' > inverse ...
               solver ...'])
83          [ Mat_A, Data_ant] = Generate_Matrix( ...
               receivedFields_mag, ...
84              receivedFields_pha, greensFunctions_mag, ...
85              greensFunctions_pha, measMag, measPha, numFreqs, ...
                   numTR,...
86              omegas, eps0, PairTR, tauP, bbSize);
87          Result.residual3(iter_total) = norm(Data_ant,2);
88          Result.res_diff_1(iter_total) = ...
               norm(estEpsInf(bbox_interior_mask)...
89              -Debye_coarse_2D_model.EpsInf(bbox_interior_mask))./...
90              norm(Debye_coarse_2D_model.EpsInf(bbox_interior_mask));
91          Result.res_diff_2(iter_total) = ...
               norm(estEpsDelta(bbox_interior_mask)...
92              -Debye_coarse_2D_model.DeltaEps(bbox_interior_mask))./...
93              norm(Debye_coarse_2D_model.DeltaEps(bbox_interior_mask));
94          Result.res_diff_3(iter_total) = ...
               norm(estCond(bbox_interior_mask)...
95              -Debye_coarse_2D_model.SigmaS(bbox_interior_mask))./...
96              norm(Debye_coarse_2D_model.SigmaS(bbox_interior_mask));
97          %=======Start the solve the linear equation=====
98          Solve_Linear_Equation
```

```
99          if numFreqs~=1
100             contrast(2*end/3+1:end)=multiple_sigma * ...
                    contrast(2*end/3+1:end);
101         end
102         Result.allContrast(:,iter_total) = contrast;
103         contrast(2*end/3+1:end) = ...
                contrast(2*end/3+1:end).*2*pi*1e9*eps0;
104         if isnan(contrast)
105             error('The value of contrast includes NaN !');
106         end
107         disp(['Residual error = ' ...
                num2str(Result.residual3(iter_inner,1))])
108         estEpsInf(bbox_interior_mask) = ...
                estEpsInf(bbox_interior_mask) + ...
109             contrast(1:end/3);
110         estEpsDelta(bbox_interior_mask) = ...
                estEpsDelta(bbox_interior_mask) + ...
111             contrast(end/3+1:2*end/3);
112         estCond(bbox_interior_mask) = ...
                estCond(bbox_interior_mask) + ...
113             contrast(2*end/3+1:end);
114         estEpsInf(estEpsInf<  constraints.EpsInf & range_c) =  ...
                constraints.EpsInf;
115         estEpsDelta(estEpsDelta<  constraints.DeltaEps & ...
                range_c) =  constraints.DeltaEps;
116         estCond(estCond< constraints.SigmaS & range_c) = ...
                constraints.SigmaS;
117         estEpsInf(estEpsInf>90&range_c) = 90; % for water
118         estCond(estCond>1.6&range_c) = 1.6; % for water
119         if plot_flag
120             Plot_All_Result;
121         end
122         Result.L_curve_x(iter_total,1) = norm(contrast);
```

```
123         Result.L_curve_Ax_b(iter_total,1) = norm(Mat_A * ...
                contrast - Data_ant);
124         %   objective=rho; % this line is for CGLS
125         pre_objective = log10(max(objective));
126         Result.objective_all{iter_total} = objective;
127         %     tau_all(iter_total)=tau_max;
128         pre_contrast = contrast;
129         iter_total = iter_total+1;
130     end
131     Result.hopping_result{ind_freq,1} = estEpsInf;
132     Result.hopping_result{ind_freq,2} = estEpsDelta;
133     Result.hopping_result{ind_freq,3} = estCond;
134 end % DBIM iterations
135 delete(FDTD_Prep_path);
136 end % end function
```

```
1  %  ================== Run IMAT_CS for the inversion ...
       ====================
2  Anorm=norm(Mat_A,2);
3  Mat_A=Mat_A/Anorm;
4  Data_ant=Data_ant/Anorm;%*mul;
5  %------------- test the adjustment factor
6  if numFreqs~=1
7      Mat_A(:,2*end/3+1:end)=Mat_A(:,2*end/3+1:end)*multiple_sigma;
8  end
9  %--------------------------------------
10 switch InP.linear_method
11     case 1
12         %---------------------TwIST-----------------------
13         tau_max=max(Mat_A'*Data_ant);
14         %tau_TwIST=0.1*max(Mat_A'*Data_ant);
15         %[Tol]=Adaptive_Para(ind_freq);
```

```
16          if (ind_freq==1 && iter_inner==1)
17              tau_TwIST=0;
18              Tol=10^(-1);
19          else
20              [Tol]=Adaptive_Tol_2(pre_objective);
21              %[tau_TwIST]=Adaptive_tau(pre_contrast,0.5);
22          end
23  %         Tol=10^(-2);
24          lam1=10^(-4);
25          disp(['iteration #' num2str(iter_inner) ' >  TwIST...'])
26          [contrast, x_debias, objective, times, debias_start, ...
               mses, max_svd]...
27              =TwIST(Data_ant, Mat_A, tau_TwIST, 'TOLERANCEA', Tol,...
28              'lambda', lam1, 'MAXITERA',5000,'VERBOSE',0);
29          if InP.Opt_L1
30              L1_result(iter_total) = Optimization_L1(Mat_A, ...
31                  Data_ant, Tol, lam1, contrast, ...
32                  estEpsInf(bbox_interior_mask), ...
33                  Debye_coarse_2D_model.EpsInf(bbox_interior_mask), ...
                        1);
34              contrast=L1_result(iter_total).solu;
35              objective=L1_result(iter_total).objective;
36          end
37      case 2
38          %--------cgls algorithm----------
39          disp(['iteration #' num2str(iter_inner) ' >  CGLS...'])
40          [X,rho,eta] = cgls(Mat_A,Data_ant,50);
41          [k_corner,info] = corner(rho,eta);
42          contrast=X(:,k_corner);
43          objective=k_corner;
44      case 3
45          %---------LSQR algorithm----------
46          disp(['iteration #' num2str(iter_inner) ' >  LSQR...'])
```

```
47          [contrast,FLAG,RELRES] = lsqr(Mat_A,Data_ant);
48          objective = RELRES;
49  end
```

```
1   function [Tol]=Adaptive_Tol_2(pre_objective)
2       if pre_objective>2
3           Tol=10^(-1);
4       else if pre_objective>1.5
5                Tol=10^(-2);
6           else
7               Tol=10^(-3);
8           end
9       end
10      disp( [ 'Tol=' num2str(Tol) ]);
11      disp('adaptive tol is modified');
12  end
```

```
1   function [ Mat_A,Data_ant] = Generate_Matrix( ...
        receivedFields_mag, ...
2       receivedFields_pha, greensFunctions_mag, ...
            greensFunctions_pha, ...
3       measMag,measPha,numFreqs,numTR,omegas,eps0, PairTR, tauP, ...
            bbSize)
4   for nf = 1:numFreqs
5       Mat_A = zeros(numTR*numFreqs*2,bbSize*3);
6       Data_ant = zeros(numTR*numFreqs*2,1);
7       calcMag = squeeze(receivedFields_mag(:,:,nf));
8       calcPha = squeeze(receivedFields_pha(:,:,nf));
9       internalFields = squeeze(greensFunctions_mag(:,:,nf).* ...
10          exp(1i.*greensFunctions_pha(:,:,nf)));
11      multiplier = 1i.*omegas(nf).*eps0;
```

```
12
13      mmMag = zeros(numTR,1);
14      mmPha = zeros(numTR,1);
15      ccMag = zeros(numTR,1);
16      ccPha = zeros(numTR,1);
17      A = multiplier*internalFields(PairTR(:,1),:).* ...
18          internalFields(PairTR(:,2),:);
19      count = 1;
20      for i = 1:numTR
21          mmMag(count) = measMag(PairTR(i,1),PairTR(i,2),nf);
22          mmPha(count) = measPha(PairTR(i,1),PairTR(i,2),nf);
23          ccMag(count) = calcMag(PairTR(i,1),PairTR(i,2));
24          ccPha(count) = calcPha(PairTR(i,1),PairTR(i,2));
25          count = count + 1;
26      end
27      data = ccMag.*exp(1i.*ccPha) - mmMag.*exp(1i.*mmPha);
28      numer1 = omegas(nf).*tauP;
29      denom1 = 2*pi*1e9./omegas(nf);
30      denom2 = 1+numer1.^2;
31      Mat_A(1+(nf-1)*numTR*2:(nf-1)*numTR*2+numTR,1:end/3)= real(A);
32      Mat_A(1+(nf-1)*numTR*2:(nf-1)*numTR*2+numTR,end/3+1:2*end/3) ...
33          = real(A).*(1./denom2)+imag(A).*(numer1./denom2);
34      Mat_A(1+(nf-1)*numTR*2:(nf-1)*numTR*2+numTR,2*end/3+1:end) ...
35          = imag(A).*denom1;
36      Mat_A(1+(nf-1)*numTR*2+numTR:nf*numTR*2,1:end/3)= imag(A);
37      Mat_A(1+(nf-1)*numTR*2+numTR:nf*numTR*2,end/3+1:2*end/3) ...
38          = imag(A).*(1./denom2)+real(A).*(-numer1./denom2);
39      Mat_A(1+(nf-1)*numTR*2+numTR:nf*numTR*2,2*end/3+1:end) ...
40          = -real(A).*denom1;
41      Data_ant(1+(nf-1)*numTR*2:nf*numTR*2) = [real(data);imag(data)];
42  end % loop over freqs
43
44  end
```

A.3 Matlab Code of Optimized Initial Guess Method

```
function opt_init = Analyze_optimized_init(init_result,init_guess)
for i=1:length(init_result)
    temp_guess(i)=init_result(i).residual3(end);
end
opt_init=find(temp_guess==min(temp_guess));
if length(opt_init)~=1
    warning('Existing more than one optimized initial guess!')
end
disp('the optimized initial guess is:');
disp(['EpsInf = ' num2str(init_guess.EpsInf(opt_init))]);
disp(['DeltaEps = ' num2str(init_guess.EpsDelta(opt_init))]);
disp(['EpsInf = ' num2str(init_guess.EpsInf(opt_init))]);
end
```

```
function value_guess=Create_initial_guess(guess_number)
initial_bottom=[4.68 3.21 0.0881]';
initial_top=[17.3 19.4 0.535]';
k=guess_number-1;
value_guess=(initial_top-initial_bottom)/k*(0:k) + ...
    repmat(initial_bottom,1,guess_number);
end
```

A.4 Matlab Code of L_1 Optimization method

```
function L1_result=Optimization_L1(A,b,Tol,lam1,est_contrast,...
    pre_solution,Original_Debye_model_EpsInf,visible)
```

```
npoints = 200;  % Number of points on the L-curve for Tikh and dsvd.
smin_ratio = 16*eps;  % Smallest regularization parameter.
eta1 = zeros(npoints,1);
rho1 = eta1;
reg_param = eta1;
RE1=eta1;
Pt1=eta1;
reg_param2 = eta1;
G=eta1;
m=length(est_contrast);
sort_contrast=sort(abs(est_contrast));
for i=1:npoints
    point=ceil((i-1)/npoints*m);
    reg_param2(i)=sort_contrast(point+1);
end
reg_param2=flipud(reg_param2);
reg_param=reg_param2;
for i=1:npoints
    [contrast,x_debias,objective,times,debias_start,mses,max_svd]=...
        TwIST(b,A,reg_param(i),'TOLERANCEA',Tol,'lambda',lam1,...
        'MAXITERA',5000);
     eta1(i)=norm(contrast,1);
     rho1(i)=norm(A*contrast-b);
     RE1(i)=norm((contrast(1:end/3)+pre_solution)-...
     Original_Debye_model_EpsInf)./norm(Original_Debye_model_EpsInf);
     solution{i}=contrast;
end
locate=find(RE1==min(RE1));
if visible
    figure(111); hold off;
    plot(eta1,rho1,'-*'); hold on;
    for i=20:20:200
        text(eta1(i),rho1(i),num2str(reg_param(i)));
```

```
36      end
37      figure(112); hold off;
38      plot(reg_param,RE1,'-*'); hold on;
39      xlabel('para'); ylabel('Relatvie error');
40      figure(113); hold off;
41      loglog(eta1,rho1,'-*'); hold on;
42      xlabel('log(||x||_1)'); ylabel('log(||Ax-b||)');
43      plot(eta1(locate),rho1(locate),'ro'); hold on;
44      refresh,pause(0.1)
45  %       plot_lc(rho1,eta1,'-x',1,reg_param);
46  end
47  L1_result.para=reg_param;
48  L1_result.curve={eta1,rho1,RE1};
49  L1_result.solu=solution{locate};
50  L1_result.objective=0.5*(rho1(locate))^2 + reg_param(locate) * ...
        eta1(locate);
51  L1_result.RE_locate=locate;
52  end
```

A.5 Matlab Code of 2-D Forward FDTD Simulation

```
1  % db_Main_Script
2  clear
3  fw.new_res=input('Please enter a new coarse resolution on a ...
       mulitple of 0.5(mm):');
4  fw.model_phantom=input('Please choose a kind of breast phantom ...
       (1¬999):');
5  fw.mode=input('Please input the mode of forward FDTD: \n ...
       1.Known_original \n 2.Unknown_original \n');
6  load(['..\data\model' num2str(fw.model_phantom) ...
       '\all_material.mat'],'frequency');
```

```
fw.freqs=frequency;
switch fw.mode
    case 1
        fw.fctr=2e9; % 2.0 GHZ
        fw.mode='Forward_original';
        disp(['The central frequency is ' num2str(fw.fctr/1e9) ' ...
            GHz']);
        fw.save_path_whole{1} = db_MF_Forward_FDTD(fw.fctr,fw);
        disp('Starting to deal with the simulated data...');
        Deal_with_original_simulation(fw); % Only called for ...
            when we know the original model
    case 2
        % wide band model
        fw.fctr=2e9; % 2.0 GHZ
        fw.mode='Forward_background';
        disp(['The central frequency is ' num2str(fw.fctr/1e9) ' ...
            GHz']);
        fw.save_path_whole{1} = db_MF_Forward_FDTD(fw.fctr,fw);
        disp('Starting to deal with the simulated data...');
        Deal_with_original_simulation(fw);
    otherwise
        error('Please check the input of the forward mode');
end

save(['..\data\model' num2str(fw.model_phantom) ...
    '\forward_para.mat'],'fw');
disp('forward parameters have been saved!');
```

```
% db_MF_Forward_FDTD
function [save_path_whole] = db_MF_Forward_FDTD(fctr,fw)
tic
%%%%% CHOOSE OPTIONS %%%%%%%
```

```
load sim_params_2D
%---------------Forward solution parameter-------------
warning('This is forward solution process !!');
[antLocations_coarse_2D, resolution, mul, coarse_grid_x, ...
    coarse_grid_y,...
     Debye_coarse_2D_model, numAnts] = Transform_Resolution(fw);
warning(['The number of antenna is ' num2str(numAnts)]);
timeSteps=6000;
omegas = 2.*pi.*fctr;
obs_iter = 5;  % used to plot inverse solution
numTR = numAnts*(numAnts-1)/2;
PairTR = Generate_Ant_index(numAnts);
% computational domain dimensions
dimX = coarse_grid_x;%from temp_coarse_2D.mat
dimY = coarse_grid_y;%from temp_coarse_2D.mat
delX = resolution;%from temp_coarse_2D.mat
delT = delX/(2*c);
%================loading model =========
[estEpsInf, estEpsDelta, estCond, tauP, EpsS, bbSize, ¬,...
    bbox_interior_mask, ¬] = Load_FDTD_material_2D(...
    Debye_coarse_2D_model, fw.model_phantom,1, fw.mode, 0);
%============pre-process the FDTD parameters==============
FDTD_Prep_path = FDTD_Preprocess(num2str(fw.model_phantom), ...
    delT, pml_coarse, dimX, dimY, bbox_interior_mask, mu0, eps0,...
    delX, EpsS, antLocations_coarse_2D);
%%%%%%%%%%%%%%%%%DBIM beginning%%%%%%%%%%%%%%%%%%
disp('Start to reconstruct the MWI...')
numFreqs=1;
switch fw.mode
    case 'Forward_original'
        [source, timeSteps]=create_GMS(fctr,delT,'wide',...
            timeSteps,dimX,dimY,0);
    case 'Forward_background'
```

```
37          [source, timeSteps]=create_GMS(fctr,delT,'wide',...
38              timeSteps,dimX,dimY,0);
39  end
40  [esource_mag,esource_pha]=fft_trans(source,omegas,delT,0,0);
41  disp(['The current frequency is ' num2str(fctr/1e9) 'GHz'])
42  disp( ' > forward solver ...(FDTD is running)')
43  [¬,¬,¬,¬,original_measurement] = project_FDTD_2D(FDTD_Prep_path, ...
44      estEpsInf, estEpsDelta,estCond, tauP, delT, eps0, mu0, delX,...
45      source, numAnts, numFreqs, omegas, timeSteps, EpsS, bbSize,...
46  esource_mag, esource_pha);
47  %--------------return for the foward process---------------
48  disp('The measured data has been saved.');
49  save_path=['..\data\model' num2str(fw.model_phantom) '\model'...
50      num2str(fw.model_phantom) fw.mode];
51  mkdir(save_path);
52  save_path_whole=[save_path '\simulated_model' ...
53      num2str(fw.model_phantom) '_' num2str(fctr/1e9) 'GHz.mat'];
54  save(save_path_whole,'original_measurement', ...
      'delT','delX','source');
55  delete(FDTD_Prep_path);
56  toc
57  end
```

```
1  function ...
       [mag_background,pha_background]=Deal_FDTD_forward(fctr,path_t)
2  load(path_t);
3  [numAnts,¬,len] = size(original_measurement);
4  omega = 2*pi*fctr;
5
6  [esource_mag,esource_pha] = fft_trans(source,omega,delT,0,0);
7  [mag,pha] = ...
       fft_trans(reshape(original_measurement,numAnts^2,len),...
```

```
    omega,delT,esource_mag,esource_pha);
mag_background = reshape(mag,numAnts,numAnts);
pha_background = reshape(pha,numAnts,numAnts);
end
```

```
% deal with the original_measurement as background
function Deal_with_background_simulation(fw)
num_file=length(fw.save_path_whole);
for i=1:num_file
    [mag_background,pha_background]=...
        Deal_FDTD_forward(fw.freqs(i)*1e9,fw.save_path_whole{i});
    mag_background_set(:,:,i)=20*log10(mag_background); %dB
    pha_background_set(:,:,i)=pha_background;
end
save(['..\data\model' num2str(fw.model_phantom) ...
    '\background.mat'],...
    'mag_background_set','pha_background_set');
disp('The new simulated data have been saved!')
end
```

```
function Deal_with_original_simulation(fw)
switch fw.mode
  case 'Forward_original'
    for i = 1:length(fw.freqs)
      [mag_background, pha_background] = ...
          Deal_FDTD_forward(fw.freqs(i), fw.save_path_whole{1});
      Calibrated_Mag(:, :, i) = 20*log10(mag_background); %dB
      Calibrated_Pha(:, :, i) = pha_background; %rad
    end
    save(['..\data\model' num2str(fw.model_phantom)...
```

```
11          '\Calibrated_data.mat'], 'Calibrated_Mag', ...
                'Calibrated_Pha');
12      disp('The new Calibrated data based on original model are ...
            saved!')
13    case 'Forward_background'
14      for i = 1:length(fw.freqs)
15        [mag_background, pha_background] = ...
16            Deal_FDTD_forward(fw.freqs(i), fw.save_path_whole{1});
17        mag_background_set(:, :, i) = 20*log10(mag_background); %dB
18        pha_background_set(:, :, i) = pha_background; % rad
19      end
20      save(['..\data\model' num2str(fw.model_phantom) ...
21          '\background.mat'], 'mag_background_set', ...
                'pha_background_set');
22      disp('The new background data have been saved!')
23  end
24  end
```